1D Raman/Rayleigh-scattering and CO-LIF measurements in laminar and turbulent jet flames of dimethyl ether using a hybrid data reduction strategy

Vom Fachbereich Maschinenbau
an der Technischen Universität Darmstadt
zur
Erlangung des Grades eines Doktor-Ingenieurs (Dr.-Ing.)
genehmigte

Dissertation

vorgelegt von

Dipl.-Ing. Frederik Fuest

aus Bielefeld

Berichterstatter:	Prof. Dr. rer. nat. A. Dreizler
Mitberichterstatter:	Prof. Dr. rer. nat. V. Sick
Tag der Einreichung:	26. April 2011
Tag der mündlichen Prüfung:	14. Juni 2011

Darmstadt 2011

D 17

Preface

The present work is the result of my time as a doctoral candidate at the Department Reactive Flows and Diagnostics at the Technische Universität Darmstadt. First, I would like to thank the head of the Department, Prof. Andreas Dreizler, for his support in doing such a special kind of work at an Department in Mechanical Engineering. In addition, he gave me the opportunity to realize a research stay at Sandia National Laboratories in California and gave me the freedom necessary to dig deeply into the measured data. I also wish to thank Prof. Volker Sick from the University of Michigan for taking over the co-review of this thesis.

Exceptionally, I whish to thank Dr. Robert S. Barlow for his contributions to this work. Without the measurements taken in his remarkable laboratory at Sandia and the friendly collaboration the outcome would have never been possible. I also thank him for the good time, inspiration and fun I had at Sandia. I also whish to thank Prof. J.-Y. Chen (University of California, Berkeley) for providing me with laminar flame calculations, and for sharing his experience in discussions reliably and fast.

Thanks to Dr. Florian Seffrin for sharing the suffering going ahead with Raman measurements in turbulent flames. I whish to thank Dr. Thilo Kissel for the friendship and many evenings of fun at the Frischzelle. Prof. Dirk Geyer I thank for the many years of collaboration and his contributions to the data evaluation I could start with at the beginning of my work. Thanks for interesting discussions and distractions to Dr. Desislava Dimitrova, Raman fellow Thabo Stahler, Matthias Euler, Christof Heeger, Guido Künne and all colleagues from the departments EKT and RSM. I whish to thank Prof. J. A. van Oijen (TU Eindhoven) for his helpful advices regarding the reaction kinetics calculations with CHEM1D, Prof. Rolf Schäfer (TU Darmstadt) for advices in questions about molecule calculations, Dr. Guanghua Wang for the clean code I could start with to implement the extensions derived in this work, and Prof. Bengt Friman (TU Darmstadt, GSI) for the most inspiring lectures I ever attended. Special thanks go to my friends and Mensa-mates Frank Vytrisal, Robert Dicks, Bernd Emanuel, Philipp Benz, and Uli Giesecke. I thank Roland Berntheisel and his workshop for the help in construction and manufacturing of parts for the experimental Raman setup at Darmstadt.

Last, I wish to express my gratitude to my parents, my brother, and Verena for supporting me the long time period of my education and their help I received whenever they could.

Darmstadt, June 2011 Frederik Fuest

Contents

Glossary

Uppercase Latin letters		Unit
A_{probe}	cross sectional area of probe volume	m^2
C_{HC}	sum of concentrations from all hydrocarbon species	mol/Liter
C_i	molar concentrations	mol/Liter
E_i	eigenenergy of molecule	J
E_σ	components of electric field vector	Vm^{-1}
F	mixture fraction	–
F_{all}	reference mixture fraction including all species	–
F_{st}	stoichiometric mixture fraction	
F^*	adapted mixture fraction	–
J	rotational quantum number	–
K	second rotational quantum number	–
N	number density	m^{-3}
N_{A}	Avogadro-constant	mol^{-1}
N_{detector}	total noise of Raman detector	–
N_{L}	Loschmidt-constant	m^{-3}
N_{tot}	total statistical noise in Raman measurement	–
N_i	number density of species i	m^{-3}
P_{pixel}	spectral Raman pixels	–
Q	partition function	–
R	internuclear distance	a_0
R_e	equilibrium internuclear distance	a_0
Re	Reynolds number	–
S	radiated photons per time	s^{-1}
$S_{\mathrm{CO-LIF}}$	measured CO-LIF signal	–
S_{Ray}	measured Rayleigh signal	–
$S_{\mathrm{Ram},i}$	measured Raman signal of species i	–
T	local temperature	K
T_0	standard temperature (273.15 K)	K
T_{Ram}	measured Raman temperature	K
T_{Ray}	measured Rayleigh temperature	K
$V(R)$	potential energy curve of molecule	–

V_m	molar volume at T_0 and p_0, (22.413996(39) Liter/mol)	Liter/mol
V_probe	probe volume	m^3
X_i	mole fractions	–
Y_C	elemental mass fraction of carbon	–
Y_H	elemental mass fraction of hydrogen	–
Y_C^*	adapted elemental mass fraction of carbon	–
Y_H^*	adapted elemental mass fraction of hydrogen	–
Y_i^*	adapted mass fractions	–
Y_i	mass fractions	–
SNR	signal to noise ratio	

Lowercase Latin letters		**Unit**
$\boldsymbol{p}$	classical dipole moment vector	Cm
a	strain rate	s^{-1}
$b^{(2)}_{J^f K^f : J^i K^i}$	Placzek-Teller factors for symmetric top molecules	–
$c_\mathrm{Ray,calib}$	Rayleigh calibration constant	Km^{-2}
c_0	speed of light in vacuum	m/s
$c_{\mathrm{Ram},i\leftarrow j}$	Raman crosstalk calibration constant	
$c_{\mathrm{Ram},i}$	Raman response calibration constant	
c_{ii}	Raman response curve	–
c_{ij}	Raman crosstalk curve	–
f_i	fractional energy population factor	–
g_N	nuclear statistical weight	–
h	Planck constant	Js
$i \leftarrow j$	Raman crosstalk from molecule j onto Raman channel of molecule i	–
l_probe	length of probe volume	m
n	index of refraction	–
n_{e^-}	number of detected photoelectrons	–
p	local pressure	kPa
p_0	standard pressure (101.325 kPa)	kPa
r	radial coordinate in experiment	mm
v	vibrational quantum number	–
w_i	molar mass	g/mol
x	radial coordinate in calculation	mm
z	molecular diffusion parameter	–
z^*	adapted molecular diffusion parameter	–

Uppercase Greek letters		**Unit**
$\Delta\alpha$	anisotropic polarizability	$\mathrm{Cm}^2\mathrm{V}^{-1}$
Γ_app	apparatus function	–
Ω	solid angle	steradian
Φ	time-averaged radiated power	W
Φ_nuclei	nuclear wave function of molecule	–

Ψ	wave function of molecule	–

Lowercase Greek letters

		Unit
5σ	detection limit at five standard deviations	–
$\alpha_{\rho\sigma}$	cartesian components of polarizability tensor	$\mathrm{Cm^2V^{-1}}$
μ	reduced mass of molecule	amu
$\overline{\alpha}$	mean polarizability	$\mathrm{Cm^2V^{-1}}$
ϕ	equivalence ratio	–
ϕ_{rot}	rotational wave function of molecule	–
ϕ_{vib}	vibrational wave function of molecule	–
$\psi_{\mathrm{electronic}}$	electronic wave function of molecule	–
ρ	depolarization ratio	–
σ	Raman/Rayleigh cross section	$\mathrm{m^2}$
τ_{pulse}	laser single-shot pulse length	s
$\tilde{\nu}_{\mathrm{Laser}}$	wavenumber of laser	$\mathrm{m^{-1}}$
ε_0	vacuum permittivity	$\mathrm{AsV^{-1}m^{-1}}$

Superscripts

$\parallel$	parallel polarized to scatter plane	–
$\perp$	perpendicular polarized to scatter plane	–

Operators and Symbols

$\boldsymbol{\mathfrak{p}}$	quantum mechanical dipole moment vector	Cm
$\circ$	entrywise matrix product	
$\hbar$	reduced Planck constant, $h/(2\pi)$	Js
$\langle\alpha^2_{\rho\sigma}\rangle$	isotropic average of $\alpha^2_{\rho\sigma}$	$\mathrm{C^2m^4V^{-2}}$
$\mathcal{S}_{\Sigma fi}$	superposed, convolved, calculated Raman transitions	–
$\mathcal{S}_{fi}$	convolved single transition	–
$\mathfrak{E}_{\mathrm{Laser}}$	laser single-shot energy	J
$\mathfrak{N}_{\mathrm{photons}}$	Raman/Rayleigh scattered photons	–

Abbreviations

DME	dimethyl ether (C_2H_6O)
FWHM	full width at half maximum
HC	hydrocarbon species
L1	first laminar DME/air jet configuration (11.4 % DME)
L2	second laminar DME/air jet configuration (28.1 % DME)
LIF	laser induced fluorescence
MI	matrix inversion method
nonHC	non-hydrocarbon species
SF	spectral fitting method
T1	first turbulent DME/air jet configuration (11.4 % DME)
T2	second turbulent DME/air jet configuration (19.7 % DME)

1 Introduction

1.1 Motivation

Turbulent combustion processes are of high practical relevance. In 2008, more than 90 % of the global primary energy supply was based on fossil and renewable fuels [2]. Hence, stability of combustion processes and their impact on air quality and climate change are important aspects in the development of new technical combustion devices. This demands for a detailed understanding of the complex interactions between the turbulent flow field and the chemistry of the combustion process.

Significant progress has been made in collaborative research within the International Workshop on Measurement and Computation of Nonpremixed Flames (TNF) [94], adressing particular phenomena in well-documented and simplest possible laboratory-scale flames to provide bench mark configurations for numerical simulations of these flames. In recent years, the data base of bench mark flames was consequently extended with increasing complexity of both, the flow field and the chemistry. The collaborative efforts began by looking with laser-based diagnostics into simple jet flames of diluted hydrogen [79, 93] and were subsequently extended to hydrogen/methane/nitrogen jet flames [84].

As the next step in complexity, a pilot or bluff-body was added to the burner geometry to stabilize the flow and allow for high flow and mixing rates with increased turbulence. In addition, complexity of the chemistry was increased by using methane instead of the chemically much simpler hydrogen and piloted partially-premixed methane/air flames were studied in [9–11, 13, 55, 84]. The progression in complexity is summarized in [15] and some of the steps are exemplified in Fig. 1.1. With respect to the fluid dynamics, further increased complexity was achieved by swirling flows [46, 68] or more recently by stratification [14, 86].

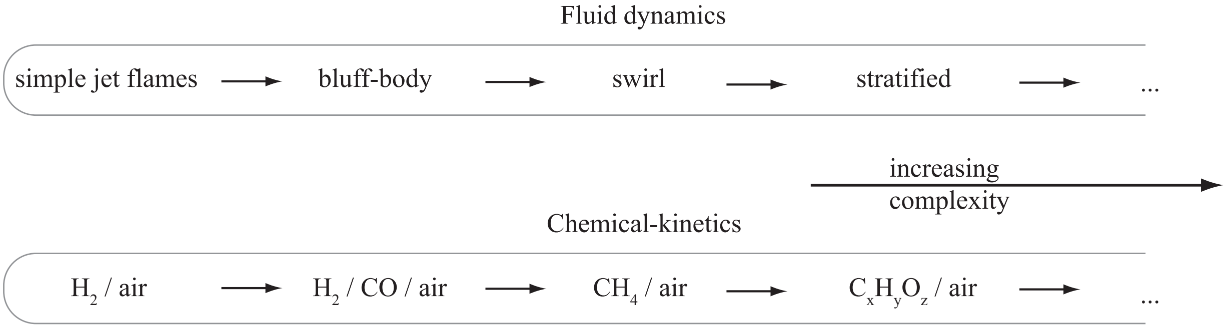

Figure 1.1: Simplified progression in complexity of the flow field and chemistry of target flames for the investigation of turbulence-chemistry interactions. For a detailed view see [15].

In addition to velocity measurements of the flow field, instantaneous measurements of the thermochemical state were performed. This requires the simultaneous measurement of the temperature and all major species concentrations. For this purpose, laser-based point-wise and more recently line-imaged instantaneous Raman/Rayleigh scattering was developed continuously over the last decades and forms an important basis for understanding turbulence-chemistry interactions in turbulent flames.

The demand on lasers, optical and detection systems is challenging due to the weakness of the Raman effect and the processing of the data into concentrations can be even impossible in flames with high fluorescence and broadband interference levels. In general, such distortions of the Raman signals are especially large with increasing complexity of the fuel. In this work the feasibility of measurements and data-processing strategies in flames of such complex fuels as dimethyl ether (DME) was investigated in a collaborative work with R. Barlow from Sandia National Laboratories, Livermore and J.-Y. Chen from University of California, Berkeley.

In an earlier step, the strength of two existing data-reduction strategies were investigated and combined in a hybrid method that allows for faster and more precise data processing.

1.2 State of the Scientific Knowledge

Raman/Rayleigh/CO-LIF data processing Two different approaches to Raman data processing are described in the turbulent combustion literature. The matrix inversion method (MI) [8, 17, 34, 77] and the spectral fitting method (SF) [43]. Both are described more detailed in Sections 2.7.1 and 2.7.2.

The matrix inversion method allows for lower camera readout noise due to on-chip binning, and processing is more than two orders of magnitude faster. However, extensive calibration is needed, and uncertainties in calibrations of reactive species and crosstalk terms at flame temperatures can be large. Furthermore, it is not practical to account for the effects of beam steering in turbulent flames, which shifts the entire Raman spectrum relative to the fixed on-chip binning regions. On the other hand, the spectral fitting method is based on quantum mechanical theory. This reduces the number of calibrations to only one per species and reduces uncertainty within temperature ranges that are difficult to calibrate. For luminous flames the background radiation can be corrected more rigorously in the spectral fitting process, and beam steering can be automatically handled. However, the preserved spectral information comes with the price of higher readout noise, slower data acquisition rates, and significant effort fitting the Raman spectrum of each single-shot measurement.

In this work a hybrid approach for processing Raman data was developed, combining the advantages of both methods.

Raman/Rayleigh measurements in flames of DME Previous studies using Raman scattering in gaseous hydrocarbon/air flames with fuels chemically more complex than methane are rare. No Raman/Rayleigh measurements in flames of dimethyl ether exist at all. In an early study by Stårner et al. [89] simultaneous Raman/Rayleigh/LIF measurements were made in piloted turbulent jet diffusion flames of diluted propane. It was shown that Raman measurements were feasible only when propane was diluted substantially by air or nitrogen, preventing overwhelming soot precursor interferences. Pilot-stabilized non-premixed methanol flames were investigated in by Masri et al. [67] for stable conditions as well as close to blowoff. Propane flames, partly in mixture with dodecane or Diesel, were investigated by Dreyer et al. [35]. The speciality of this work was a Raman measurement in the vicinity of liquid fuel droplets. One important conclusion was that for their experimental conditions 355 nm excitation proved to be a better candidate wavelength than previously thought. Meier and Keck [69] and Rabenstein et al. [80] investigated premixed sooting and non-sooting C_2H_4/air and CH_4/air flames, respectively. In Meier and Keck's comparative study the signal-to-background ratio of Raman measurements was investigated for pulsed laser radiation at 532, 489, 355, and 266 nm. Excitation wavelength of 532 nm proved to be most suitable, and limitations of concentration measurements by laser Raman measurements were demonstrated. In contrast, for soot-volume concentrations nearly two orders of magnitude higher, Egermann et al. [37] reported excitation wavelengths of 266 nm to be beneficial compared to 355 nm in ethylene diffusion flames because of reduced spectral overlap between Raman bands and LIF interferences. Nooren et al. [77] reported on Raman/Rayleigh/LIF measurements in Dutch natural gas jet diffusion flames. High levels of fluorescence interferences were subtracted from the Raman signals by empirical correlations using, amongst others, an interference channel monitored at 615 nm. This approach was exploited by Dibble et al. [33] and it is followed similarly in the present study. Brockhinke et al. [24] studied LIF of C_2 following a UV-excitation at 248 nm. They identified fluorescence in different spectral ranges and discussed possible interferences with Raman bands especially around 350 nm. Removal of LIF interferences by separating and subtracting the signals in two polarization directions was proposed as a possible approach to measuring mole fractions by Raman scattering in fuel rich laminar premixed propylene/oxygen flames. Egermann et al. [37] similarly proposed the possibility of Raman measurements with excitation at 266 nm in sooting ethylene diffusion flames using horizontal and vertical polarization directions. None of these studies, however, addressed in sufficient detail the role of intermediate hydrocarbons or strategies to account for the resulting effects on Raman/Rayleigh scattering.

1.3 Structure of the thesis

The present thesis is structured as follows:

- Chapter 2 provides the measurement principles and introduces the measured and derived quantities. The mathematical description for the process of Raman/Rayleigh scattering and laser induced fluorescence of CO is outlined followed by the application of the theory in processing of actual measurement data. After describing the experimental setup, the data reduction strategies and measurement uncertainties are detailed.
- Chapter 3 presents a hybrid approach for processing of Raman data, that combines the strength of both previous methods. The spectral library based on quantum mechanical calculations of the spectral fitting method is used to provide essential information for the data evaluation of the Raman data in the matrix inversion method. Calculated Raman spectra are compared to experimental spectra. The new method is compared with both previous methods in laminar flat flames and a laminar hydrogen jet flame.
- Chapter 4 proceeds with necessary extensions of the previously developed hybrid method to allow for data evaluation of Raman/Rayleigh/CO-LIF measurements in hydrocarbons more complex than methane. This is quantitatively exemplified on measurements of laminar and turbulent jet flames of dimethyl ether presenting new methods for reasonable comparison with numerical simulations in such laminar and turbulent flames. Some additional information on the data-processing are provided in Appendices A and B.
- The last chapters provide the conclusions from the preceding chapters and presents relevant topics for future investigations.

2 Principles

2.1 Introduction

Multiscalar measurements in turbulent flames are an important key to a detailed understanding of turbulence-chemistry interaction. Raman/Rayleigh spectroscopy is a valuable diagnostic tool for this purpose [8, 16, 36, 49]. Spontaneous Raman scattering does not require tunable excitation radiation, and the spectrum of Raman scattered light contains characteristic signatures of different molecules in the probe volume. The scattering process is not disturbed by inter-molecular collisions, so signal evaluation is independent of bath conditions. These advantages are offset by small scattering cross-sections, such that single-shot Raman scattering in turbulent hydrocarbon flames allows only the detection of main species (e.g., CO_2, O_2, CO, N_2, H_2O, CH_4, H_2), based on rovibrational Raman transitions of the Stokes side. Spontaneous Raman scattering, applied by itself or in combination with Rayleigh scattering of the same laser source, has been used to study a broad range of turbulent flames [8, 15]. Much of this work has been motivated by the need for detailed data to validate combustion models. In recent years, this has included measurements of scalar gradients and scalar dissipation in atmospheric pressure CH_4/air flames, including nonpremixed, partially premixed, stratified, and premixed cases [15, 45, 100]. Gradient measurements demand higher spatial resolution and precision than is needed to measure statistics of the scalars themselves [99]. This has prompted development of specialized imaging spectrographs using high efficiency transmission gratings and low f-number optics [14]. Commensurate with the improved resolution and detection efficiency of these systems is the need to optimize data acquisition and processing methods to achieve the best possible accuracy and precision. Simultaneous measurements of CO by two-photon laser-induced fluorescence (LIF) is superior to Raman scattering for low CO number densities, yielding higher precision and accuracy, especially in flames with strong fluorescence interference. This chapter specifies the principles of the measurement techniques, the expermental setup, and the data reduction strategies.

2.2 Measurement principles

The basic principles of quantitative species and temperature measurements by Raman/Rayleigh scattering and laser induced fluorescence of CO (CO-LIF) can be expressed in the most simple form using just the crucial proportionalities.

Rayleigh temperature measurement The measured Rayleigh signal S_{Ray} is proportional to the number density, N, in the probe volume. This yields the following relation for the temperature determined by Rayleigh scattering

$$T_{\mathrm{Ray}} \propto 1/S_{\mathrm{Ray}} \, . \tag{2.1}$$

Raman species measurement Quantitative species measurements are used to obtain number densities of particular species i from their measured Raman signals $S_{\mathrm{Ram},i}$

$$N_i \propto S_{\mathrm{Ram},i} \, . \tag{2.2}$$

Here, Raman signals are simultaneously collected from six major species (CO_2, O_2, CO, N_2, H_2O, and H_2), and one cumulated signal from most of the hydrocarbons (HCs) occuring in combustion processes.

Laser induced fluorescence of CO Similarly, the number density of CO is determined from the CO-LIF measurement by

$$N_{\mathrm{CO-LIF}} \propto S_{\mathrm{CO-LIF}} \tag{2.3}$$

with $S_{\mathrm{CO-LIF}}$ being the measured CO-LIF signal.

Derived quantities from species measurements For reasons of convenience, instead of number densities, molar concentrations C_i (in units of mol/Liter), mole fractions X_i, and mass fractions Y_i, are used throughout this work. Molar concentrations are related to number densities or mole fractions by

$$C_i = \frac{N_i}{N_{\mathrm{A}}} = \frac{N_i}{N_{\mathrm{L}} V_{\mathrm{m}}} = \frac{X_i}{V_{\mathrm{m}}} \frac{T_0}{T} \frac{p}{p_0} \tag{2.4}$$

with N_A being the Avogadro-constant[‡], N_L the Loschmidt-constant[§], T_0, p_0, and V_m being the temperature, pressure, and molar volume[¶] of an ideal gas at consistent conditions, respectively. T and p are local temperature and pressure in the probe volume. Mole fractions are obtained from molar concentrations or mass fractions by

$$X_i = C_i V_\mathrm{m} \frac{T}{T_0} \frac{p_0}{p} = \frac{C_i}{\sum_i C_i} = \frac{Y_i/w_i}{\sum_i Y_i/w_i} \tag{2.5}$$

with w_i being the molar mass of species i. Mass fractions expressed in terms of molar concentrations or mole fractions are

$$Y_i = \frac{C_i w_i}{\sum_i C_i w_i} = \frac{X_i w_i}{\sum_i X_i w_i} \,. \tag{2.6}$$

The temperature based on Raman scattering is obtained from

$$T_\mathrm{Ram} = T_0 \frac{p}{p_0} \frac{N_\mathrm{L}}{\sum_i N_i} \,. \tag{2.7}$$

Other quantities, which were derived from the quantities above included mixture fraction, atom ratios, elemental mass fractions, and the differential diffusion parameter. These are defined in the corresponding sections below.

2.3 Physical principles

This section provides the principles for the mathematical description of Raman/Rayleigh scattering and is mostly based on Long [64]. Laser induced fluorescence (LIF) is also briefly considerd. Here, Raman/Rayleigh scattering is only referred to non-resonant Raman/Rayleigh scattering, whereas LIF is a resonant process. In general, all three processes are based on the interaction of electrons and photons and a possible energy transfer between both. However, here photons are treated classically in terms of electromagnetic radiation and their source is well-described by the concept of an oscillating electric dipole from classical electrodynamics. In contrast, for an appropriate description of the energy states and transitions of electrons that are bound to molecules, quantum mechanical descriptions are essential. Finally, photon numbers, their state of polarization and their wavenumber are predicted to provide the necessary information for the interpretation of the experimental data.

[‡] $N_\mathrm{A} = 6.02214179(30) \cdot 10^{23}\,\mathrm{mol}^{-1}$

[§] $N_L = 2.6867774(47) \cdot 10^{25}\,\mathrm{m}^{-3}$

[¶] $V_\mathrm{m} = 22.413996(39)$ Liter/mol at $T_0 = 273.15\,\mathrm{K}, p_0 = 101.325\,\mathrm{kPa}$

Oscillating electric dipole moment For a distribution of charges in space the resulting electric dipole moment vector is defined as

$$\boldsymbol{p} = \sum_i e_i \boldsymbol{r}_i \tag{2.8}$$

with e_i the electric charge of particle i and $\boldsymbol{r}_i$ its position vector. The oscillating electric dipole moment vector is given by

$$\boldsymbol{p} = \boldsymbol{p_0} \cos \omega t \tag{2.9}$$

with the dipole amplitude vector $\boldsymbol{p_0}$ and the oscillation frequency ω. Time-averaging of its square yields

$$\frac{1}{\pi} \int_0^{\pi} \boldsymbol{p}^2 \mathrm{d}t = \frac{1}{2} \boldsymbol{p_0}^2 \,. \tag{2.10}$$

With appropriate orientation in space, i.e. along one coordinate axis, the amplitude vector is fully described by $p_0 \sin \theta$, with the amplitude p_0 and the angle θ defined with respect to the dipole axis. Classically, the source of electromagnetic radiation by such an oscillating electric dipole is commonly expressed in terms of time-averaged power emitted into the element of solid angle $\mathrm{d}\Omega$, see Long [64, p.560]

$$\Phi_\Omega = \frac{\pi^2 c_0 \tilde{\nu}^4 p_0^2}{2\varepsilon_0} \int \sin^2 \theta \, \mathrm{d}\Omega \,, \tag{2.11}$$

where p_0 is the amplitude of the oscillating electric dipole, c_0 the speed of light in vacuum[‡], $\tilde{\nu}$ the wavenumber of the scattered light, ε_0 the vacuum permittivity[§], and θ the angle of observation with respect to the dipole axis. However, in present experiments, which make commonly use of CCD cameras for the detection of the signal, instead of radiated power photon counts are measured. Thus, Eq. (2.11) divided by the energy of one photon[¶], $hc_0\tilde{\nu}$, yields the number of signal photons emitted by the oscillating dipole into the element of solid angle $\mathrm{d}\Omega$ per time

$$S_\Omega = \frac{\pi^2 \tilde{\nu}^3 p_0^2}{2\varepsilon_0 h} \int \sin^2 \theta \, \mathrm{d}\Omega \tag{2.12}$$

with the element of solid angle defined as

$$\mathrm{d}\Omega = \sin \theta \mathrm{d}\theta \mathrm{d}\phi \,. \tag{2.13}$$

The angle ϕ is defined in the plane perpendicular to the dipole axis. In order to calculate the exact photon number for one specific observation geometry it is necessary to integrate over appropriate angles ϕ and θ to account for the angular dependence of the scattered light and the f-number of the first collection lens used in the experiment. Hence, the

---

[‡] $c_0 = 299792458\,\mathrm{m/s}$

[§] $\varepsilon_0 = 8.8541878 \cdot 10^{-12}\,\mathrm{AsV^{-1}m^{-1}}$

[¶] $h = 6.62606896(33) \cdot 10^{-34}\,\mathrm{Js}$ (Planck constant) number of photons emitted onto that lens per time is

$$S_{\Delta\Omega} = \frac{\pi^2 \tilde{\nu}^3 p_0^2}{2\varepsilon_0 h} \int_{\theta-\Delta\theta}^{\theta+\Delta\theta} \int_{\phi-\Delta\phi}^{\phi+\Delta\phi} \sin^3\theta \, \mathrm{d}\theta \mathrm{d}\phi \,. \tag{2.14}$$

Herein, the angles θ and ϕ are defined with respect to the center line of observation, and $\Delta\theta$ and $\Delta\phi$ account for the aperture of the collection lens. For circular lenses these are simply $\Delta\theta = \Delta\phi = \arctan(\,0.5 \,/\, f/\#)$. The angle ϕ is defined from 0 to 2π, and the angle θ is defined from 0 to π. Integration of the angle dependent part in Eq. (2.14) yields the factor $\int_0^{2\pi} \mathrm{d}\phi \int_0^{\pi} \sin^3\theta \, \mathrm{d}\theta = 8\pi/3$ for the total number of emitted photons. In order to use Eq. (2.14) for the description of radiation that originates from particular molecules it is necessary to calculate the electric dipole moment of that molecule.

Electric dipole moments of molecules Gaseous molecules are freely rotating particles in space with unknown orientation. In addition, their complex nature leads to a huge amount of different internal energy states which must be considered all separately for the correct prediction of the numbers and wavenumbers of detectable photons. An appropriate mathematical description of all internal energy states of a molecule is provided by the corresponding time-independent Schrödinger equation where such states k are expressed by the wavefunction $|\Psi_k\rangle$ and the associated energy eigenstate E_k. To solve this equation for particular molecules, generally, the eigenfunction Ψ is separated by using the product ansatz

$$\Psi = \psi_{\text{electronic}} \, \Phi_{\text{nuclei}} \,. \tag{2.15}$$

This yields another two Schrödinger equations for the electronic and the nuclear part of the molecule, respectively. Vibrational and rotational motions of the nuclei are further separated by

$$\Phi_{\text{nuclei}} = \phi_{\text{vib}} \, \phi_{\text{rot}} \,. \tag{2.16}$$

Note that for both ansätze, interaction between the separated parts occur, which are for the molecules of interest in this work mostly small in the former case but important in the latter case with respect to appropriate descriptions of higher quantum-states populated at common flame temperatures. The corresponding description for a dipole moment in the quantum picture is transition-specific involving the initial state $|\Psi_i\rangle$ and the final state $|\Psi_f\rangle$ of the molecule. Mathematically, it is given by the expectation value of the dipole moment operator $\hat{\mathfrak{p}}$

$$\mathfrak{p} = \langle \mathfrak{p}_{fi} \rangle = \int_{\boldsymbol{r}} \Psi_f^* \hat{\mathfrak{p}} \; \Psi_i \mathrm{d}\boldsymbol{r} \tag{2.17}$$

Generally, the electric dipole moment $\mathfrak{p}$ can be separated into a permanent, an induced and an instantaneous part expressed by

$$\mathfrak{p} = \mathfrak{p}^{\text{per}} + \mathfrak{p}^{\text{ind}} + \mathfrak{p}^{\text{inst}} \,. \tag{2.18}$$

The permanent electric dipole $\mathfrak{p}^{\mathrm{per}}$ is the source of absorption or spontaneous emission of light, i.e. both necessary for the description of laser induced fluorescence. The instantaneous part $\mathfrak{p}^{\mathrm{inst}}$ is not considered here. The induced part $\mathfrak{p}^{\mathrm{ind}}$ is responsible for the arise of Raman/Rayleigh scattering and is further separated into one linear and one non-linear part

$$\mathfrak{p}^{\mathrm{ind}} = \mathfrak{p}^{\mathrm{L}} + \mathfrak{p}^{\mathrm{NL}} \tag{2.19}$$

which is in index notation written as

$$\mathfrak{p}^{\mathrm{ind}}_{\rho} = \alpha_{\rho\sigma} E_{\sigma} + \frac{1}{2}\beta_{\rho\sigma\tau} E_{\sigma} E_{\tau} + \frac{1}{6}\gamma_{\rho\sigma\tau\mu} E_{\sigma} E_{\tau} E_{\mu} + \dots \tag{2.20}$$

Here, $\alpha_{\rho\sigma}$ and E_{σ} are components in the cartesian basis of the polarizability tensor and of the electric field vector of the incident radiation, respectively. The non-linear part $\mathfrak{p}^{\mathrm{NL}}$ gives rise to processes where in every event more than one photon are involved like hyper-Raman, hyper-Rayleigh and second hyper-Raman and second hyper-Rayleigh scattering. These are not considered here. However, in the process of laser induced fluorescence of CO also two photons are absorbed - but based on the permanent dipole part in Eq. (2.18).

Illumination-observation geometry In addition to energy characteristics, the scattered photons carry information on the symmetry of the scatterer in their state of polarization. The measured signal strength and state of polarization depend strongly on the actual illumination-observation geometry. A widely-used approach to account for this, is to introduce the concept of a scatter plane that is defined by the optical axis of observation and the propagation direction of the incident light. The illumination-observation geometry is shown in Fig. 2.1 and fully described by two angles θ, ϕ, and the polarization property of the incident light.

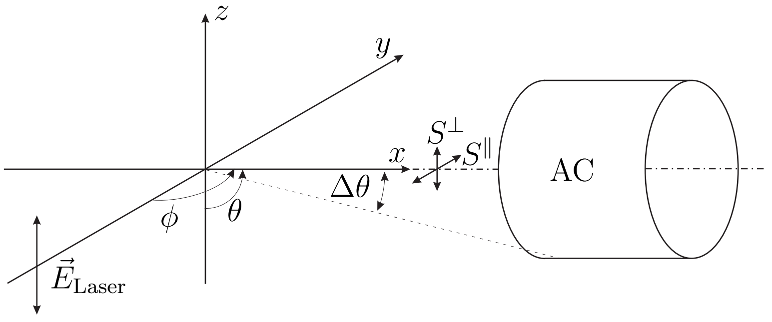

Figure 2.1: Scattering and detection geometry in present experiment defined by angles θ in the xz plane and ϕ in the xy plane (scatter plane). Linearly polarized laser light propagated in y direction with nonzero z component of the electric field vector $\vec{E}_{\mathrm{Laser}}$. The probe volumes were located ±3 mm along the y direction at the origin. The sum of perpendicular and parallel polarized components of the scattered light, $S^{\perp} + S^{\parallel}$, respectively, were collected by an achromatic lens (AC) centered on the x axis.

Generally, the scattered light is treated separately with respect to its polarization direction relative to the scatter plane by one perpendicular and one parallel component

$$S = S^{\perp} + S^{\parallel} \,. \tag{2.21}$$

Accordingly, proportionality of the scattered signal is given by

$$S^{\perp} \propto (\mathfrak{p}_0^{\perp})^2 \tag{2.22}$$

$$S^{\parallel} \propto (\mathfrak{p}_0^{\parallel})^2 \,. \tag{2.23}$$

Both components $\mathfrak{p}_0^{\perp}$ and $\mathfrak{p}_0^{\parallel}$ can be expressed as observation-angle dependent linear combinations of all three space-fixed components of $\mathfrak{p}_{\rho_0}$ by

$$\begin{aligned} \mathfrak{p}_0^{\perp} &= \mathfrak{p}_{x_0}(-\cos\theta)\sin\phi + \mathfrak{p}_{y_0}(-\cos\theta)(-\cos\phi) + \mathfrak{p}_{z_0}\sin\theta && (2.24)\\ &= -\mathfrak{p}_{x_0}\cos\theta\sin\phi + \mathfrak{p}_{y_0}\cos\theta\cos\phi + \mathfrak{p}_{z_0}\sin\theta && (2.25)\\ \mathfrak{p}_0^{\parallel} &= -\mathfrak{p}_{x_0}\cos\phi + \mathfrak{p}_{y_0}\sin\phi \,. && (2.26) \end{aligned}$$

Using the relation of the linear part in Eq. (2.20) and squaring yields

$$\begin{aligned} (\mathfrak{p}_0^{\perp})^2 &= (-\alpha_{\mathrm{xz}}E_{\mathrm{z_0}}\cos\theta\sin\phi + \alpha_{\mathrm{yz}}E_{\mathrm{z_0}}\cos\theta\cos\phi + \alpha_{\mathrm{zz}}E_{\mathrm{z_0}}\sin\theta)^2 && (2.27)\\ &= (\alpha_{\mathrm{xz}}^2\cos^2\theta\sin^2\phi + \alpha_{\mathrm{yz}}^2\cos^2\theta\cos^2\phi + \alpha_{\mathrm{zz}}^2\sin^2\theta \\ &\quad - 2\alpha_{\mathrm{xz}}\alpha_{\mathrm{yz}}\cos^2\theta\sin\phi\cos\phi - 2\alpha_{\mathrm{xz}}\alpha_{\mathrm{zz}}\sin\theta\cos\theta\sin\phi && (2.28)\\ &\quad + 2\alpha_{\mathrm{yz}}\alpha_{\mathrm{zz}}\sin\theta\cos\theta\cos\phi)E_{\mathrm{z_0}}^2 \end{aligned}$$

and

$$\begin{aligned} (\mathfrak{p}_0^{\parallel})^2 &= (-\alpha_{\mathrm{xz}}E_{\mathrm{z_0}}\cos\phi + \alpha_{\mathrm{yz}}E_{\mathrm{z_0}}\sin\phi)^2 && (2.29)\\ &= (\alpha_{\mathrm{xz}}^2\cos^2\phi + \alpha_{\mathrm{yz}}^2\sin^2\phi - 2\alpha_{\mathrm{xz}}\alpha_{\mathrm{yz}}\cos\phi\sin\phi)E_{\mathrm{z_0}}^2 \,. && (2.30) \end{aligned}$$

In order to account for freely in space oriented molecules, spatial averaging is applied to Eqs. (2.28) and (2.30) and is denoted by $\langle \ldots \rangle$. A general rule for resulting isotropic averages stated by Long [64, p.489] is that all isotropic averages which involve a subscript once, are zero. Hence, the squared perpendicular component becomes

$$(\mathfrak{p}_0^{\perp})^2 = [\,\langle\alpha_{\mathrm{xz}}^2\rangle\cos^2\theta\sin^2\phi + \langle\alpha_{\mathrm{yz}}^2\rangle\cos^2\theta\cos^2\phi + \langle\alpha_{\mathrm{zz}}^2\rangle\sin^2\theta\,]E_{\mathrm{z_0}}^2 \tag{2.31}$$

and the squared parallel component

$$(\mathfrak{p}_0^{\parallel})^2 = [\,\langle\alpha_{\mathrm{xz}}^2\rangle\cos^2\phi + \langle\alpha_{\mathrm{yz}}^2\rangle\sin^2\phi\,]E_{\mathrm{z_0}}^2 \,. \tag{2.32}$$

Finally, by using the symmetry property

$$\langle \alpha^2_{\mathrm{xz}} \rangle = \langle \alpha^2_{\mathrm{yz}} \rangle \tag{2.33}$$

both components are reduced to

$$(\mathfrak{p}_0^{\perp})^2 = [\, \langle \alpha^2_{\mathrm{yz}} \rangle \cos^2\theta + \langle \alpha^2_{\mathrm{zz}} \rangle \sin^2\theta \,] E^2_{\mathrm{z}_0} \tag{2.34}$$

$$(\mathfrak{p}_0^{\parallel})^2 = \langle \alpha^2_{\mathrm{yz}} \rangle E^2_{\mathrm{z}_0} \,. \tag{2.35}$$

Polarizability of molecules In order to obtain molecule- and transition-specific results for the quadratic products of isotropic averages of the type $\langle \alpha_{\rho\sigma} \alpha_{\bar{\rho}\bar{\sigma}} \rangle$ it proves useful to start with the matrix elements of polarizability in the molecule-fixed cartesian coordinate system which are expressed by

$$\left(\alpha_{(\underline{\rho\sigma})_{\mathrm{molfix}}} \right)_{fi} = \langle \Phi^f_{\mathrm{nuclei}} |\; \hat{\alpha}_{(\underline{\rho\sigma})_{\mathrm{molfix}}}(\psi_{\mathrm{electronic}}, \tilde{\nu}) \;| \Phi^i_{\mathrm{nuclei}} \rangle \,. \tag{2.36}$$

Components of the operator $\hat{\alpha}_{(\underline{\rho\sigma})_{\mathrm{molfix}}}$ depend on the electronic wavefunctions ψ and the wavenumber $\tilde{\nu}$ of the incident radiation. They can be calculated by quantum chemical *ab initio* computations within different orders of accuracy dependent on the used level of approximation, e.g. [31, 32, 50, 78]. As shown by Long [64, pp.154] using an irreducible spherical basis with especially simple transformation properties under rotation, a separation of rotational and vibrational parts in Eq. (2.36) according to Eq. (2.16) becomes possible. Then spatially averaged matrix elements for both parts can be derived separately. With the exception of asymmetric top molecules and special cases of angular momentum coupling, e.g. open shell molecules like molecular oxygen, general expressions for rotational quantum number dependencies are given in terms of Wigner 3-j symbols. Rotational selection rules are obtained from their properties and rotational quantum number dependencies are expressed quantitatively in terms of Placzek-Teller factors. Due to the spatial averaging process, particular components of the polarizability tensor are no longer accessible by experiment. Instead, the matrix elements of Eq. (2.36) are given in terms of tensor invariants which are related to the cartesian molecule-fixed components of $\hat{\alpha}_{(\underline{\rho\sigma})_{\mathrm{molfix}}}$ by

$$\overline{\alpha} = \tfrac{1}{3} \left(\alpha_{\underline{\mathrm{xx}}} + \alpha_{\underline{\mathrm{yy}}} + \alpha_{\underline{\mathrm{zz}}} \right) \,, \tag{2.37}$$

$$\begin{aligned} \Delta\alpha = \Big\{ & \tfrac{1}{2} \Big[(\alpha_{\underline{\mathrm{xx}}} - \alpha_{\underline{\mathrm{yy}}})^2 + (\alpha_{\underline{\mathrm{yy}}} - \alpha_{\underline{\mathrm{zz}}})^2 + (\alpha_{\underline{\mathrm{zz}}} - \alpha_{\underline{\mathrm{xx}}})^2 \Big] \\ & + \tfrac{3}{4} \Big[(\alpha_{\underline{\mathrm{xy}}} + \alpha_{\underline{\mathrm{yx}}})^2 + (\alpha_{\underline{\mathrm{xz}}} + \alpha_{\underline{\mathrm{zx}}})^2 + (\alpha_{\underline{\mathrm{yz}}} + \alpha_{\underline{\mathrm{zy}}})^2 \Big] \Big\}^{-1/2} \,. \end{aligned} \tag{2.38}$$

Herein, $\overline{\alpha}$ and $\Delta\alpha$ are denoted as mean and anisotropic polarizability, respectively, and the $\alpha_{\underline{\rho\sigma}}$ are a shorthand notation for the components of $\hat{\alpha}_{(\underline{\rho\sigma})_{\mathrm{molfix}}}$. In general, both invariants are functions of the motions of the nuclei and of the wavenumber $\tilde{\nu}$ of the incident radiation and appropriate labeling is also omitted for the sake of brevity. Then, transition-specific isotropic averages in the laboratory-fixed cartesian coordiante system are expressed by

$$\langle\alpha_{\mathrm{zz}}^2\rangle = (2J^i+1)\left[b^{(0)}_{J^fK^f:J^iK^i}\langle\phi^f_{\mathrm{vib}}|\,\overline{\alpha}\,|\phi^i_{\mathrm{vib}}\rangle^2 + b^{(2)}_{J^fK^f:J^iK^i}\tfrac{4}{45}\langle\phi^f_{\mathrm{vib}}|\,\Delta\alpha\,|\phi^i_{\mathrm{vib}}\rangle^2\right], \tag{2.39}$$

$$\langle\alpha_{\mathrm{yz}}^2\rangle = (2J^i+1)b^{(2)}_{J^fK^f:J^iK^i}\tfrac{1}{15}\langle\phi^f_{\mathrm{vib}}|\,\Delta\alpha\,|\phi^i_{\mathrm{vib}}\rangle^2 . \tag{2.40}$$

The degeneracy factor $(2J^i+1)$ of the rotational state of the molecule is included here because it follows directly from the spatial averaging of the rotational matrix element part. This degeneracy factor is, however, generally included into the fractional energy population factor f_i of the initial state and therefore omitted in the following, see Eq. (2.50) and text below. The $b^{(0)}_{J^fK^f:J^iK^i}$ and $b^{(2)}_{J^fK^f:J^iK^i}$ are the Placzek-Teller factors for symmetric top molecules. They can be found in Long [64, pp.162] and are listed here just in their most simple form in Table 2.1 for diatomic molecules, where the second rotational quantum number K is obsolete. Note that the vibrational wavefunctions ϕ_{vib} are generally not independent of the rotational state of the molecule. This type of vibration-rotation interaction needs to be taken into account to derive accurate signal strength of Raman scattering at elevated temperatures and was applied to Raman measurements in combustion science by Geyer [45]. Finally, Eqs. (2.34) and (2.35) expressed in terms of the experimentally accessible and transition-specific squared dipol moments are given by

$$\begin{aligned}(\mathfrak{p}_0^{\perp})^2_{fi} &= \langle\alpha^2_{fi}\rangle^{\perp}E^2_{\mathrm{z}_0}\\ &= \left[b^{(0)}_{J^fK^f:J^iK^i}\overline{\alpha}^2_{\mathrm{vib},fi}\sin^2\theta + b^{(2)}_{J^fK^f:J^iK^i}\Delta\alpha^2_{\mathrm{vib},fi}\left(\tfrac{4}{45}\sin^2\theta+\tfrac{3}{45}\cos^2\theta\right)\right]E^2_{\mathrm{z}_0}\,,\end{aligned} \tag{2.41}$$

$$\begin{aligned}(\mathfrak{p}_0^{\|})^2_{fi} &= \langle\alpha^2_{fi}\rangle^{\|}E^2_{\mathrm{z}_0}\\ &= b^{(2)}_{J^fK^f:J^iK^i}\tfrac{3}{45}\Delta\alpha^2_{\mathrm{vib},fi}\,E^2_{\mathrm{z}_0}\,.\end{aligned} \tag{2.42}$$

Vibrational matrix elements in Eqs. (2.39) and (2.40) were replaced by the short forms $\overline{\alpha}_{\mathrm{vib},fi}$ and $\Delta\alpha_{\mathrm{vib},fi}$, respectively. Most simple solutions of these matrix elements exist within the double harmonic approximation. This is expressed on the example of a diatomic molecule with the internuclear distance R and equilibrium distance R_{e}. Both, the mean and the anisotropic polarizability are functions of the internuclear distance R and they can be expanded as Taylor series. The vibrational matrix elements are then given by

$$\langle\phi^f_{\mathrm{vib}}|\,\overline{\alpha}\,|\phi^i_{\mathrm{vib}}\rangle = \overline{\alpha}_{\mathrm{vib},fi} \tag{2.43}$$

$$\approx \overline{\alpha}_{\mathrm{R_e}}\langle\phi^f_{\mathrm{vib}}|\,\phi^i_{\mathrm{vib}}\rangle + \left(\frac{\partial\overline{\alpha}}{\partial R}\right)_{\mathrm{R_e}}\langle\phi^f_{\mathrm{vib}}|\,(R-R_{\mathrm{e}})\,|\phi^i_{\mathrm{vib}}\rangle \tag{2.44}$$

$$\langle\phi^f_{\mathrm{vib}}|\,\Delta\alpha\,|\phi^i_{\mathrm{vib}}\rangle = \Delta\alpha_{\mathrm{vib},fi} \tag{2.45}$$

$$\approx \Delta\alpha_{\mathrm{R_e}}\langle\phi^f_{\mathrm{vib}}|\,\phi^i_{\mathrm{vib}}\rangle + \left(\frac{\partial\Delta\alpha}{\partial R}\right)_{\mathrm{R_e}}\langle\phi^f_{\mathrm{vib}}|\,(R-R_{\mathrm{e}})\,|\phi^i_{\mathrm{vib}}\rangle \tag{2.46}$$

The exact solution of these vibrational matrix elements based on harmonic oscillator wavefunctions can be found in, e.g. Struve [91, pp.89] and are given in terms of the vibrational quantum numbers of the final and initial state v^f and v^i, respectively, by

$$\langle \phi^f_{\text{vib}} | \, \phi^i_{\text{vib}} \rangle = \begin{cases} 0 & \text{for} \quad v^f \neq v^i \\ 1 & \text{for} \quad v^f = v^i : \text{Rayleigh} \end{cases} \tag{2.47}$$

$$\langle \phi^f_{\text{vib}} | \, R \, | \phi^i_{\text{vib}} \rangle = \begin{cases} 0 & \text{for} \quad v^f = v^i \\ (v^i + 1)^{1/2} b_v & \text{for} \quad v^f = v^i + 1 : \text{Raman Stokes} \\ (v^i)^{1/2} b_v & \text{for} \quad v^f = v^i - 1 : \text{Raman Anti-Stokes} \end{cases} \tag{2.48}$$

with

$$b_v = \left(\frac{h}{8\pi^2 c_0 (\tilde{\nu}_f - \tilde{\nu}_i)} \right)^{1/2} \tag{2.49}$$

However, anharmonicities using terms up to third order derivatives and vibration-rotation interaction were considered for molecular nitrogen and oxygen by Buldakov et al. [26] and were applied subsequently by Geyer [45]. For molecular hydrogen even matrix elements from highly accurate *ab intio* methods were taken based on 484 nm incident radiation and were converted to 532 nm using the dispersion relation given by Pecul and Rizzo [78]. These *ab intio* results were later refined for incident radiation of 532 nm for hydrogen and *ab intio* results for nitrogen were found in agreement with the perturbation based results in the diploma thesis by the author of this work [39] within a difference of up to +1 % at 2500 K in the integrated Raman cross section. Solutions of the double harmonic approximation are used here in Section 2.5 for considerations of the Rayleigh cross section.

Table 2.1: Placzek-Teller factors representing the rotational quantum number dependencies of squared rotational matrix elements. Here just listed for the simplest case which is applicable to molecules with two degenerate modes of rotation where $\Delta K = K^i = K^f = 0$ and closed electron shell.

Branch	ΔJ	$b^{(0)}_{J^f K^f : J^i K^i}$	$b^{(2)}_{J^f K^f : J^i K^i}$
Q	0	1	$\frac{J(J+1)}{(2J-1)(2J+3)}$
S	+2	0	$\frac{3(J+1)(J+2)}{2(2J+1)(2J+3)}$
O	−2	0	$\frac{3J(J-1)}{2(2J-1)(2J+1)}$

Population of energy eigenstates Self-evident, in an ensemble of particles the probability of specific energy transitions $f \leftarrow i$ is directly proportional to the number of particles in the corresponding initial state i. For molecules and atoms being in thermal equilibrium the population of particular energy eigenstates E_i is expressed by the Boltzmann distribution $f_i(T)$. Consequently, the number of particles in the initial state i is given by

$$\begin{aligned} N_i(T,p) &= N(T,p) f_i(T) \\ &= N(T,p) \frac{g_i \exp(-E_i/kT)}{Q(T)} \end{aligned} \tag{2.50}$$

with N being the total number of particles within the considered volume at temperature T and pressure p, g_i is the overall degeneracy, k the Boltzmann constant[‡], and the partition function Q defined as

$$Q(T) = \sum_j g_j \exp(-E_j/kT)\,. \tag{2.51}$$

Note that just relative energies between all states must be consistent because the zero-point energy cancels out in Eq. (2.50). The overall degeneracy is generally composed of factors from all degenerate energy eigenstates and for example in case of homonuclear diatomic molecules with non degenerate ground state given by

$$g_i = g_N g_J\,. \tag{2.52}$$

Herein, g_N is the nuclear statistical weight[§] and g_J the degeneracy factor $(2J^i + 1)$ which was omitted in Eqs. (2.41) and (2.42). The number of molecules m in the probe volume[¶] V_{probe} is expressed by

$$\begin{aligned} N(T,p) &= N_{\text{L}} X_m V_{\text{probe}} \frac{T_0}{T} \frac{p}{p_0} \\ &= N_{\text{L}} X_m A_{\text{probe}} l_{\text{probe}} \frac{T_0}{T} \frac{p}{p_0}\,. \end{aligned} \tag{2.53}$$

Herein, N_{L} is the Loschmidt-number[‖], X_m is the mole fraction of molecule m, A_{probe} and l_{probe} are the cross-sectional area and length of the probe volume, respectively.

Connecting quantum mechanics and electrodynamics In order to obtain the number of scattered photons per time from specific energy transitions fi with corresponding wavenumber $\tilde{\nu}_{\text{S}}$, the classical squared dipole moment $p_0^2 \sin^2\theta$ in Eq. (2.12) needs to be substituted by $N_i\big[(\mathfrak{p}_0^{\perp})^2_{fi} + (\mathfrak{p}_0^{\parallel})^2_{fi}\big]$ from Eqs. (2.41), (2.42) and (2.50), correspondingly. The wavenumber $\tilde{\nu}_{\text{S}}$ of the scattered photons is determined by the difference between the energy of the incident photon and a possible change in the eigenenergy of the molecule ΔE_{fi} due

---

[‡] $k = 1.3806504(24) \cdot 10^{-23}\,\text{JK}^{-1}$

[§] e.g. $^{14}N_2$: $g_N = 6$ for even J, and $g_N = 3$ for odd J

[¶] Volume enclosing 95 % of signal: $A_{\text{probe}} l_{\text{probe}} = \pi(150\,\mu\text{m})^2 \cdot 102.6\,\mu\text{m} = 7.2524 \cdot 10^{-3}\,\text{mm}^3$

[‖] $N_L = 2.6867774(47) \cdot 10^{25}\,\text{m}^{-3}$

to the interaction of the photon with the molecule. Those characteristic transitions are denoted as Raman shift and are commonly expressed in wavenumbers by

$$\Delta\tilde{\nu}_{fi} = \tilde{\nu}_f - \tilde{\nu}_i \begin{cases} > 0 : & \text{Raman Stokes} \\ = 0 : & \text{Rayleigh} \\ < 0 : & \text{Raman Anti-Stokes} \end{cases} \tag{2.54}$$

Consequently, for the wavenumber of the scattered photons $\tilde{\nu}_\mathrm{S}$ follows

$$\tilde{\nu}_\mathrm{S} = \tilde{\nu}_\mathrm{Laser} - \Delta\tilde{\nu}_{fi}\,. \tag{2.55}$$

It proves useful to express the amplitude of the electric field vector in terms of the total laser single-shot energy[‡] $\mathfrak{E}_\mathrm{Laser}$ by

$$E^2_{\mathrm{z}_0} = \frac{2\mathfrak{E}_\mathrm{Laser}}{\tau_\mathrm{pulse} A_\mathrm{probe} c_0 \varepsilon_0} \tag{2.56}$$

where τ_pulse is the temporal pulse width of the laser beam[§]. Accordingly, the differential number of scattered photons per laser single-shot and transition fi into $\mathrm{d}\Omega$ is obtained from Eq. (2.12) with appropriate replacements outlined above by

$$\frac{\partial \mathfrak{N}_{\mathrm{photons},fi}}{\partial\Omega} = \frac{\partial S(\mathfrak{p}_0, \tilde{\nu}_\mathrm{S})}{\partial\Omega}\tau_\mathrm{pulse} \tag{2.57}$$

$$\begin{aligned} &= \frac{\pi^2}{\varepsilon_0^2 h c_0}\frac{T_0}{T}\frac{p}{p_0} N_\mathrm{L} X_m l_{probe} \mathfrak{E}_\mathrm{Laser} \\ &\times \frac{\partial\sigma_{fi,m}(T)}{\partial\Omega}\frac{1}{(\tilde{\nu}_\mathrm{Laser} - \Delta\tilde{\nu}_{fi,m})} \end{aligned} \tag{2.58}$$

with the differential scattering cross section per transition and single molecule defined as

$$\frac{\partial\sigma_{fi,m}(T)}{\partial\Omega} = f_{i,m}(T)(\tilde{\nu}_\mathrm{Laser} - \Delta\tilde{\nu}_{fi,m})^4 \left[\langle\alpha^2_{fi,m}\rangle^\perp + \langle\alpha^2_{fi,m}\rangle^\parallel\right]\,. \tag{2.59}$$

Integration of solid angle In order to obtain integral photon numbers per laser single-shot for actual experimental conditions, integration is applied for components in Eq. (2.58) which depend on $\mathrm{d}\Omega$, namely $\langle\alpha^2_{fi}\rangle^\perp$ and $\langle\alpha^2_{fi}\rangle^\parallel$. The corresponding angular dependent integral form for the perpendicular polarized component is expressed by

$$\langle\alpha^2_{fi}\rangle^\perp_\Omega = \int \mathrm{d}\Omega \left[b^{(0)}_{J^fK^f:J^iK^i}\overline{\alpha}^2_{\mathrm{vib},fi}\sin^2\theta + b^{(2)}_{J^fK^f:J^iK^i}\Delta\alpha^2_{\mathrm{vib},fi}\left(\tfrac{4}{45}\sin^2\theta + \tfrac{3}{45}\cos^2\theta\right)\right] \tag{2.60}$$

[‡] $\mathfrak{E}_\mathrm{Laser}$ is up to 1.8 J/pulse

[§] $\Delta\tau_\mathrm{pulse} = 500\,\mathrm{ns}$ (FWHM) and for the parallel polarized component by

$$\langle \alpha_{fi}^2 \rangle_\Omega^\parallel = \int \mathrm{d}\Omega \, b^{(2)}_{J^fK^f:J^iK^i} \tfrac{3}{45} \Delta\alpha^2_{\mathrm{vib},fi} \,. \tag{2.61}$$

Integration is applied over a circle with radius $\Delta\theta$ on the surfaces defined by Eqs. (2.60) and (2.61). Values of ϕ describing a circle centered at $\phi_0 = \pi/2$ and $\theta_0 = \pi/2$ are expressed as a function of θ and radius $\Delta\theta$ by

$$\phi_{\mathrm{circle}}(\theta) = \pi/2 \pm \sqrt{(\Delta\theta)^2 - (\theta - \pi/2)^2} \,. \tag{2.62}$$

Using the fourfold symmetry of that circle Eqs. (2.60) and (2.61) in definite integral form are then given for the perpendicular component by

$$\begin{aligned}\langle \alpha_{fi}^2 \rangle_{\Delta\Omega}^\perp = 4 \int_{\frac{\pi}{2}}^{\frac{\pi}{2}+\sqrt{(\Delta\theta)^2-(\theta-\frac{\pi}{2})^2}} \mathrm{d}\phi \int_{\frac{\pi}{2}}^{\frac{\pi}{2}+\Delta\theta} \mathrm{d}\theta \Big[b^{(0)}_{J^fK^f:J^iK^i} \overline{\alpha}^2_{\mathrm{vib},fi} \sin^3\theta \\ + b^{(2)}_{J^fK^f:J^iK^i} \Delta\alpha^2_{\mathrm{vib},fi} \left(\tfrac{4}{45} \sin^3\theta + \tfrac{3}{45} \cos^2\theta \sin\theta \right) \Big] \,,\end{aligned} \tag{2.63}$$

and for the parallel component by

$$\langle \alpha_{fi}^2 \rangle_{\Delta\Omega}^\parallel = 4 \int_{\frac{\pi}{2}}^{\frac{\pi}{2}+\sqrt{(\Delta\theta)^2-(\theta-\frac{\pi}{2})^2}} \mathrm{d}\phi \int_{\frac{\pi}{2}}^{\frac{\pi}{2}+\Delta\theta} \mathrm{d}\theta \, b^{(2)}_{J^fK^f:J^iK^i} \tfrac{3}{45} \Delta\alpha^2_{\mathrm{vib},fi} \sin\theta \,. \tag{2.64}$$

Solving of the integrals yields factors for each of the terms in Eqs. (2.63) and (2.64). These are listed for the used achromatic collection lens with f-number of two and a corresponding $\Delta\theta$[‡]

$$\Delta\Omega_1 = 4 \int_{\frac{\pi}{2}}^{\frac{\pi}{2}+\Delta\theta} \mathrm{d}\theta \sqrt{(\Delta\theta)^2 - \left(\theta - \frac{\pi}{2}\right)^2} \sin^3\theta = 0.18437 \tag{2.65}$$

$$\Delta\Omega_2 = 4 \int_{\frac{\pi}{2}}^{\frac{\pi}{2}+\Delta\theta} \mathrm{d}\theta \sqrt{(\Delta\theta)^2 - \left(\theta - \frac{\pi}{2}\right)^2} \cos^2\theta \sin\theta = 0.00275883 \tag{2.66}$$

$$\Delta\Omega_3 = 4 \int_{\frac{\pi}{2}}^{\frac{\pi}{2}+\Delta\theta} \mathrm{d}\theta \sqrt{(\Delta\theta)^2 - \left(\theta - \frac{\pi}{2}\right)^2} \sin\theta = 0.187129 \,. \tag{2.67}$$

Insertion of Eqs. (2.65) to (2.67) into Eqs. (2.63) and (2.64) gives for the perpendicular polarized component

$$\langle \alpha_{fi}^2 \rangle_{\Delta\Omega}^\perp = \left[b^{(0)}_{J^fK^f:J^iK^i} \overline{\alpha}^2_{\mathrm{vib},fi} \Delta\Omega_1 + b^{(2)}_{J^fK^f:J^iK^i} \Delta\alpha^2_{\mathrm{vib},fi} \left(\tfrac{4}{45} \Delta\Omega_1 + \tfrac{3}{45} \Delta\Omega_2 \right) \right] \,, \tag{2.68}$$

[‡] $\Delta\theta = \arctan(0.5/f/\#) = 0.245$

and for the parallel polarized component

$$\langle \alpha_{fi}^2 \rangle_{\Delta\Omega}^{\parallel} = b^{(2)}_{J^f K^f : J^i K^i} \tfrac{3}{45} \Delta\alpha^2_{\mathrm{vib},fi} \Delta\Omega_3 \,. \tag{2.69}$$

Number of photons from Raman/Rayleigh scattering Finally, it is possible to give the equation describing the laser-shot average number of photons per transition $f \leftarrow i$ and molecule m that is scattered onto the effective surface of the first collection lens due to the Raman/Rayleigh effect by

$$\begin{aligned} \mathfrak{N}_{\mathrm{photons},fi}(T,m) = {} & \frac{\pi^2 N_{\mathrm{L}} T_0}{\varepsilon_0^2 h c_0 p_0} \\ & \times \frac{p}{T} X_m l_{probe} \mathfrak{E}_{\mathrm{Laser}} \\ & \times \left\{ f_i(T) (\tilde{\nu}_{\mathrm{Laser}} - \Delta\tilde{\nu}_{fi})^3 \left[\langle \alpha_{fi}^2 \rangle_{\Delta\Omega}^{\perp} + \langle \alpha_{fi}^2 \rangle_{\Delta\Omega}^{\parallel} \right] \right\}_m \end{aligned} \tag{2.70}$$

The fraction in the first line is composed of physical constants. The second line determines experimental conditions. And the term in the last line is apart from $\tilde{\nu}_{\mathrm{Laser}}$ only molecule-specific. Note that $\langle \alpha_{fi}^2 \rangle$ depends also on the wavenumber of the laser $\tilde{\nu}_{\mathrm{Laser}}$ which is not explicitly labeled. Figure 2.2 shows the resulting photon numbers per transition for N_2 at 2000 K for both polarization components versus the Raman shift defined in Eq. (2.54) with matrix elements of polarizability from *ab initio* results, presented in [39].

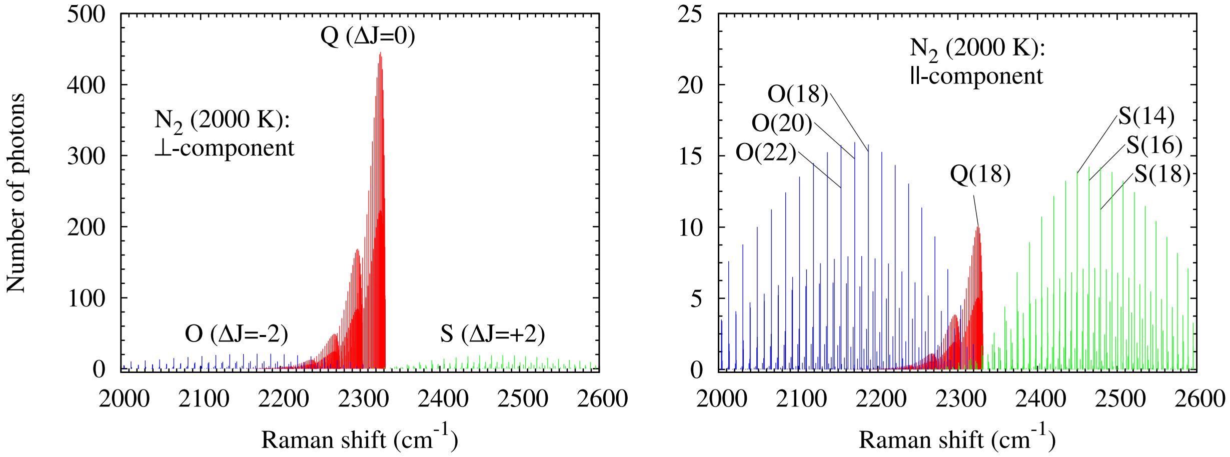

Figure 2.2: Calculated number of scattered Raman photons per transition into present solid angle, $\mathfrak{N}^{\perp}_{\mathrm{photons},fi}$ and $\mathfrak{N}^{\parallel}_{\mathrm{photons},fi}$, for N_2 at 2000 K and 101.325 kPa shown as stick spectra for both polarization directions. Based on $\mathfrak{E}_{\mathrm{Laser}} = 1.8$ J/pulse ($4.82 \cdot 10^{18}$ photons at 532 nm), $l_{\mathrm{probe}} = 102\,\mu$m, and $X_{\mathrm{N_2}} = 1$. Rovibrational transitions are denoted as $\mathrm{O}(J^i)$ etc. and refer to $v^i = 0$.

2.4 Raman species measurement

In order to make the calculated photon numbers from particular transitions comparable to experimental data, each Raman transition is convolved with an experimentally determined apparatus function. This apparatus function dominates all other linewidth effects like Doppler or pressure broadening. Finally, all convolved Raman transitions are superposed, resulting in rovibrational Raman bands. A spectral library is composed of these temperature-dependent Raman bands.

2.4.1 Convolution of calculated spectra

To get calculated spectra which can be used for comparison with experimental spectra every single transition strength expressed by the calculated number of photons $\mathfrak{N}_{\mathrm{photons},fi}$ of molecule m and temperature T in Eq. (2.70) is convolved with an apparatus function Γ_{app}. This is expressed by

$$\mathcal{S}_{fi}(\tilde{\nu},T,m)=\mathfrak{N}_{\mathrm{photons},fi}(\tilde{\nu}_{\mathrm{S}},T,m)\cdot\Gamma_{\mathrm{app}}(\tilde{\nu}-\tilde{\nu}_{\mathrm{S}})\,. \tag{2.71}$$

With the present dispersion, spectral separation of lines from specific transitions fi is just provided for a few lines from molecular hydrogen. Generally, single transitions fi strongly overlap. This is accounted for by the superposition of all convolved transitions by

$$\mathcal{S}_{\Sigma fi}(\tilde{\nu},T,m)=\sum_{fi}\mathfrak{N}_{\mathrm{photons},fi}(\tilde{\nu}_{\mathrm{S}},T,m)\cdot\Gamma_{\mathrm{app}}(\tilde{\nu}-\tilde{\nu}_{\mathrm{S}})\,. \tag{2.72}$$

Note that $\tilde{\nu}_{\mathrm{S}}$, definded by Eq. (2.55), is fi-specific. This Eq. (2.72) is solved in spectral Ramanpixel-space using the discrete function Γ_{app} from the experiment with linear interpolation used between two adjacent Ramanpixels. The dispersion is nonlinear along all 1300 spectral Ramanpixels. This is accounted for by a third-order polynomial fit on spectral emission lines of a Neon lamp given by

$$P_{\mathrm{pixel}}(\tilde{\nu})=C_3\tilde{\nu}^3+C_2\tilde{\nu}^2+C_1\tilde{\nu}+C_0\,. \tag{2.73}$$

Finally, resulting spectra in Ramanpixel-space for each of the seven molecules are obtained from

$$\mathcal{S}_{\Sigma fi}(P_{\mathrm{pixel}},T,m)=\sum_{fi}\mathfrak{N}_{\mathrm{photons},fi}(P_{\mathrm{pixel}}(\tilde{\nu}_{\mathrm{S}}),T,m)\cdot\Gamma_{\mathrm{app}}(P_{\mathrm{pixel}}(\tilde{\nu})-P_{\mathrm{pixel}}(\tilde{\nu}_{\mathrm{S}}))\,. \tag{2.74}$$

Resulting spectra from this Eq. (2.74) composed of rovibrational Raman bands for the molecules CO_2, O_2, CO, N_2, CH_4, H_2O, and H_2 provided the base for the present work.

2.4.2 Raman response and crosstalk

An often used term in this work is the Raman response and crosstalk. The non-normalized Raman response $\tilde{c}_{ii}$ of molecule i describes the molecule-specific temperature dependence of the Raman signal within particular binning regions from $br_{\text{start}}(i)$ to $br_{\text{end}}(i)$ of spectral Raman pixels and is defined by

$$\tilde{c}_{ii}(T,i) = \sum_{br_{\text{start}}(i)}^{br_{\text{end}}(i)} \frac{T}{T_0} \mathcal{S}_{\Sigma fi}(P_{\text{pixel}}, T, i)\,. \tag{2.75}$$

Herein, i are numbers from 1 to 7 denoting the molecules in the order of increasing rovibrational Raman shifts: CO_2, O_2, CO, N_2, HCs, H_2O, and H_2. Note that the decrease in signal to higher temperatures due to the decrease in number density is excluded by the first fraction in the sum. The Raman response is obtained from Eq. (2.75) by simple normalization

$$c_{ii}(T,i) = \frac{\tilde{c}_{ii}(T,i)}{\tilde{c}_{ii}(T_{\text{norm}},i)} \tag{2.76}$$

where here $T_{\text{norm}} = 290\,\text{K}$ was used.

The Raman crosstalk is denoted by '$i{\leftarrow}j$'. For example, CO_2 crosstalk onto the O_2 channel is denoted $O_2{\leftarrow}CO_2$. The non-normalized Raman crosstalk onto molecule i is defined for all $j \neq i$ by

$$\tilde{c}_{ij}(T, i{\leftarrow}j) = \sum_{br_{\text{start}}(i)}^{br_{\text{end}}(i)} \frac{T}{T_0} \mathcal{S}_{\Sigma fi}(P_{\text{pixel}}, T, j) \tag{2.77}$$

and the Raman crosstalk, correspondingly, is defined by

$$c_{ij}(T, i{\leftarrow}j) = \frac{\tilde{c}_{ij}(T, i{\leftarrow}j)}{\tilde{c}_{ij}(T_{\text{norm}}, i{\leftarrow}j)}\,. \tag{2.78}$$

2.5 Rayleigh temperature measurement

The Rayleigh temperature for a mixture of species follows straightforwardly from Eq. (2.70) and is expressed for convenience in terms of the Rayleigh scattering cross section given by

$$T_{\text{Ray}} = c_{\text{Ray,calib}} \frac{\sum_i X_i \sigma_{\text{Ray},i}}{S_{\text{Ray}}}\,, \tag{2.79}$$

with $c_{\text{Ray,calib}}$ and S_{Ray} being the Rayleigh calibration constant and measured signal, X_i and $\sigma_{\text{Ray},i}$ mole fractions and the Rayleigh scattering cross sections of species i, respectively. The mole fractions X_i are determined simultaneously via Raman scattering. The Rayleigh scattering cross sections $\sigma_{\mathrm{Ray},i}$ of all species i must be known, either from measurements or quantum chemical *ab initio* calculations. The calibration constant is generally determined in air or cold gases using the known temperature from the thermocouple. It should be noted that the Rayleigh signal scales with the third power of the laser wavenumber $\tilde{\nu}_{\mathrm{Laser}}$ according to Eq. (2.70) - and not with the fourth power as one might expect from Eq. (2.79). In order to derive particular Rayleigh scattering cross sections, the next section treats the Rayleigh process in a more generalized way.

2.5.1 Rayleigh scattering cross section

The differential scattering cross section per single molecule and transition fi was introduced in Eq. (2.59) and is defined as

$$\frac{\partial \sigma_{fi}}{\partial \Omega} = \frac{\pi^2}{\varepsilon_0^2} f_i(T)(\tilde{\nu}_{\mathrm{Laser}} - \Delta\tilde{\nu}_{fi})^4 \left[\langle \alpha_{fi}^2 \rangle^{\perp} + \langle \alpha_{fi}^2 \rangle^{\parallel}\right] \tag{2.80}$$

where the molecule index m was omitted. The polarizabilities $\langle \alpha_{fi}^2 \rangle^{\perp}$ and $\langle \alpha_{fi}^2 \rangle^{\parallel}$ are given by Eqs. (2.41) and (2.42) and add up to

$$\langle \alpha_{fi}^2 \rangle^{\perp+\parallel} = \overline{\alpha}_{fi}^2 \sin^2\theta + b^{(2)}_{J^fK^f:J^iK^i} \Delta\alpha_{fi}^2 \left(\tfrac{3}{45} + \tfrac{4}{45}\sin^2\theta + \tfrac{3}{45}\cos^2\theta\right) . \tag{2.81}$$

For the considerations in this section the angular dependence is not important. It is neglected and $\theta = \pi/2$. Furthermore, matrix elements of polarizabilities are simplified by application of the double harmonic approximation given by Eqs. (2.44), (2.46), and (2.47). This yields[‡]

$$\langle \alpha_{fi}^2 \rangle^{\perp+\parallel} = \overline{\alpha}_{\mathrm{R_e}}^2 + b^{(2)}_{J^fK^f:J^iK^i} \tfrac{7}{45} \Delta\alpha_{\mathrm{R_e}}^2 . \tag{2.82}$$

By using the sum property of the Placzek-Teller factor

$$\sum_{J^fK^f} b^{(2)}_{J^fK^f:J^iK^i} = 1 \tag{2.83}$$

Equation (2.82) reduces further to

$$\langle \alpha_{fi}^2 \rangle^{\perp+\parallel} = \overline{\alpha}_{\mathrm{R_e}}^2 + \tfrac{7}{45} \Delta\alpha_{\mathrm{R_e}}^2 \tag{2.84}$$

which can be understood as the source of scattered light composed of three different components, reviewed by Miles et al. [71]: Placzek trace scattering, Q-branch rotational Raman scattering, and O- and S-branches rotational Raman scattering. To separate the three parts it is necessary to introduce approximations for the transition-specific Placzek-Teller factors. Hence, from fractional population weighted J-averaging of the forms given in

---

[‡] Vibrational Raman scattering is $\sim 10^{-3}$ smaller and is also neglected

Table 2.1, and averaging over n_T temperatures in the range from 290 K to 2500 K follows

$$\overline{b^{(2)}_{J^i:J^i}} = \frac{1}{n_T}\sum_T \left[\sum_{J^i}\left(\sum_v f_{v^i J^i}(T)\right)\cdot b^{(2)}_{J^i:J^i}\right] \approx \frac{1}{4} \tag{2.85}$$

$$\overline{b^{(2)}_{J^i+2:J^i} + b^{(2)}_{J^i-2:J^i}} = \frac{1}{n_T}\sum_T \left[\sum_{J^i}\left(\sum_v f_{v^i J^i}(T)\right)\cdot \left(b^{(2)}_{J^i+2:J^i} + b^{(2)}_{J^i-2:J^i}\right)\right] \approx \frac{3}{4} \tag{2.86}$$

within a maximum error of <3 % for nitrogen and <30 % for hydrogen, with both errors decreasing at higher temperatures. The three components of the Rayleigh scattering are then obtained from

$$\langle \alpha^2_{fi}\rangle^{\perp+\parallel} = \begin{cases} \overline{\alpha}^2_{\mathrm{R_e}} & : \quad \text{Placzek trace} \\ \frac{7}{180}\Delta\alpha^2_{\mathrm{R_e}} & : \quad \text{Raman Q} \\ \frac{21}{180}\Delta\alpha^2_{\mathrm{R_e}} & : \quad \text{Raman O+S} \end{cases} \tag{2.87}$$

These values agree to the values of Kattawar et al. [57] summarized by Miles et al. [71, Table 4]. Commonly, Rayleigh scattering cross sections are expressed in terms of the depolarization ratio ρ instead of the anisotropic polarizabilities $\Delta\alpha$. Both are for linearly polarized incident radiation and observation at $\theta = \pi/2$ related by

$$\rho = \frac{3\Delta\alpha^2}{45\overline{\alpha}^2 + 4\Delta\alpha^2} \tag{2.88}$$

Insertion of Eq. (2.88) in Eq. (2.84) yields

$$\langle \alpha^2_{fi}\rangle^{\perp+\parallel} = \overline{\alpha}^2_{\mathrm{R_e}}\left(1 + \frac{7\rho}{3-4\rho}\right) \tag{2.89}$$

The mean polarizability is related to the index of refraction, n, by the Lorentz-Lorenz equation [71]

$$\overline{\alpha}_{\mathrm{R_e}} = \frac{3\varepsilon_0}{N}\frac{n^2-1}{n^2+2} \tag{2.90}$$

where N is the number density of a single-species gas at conditions in consistence with those of the index of refraction n. Using Eq. (2.89) in Eq. (2.80) the differential Rayleigh scattering cross section including all three components listed in Eq. (2.87) is

$$\frac{\partial\sigma}{\partial\Omega} = \frac{\pi^2}{\varepsilon_0^2}\tilde{\nu}^4_{\mathrm{Laser}}\overline{\alpha}^2_{\mathrm{R_e}}\left(1 + \frac{7\rho}{3-4\rho}\right) \tag{2.91}$$

where an average for $\overline{(\tilde{\nu}_{\mathrm{Laser}} - \Delta\tilde{\nu}_{fi})^4} \approx \tilde{\nu}^4_{\mathrm{Laser}}$ was used. Note that due to the double harmonic approximation the polarizability is no longer transition-specific and the fractionial population $f_i(T)$ becomes obsolete as well. In order to express $\overline{\alpha}^2_{\mathrm{R_e}}$ in terms of the index of refraction relation in Eq. (2.90), $n \approx 1$ for gases yields the approximation [71]

$$\left(\frac{n^2-1}{n^2+2}\right)^2 \approx \frac{4}{9}\left(\frac{n-1}{1}\right)^2 \tag{2.92}$$

and the differential Rayleigh scattering cross section including all three components is given by

$$\frac{\partial\sigma}{\partial\Omega} = 4\pi^2\tilde{\nu}^4_{\text{Laser}}\left(\frac{n-1}{N}\right)^2\left(1+\frac{7\rho}{3-4\rho}\right) \tag{2.93}$$

It proves useful for molecules with large rotational constants and therefore well separated rotational lines like hydrogen for example, to exclude the rotational Raman O- and S-branches contribution according to the rotational average factors summarized in Eq. (2.87). This yields the differential Rayleigh scattering cross section without scattering from rotational Raman O- and S-branches

$$\frac{\partial\sigma}{\partial\Omega} = 4\pi^2\tilde{\nu}^4_{\text{Laser}}\left(\frac{n-1}{N}\right)^2\left(1+\frac{7\rho}{4(3-4\rho)}\right) \tag{2.94}$$

So far, the introduced approximations led to temperature-insensitive Rayleigh scattering cross sections. For most Rayleigh scattering based temperature measurements this is adequate in comparison to accuracies mostly in the order of 5 % or worse due to the unknown local species composition and concomittant variations in the Rayleigh cross section. However, if Raman measurements are applied simultaneously, the local composition of major species is known and can be used to correct the measured Rayleigh temperature according to Eq. (2.79). Then, small descrepancies in Rayleigh scattering cross sections may become important for specific flame conditions. This is discussed in more depth in Section 2.5.2. In this work, Rayleigh scattering cross sections were derived for a number of typical species occurring in combustion processes. These are presented in Section 4.3.3.

2.5.2 Temperature dependence of Rayleigh cross sections of H_2 and N_2 from *ab initio* calculations

As outlined in Section 2.5.1 Rayleigh cross sections within the double harmonic approximation have lost their temperature dependence. Following the *ab initio* procedure outlined in Section 3.3.4 and considering the Rayleigh $i \leftarrow i$ transitions and Raman pure rotational transitions yields the accurate integrated temperature dependence of the Rayleigh scattering cross section according to Eq. (2.80). Results for H_2 and N_2 are shown in Fig. 2.3 relative to their cross sections at 290 K. In addition, results derived from the semiempirical perturbation approach of Buldakov et al. [26], applied by Geyer [45], are shown and excellent agreement is found for N_2 and agreement within 0.02 is observed for H_2. The impact on Rayleigh temperature measurements can be directly estimated using Eq. (2.79) by simple multiplication with corresponding mole fractions of the considered species. This

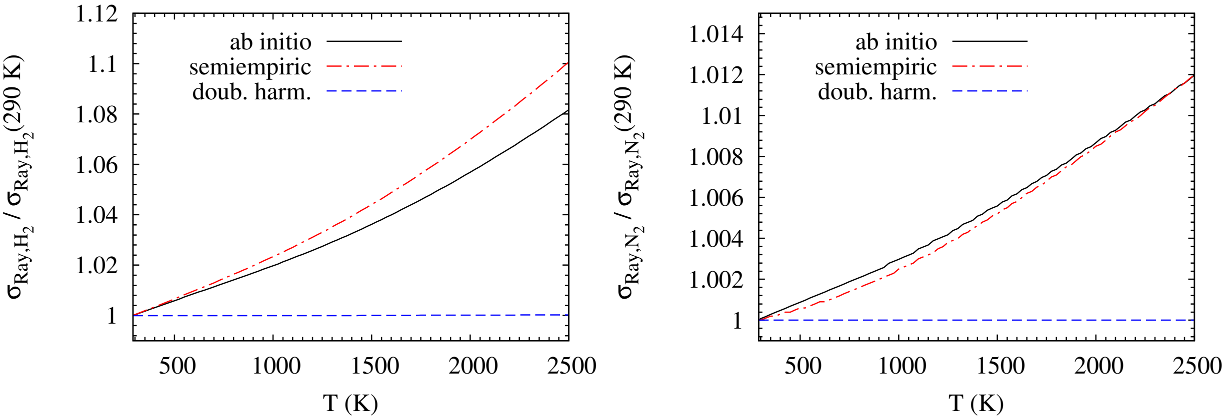

Figure 2.3: Temperature dependence of Rayleigh scattering cross section of H_2 and N_2 relative to 290 K from quantum chemical *ab initio* calculations and semiempirical perturbation approach. In contrast, the double harmonic approximation with no temperature dependence intrinsically.

was investigated by Sutton et al. [92] considering most relevant combustion species based on experimental (up to 1100 K) and semiempirical results of Hohm and Kerl [52]. For present calculations shown in Fig. 2.3, good agreement is found for N_2 with an increase of 0.4 % per 1000 K reported by Sutton et al. [92, Table 2]. Their value for H_2 is 2.8 % per 1000 K and good agreement is observed with the lower value of the *ab initio* calculations in Fig. 2.3. Sutton et al. studied the effect in the post-flame region of a premixed propane/air flame at different equivalence ratios and found a temperature correction of up to +2 % at stoichiometric condition. In hydrogen diffusion flames, the impact might be even more significant and would reach up to 3 % underestimation of the Rayleigh temperature due to large amounts of H_2 (>20 %) and H_2O (>30 %) at tempertures above 2000 K, e.g. see Figs. 3.7 and 3.14. However, experimental results presented in this work had a different focus and the molecule-specific temperature dependence of Rayleigh cross sections was not considered in the data evaluation.

2.6 Experimental setup

Line-imaged multi-scalar measurements were conducted at the Combustion Research Facility of the Sandia National Laboratories. Most recent descriptions of the experimental setup were reported by Karpetis and Barlow [14, 56].

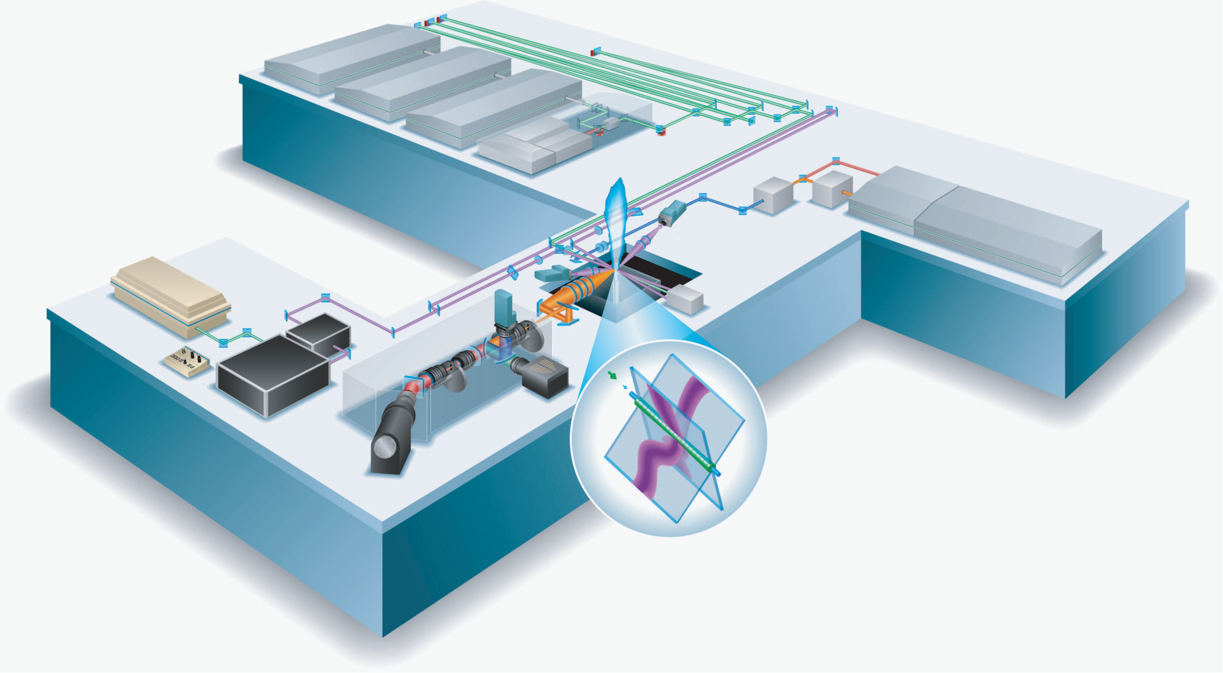

Figure 2.4: Experimental setup at the Combustion Research Facility of the Sandia National Laboratories for one-dimensional detection of seven major species (CO_2, O_2, CO, N_2, HCs, H_2O, H_2) and temperature by excitation at 532 nm (green), and CO-LIF excited at 230.1 nm (UV, but denoted as blue beam in the figure) for low number densities of CO. The Raman camera is positioned at the front edge, the CO-LIF camera on top, and the Rayleigh camera at the right edge of the detection unit, respectively. Simultaneous planar imaging of OH fluorescence from two crossed laser sheets, and line imaging of NO-LIF, both also shown in the figure, were not used in this work.

2.6.1 Excitation

Raman/Rayleigh Raman and Rayleigh scattering was excited by a cluster of four sequentially fired (150 ns) frequency-doubled Nd:YAG lasers (Continuum) operating at 532 nm. Dichroic optics were used to combine the pulses and beam waists were adjusted by optical telescopes. Three successive optical delay lines stretched each pulse from 10 ns to roughly 83 ns (FWHM) to lower the probability of optical breakdown resulting in a total pulse width (FWHM) of approximately 500 ns. After passing the delay line, a small fraction of the combined beam was reflected onto a monitor to control their spatial coincidence. The alignment of all beams was mostly covered by using eight motor driven mirror mounts, one for each laser, one for each leg of the optical delay line and one for the last mirror before entering the probe volume. The combined laser energy at the probe volume location was up to 1.8 J/pulse and focused by a 500 mm lens to a projected beam width of 300 μm (1/e^2) determined from the Rayleigh image. The one-dimensional probe volume length spanned 6 mm. The single pulse energy was monitored using a thermoelectric joule meter.

CO-LIF A tunable dye laser was pumped by a seeded Nd:YAG laser. The dye laser beam of approximately 587 nm was frequency doubled and then mixed with the Nd:YAG fundamental to reach 230.1 nm for two-photon excitation of the $B^1\Sigma(\nu' = 0) \leftarrow\leftarrow X^1\Sigma(\nu'' = 0)$ band. The resulting pulse energy was up to 1.3 mJ/pulse and fluctuations were monitored on a single shot basis using a photodiode. The UV-beam was focused using a telescope composed of -75 mm and +150 mm lenses, with the second lens located 1.0 m from the probe volume.

The 532-nm Raman/Rayleigh excitation beam and the 230.1-nm UV CO-LIF excitation beam are combined by a dichroic optic which reflected the UV beam and transmitted the 532-nm just colinear into the probe volume.

2.6.2 Detection

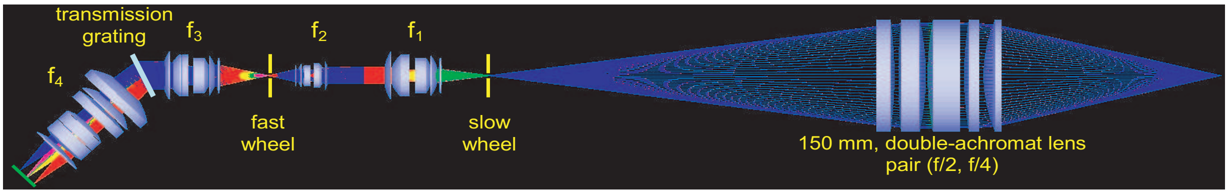

Figure 2.5: Optical detection system for Raman scattering composed of an achromatic collection lens, four commercial camera lenses, two rotating wheel shutters to reject background luminosity, and a transmission grating. Not shown for the sake of clarity: the periscope and a mechanical leaf shutter in front of the slow wheel, a long pass beam splitter after lens f_1, and an optional polarization filter before lens f_2.

Along a 6-mm line segment of the focused laser beam the scattered Rayleigh (532 nm), Raman (550 nm to 700 nm), and CO-LIF (483.5 nm) signals were collected using a custom designed achromatic lens of 150 mm diameter (Linos Photonics, $f/2$, and $f/4$), with a resulting magnification of two as illustrated in Fig. 2.5. The light was reflected by a mirror onto a periscope (not shown in Fig. 2.5, see Fig. 2.4 instead) to rotate the image to align with the vertical entrance slit of the detection unit which was composed of three cameras, six commercial camera lenses, two custom-built, motordriven chopper wheels, and a transmission grating. A gating time of 300 μs (FWHM) was provided by the first wheel (3000 rpm) at the focus of the achromatic lens coinciding with the entrance slit. Additional gating was supported by a mechanical leaf shutter (Melles Griot, 1-inch diameter, ~40 ms gate) to prevent the Raman- and Rayleigh cameras from multiple exposure.

The light was collimated by a camera lens (f_1: 85 mm, $f/1.8$, Nikon). A dichroic beam splitter reflected the signals from Rayleigh scattering (532 nm) and CO-LIF (484 nm) which were then separated by a second dichroic beam splitter (see Fig. 2.4). The transmitted Rayleigh signal was focused by a camera lens (f_5: 85 mm, $f/1.8$, Nikon) through a long-pass filter (center wavelength 532 nm, 10 nm FWHM) onto a back illuminated CCD camera

(1340×400 pixels, Roper Scientific NTE/CCD-1340/400 EMB). The reflected CO-LIF signal was focused by a camera lens (f_6: 50 mm, $f/1.4$, Nikon) through a long-pass filter (center wavelength 484 nm, 10 nm FWHM) onto an intensified CCD camera (512×512 pixels, Andor) where the CO-LIF emission from the $B^1\Sigma(\nu' = 0) \rightarrow A^1\Pi(\nu'' = 1)$ band was detected (∼480-488 nm).

A camera lens (f_2: 50 mm, $f/1.4$, Nikon) was used to focus the Raman signal through the entrance slit of the spectrometer. Optionally, in front of this lens Raman scattering passed a high-transmission thin-film polarizer reducing the crosstalk of depolarized broadband and C_2-fluorescence interferences by up to 50 %. Numerous measurements were repeated with the polarizer turned by 90° to monitor the background and minor contributions from depolarized Raman scattering to allow for further analysis in the post-processing. Background luminosity is further rejected by a fast gating of 3.9 μs (FWHM) of this entrance by the second rotating chopper wheel (21,000 rpm). In the Raman spectrometer the light was then collimated by a camera lens (f_3: 85 mm, $f/1.4$, Nikon) and send onto the transmission grating.

At an incident and refracted angle of 22° the light is dispersed by a custom transmission grating (Kaiser Optical Systems, 1200 lines/mm) with efficiency specifications of up to 90 % at the central wavelength of 625 nm and 0.78 % for 565, and 685 nm. A last camera lens (f_4: 135 mm, $f/2$, Canon) was mounted in front of the Raman CCD detector (1300×1340 pixels, Roper Scientific, VersArray 1300B, with CryoTiger Liquid Nitrogen Cooling Unit operated at -110°C). The two rotating wheels were locked in frequency and phase to a master controller, which also generated trigger signals for the cameras and lasers. Pressure, relative humidity and temperature of the coflow air were monitored by a manometer, hygrometer and thermocouple, respectively. A second thermocouple was used to measure cold gas temperatures in calibration gases.

Data acquisition Raman data were acquired in two modes, one using on-chip binning and the other using full spectral resolution (roughly 3 cm^{-1}/pixel). In both cases, on-chip binning by 10 pixels was used in the spatial direction for a projected resolution of 102 μm across the 6.12 mm probe length, resulting in 60 strips of spectral information. In wavelength direction spectral ranges for both hardware and software binning were selected to define seven Raman detection channels to monitor seven major species. In addition, two spectrally binned regions were similarly defined for monitoring of fluorescence interference and background luminosity around Raman shifts of 930 cm^{-1} and 4300 cm^{-1}, respectively. Rayleigh images were recorded using a 2×2 hardware binning and a resolution of ∼20 μm/pixel. Binning for the CO camera was 5×8, with the former in the laser beam direction and the latter in the vertical direction, resulting in 62 spatial pixels and a resolution of ∼100 μm/pixel. Generally, data files of one hundred shots were taken. Each file contained additional single-shot information on laser energies, relative humidity, pressure, two thermocouple temperatures, and the position of the traversing system for the measurement object.

2.7 Data reduction

Data post-processing was based on three different methods. Two methods have been used in the past to evaluate the data: spectral fitting, based on libraries of theoretical spectra; or matrix inversion of signals that are not spectrally resolved, based on extensive calibration of temperature-dependent system response. In this work a hybrid method for Raman/Rayleigh data analysis was developed that combines the strengths of both previous methods.

In all methods, the processing of Raman scattering signals into concentrations must account for the temperature dependence of Raman spectra and the integrated scattered signals of each measured species. Raman spectra of certain species overlap. For example, there is crosstalk between CO_2 and O_2, between CO and N_2, and from H_2 rotational lines onto all the other species to varying degrees [8, 17, 34, 60, 69, 77]. In addition, there can be interferences from laser induced fluorescence and from broadband flame luminosity [8, 69, 77].

2.7.1 Polynomial Matrix Inversion

In the matrix inversion method (MI) [8, 17, 34, 77] Raman signals, fluorescence interferences, and background radiation are integrated across fixed spectral regions (Raman channels) to form a signal vector $S_{\mathrm{Ram},i}$ (or just: S_i). Spectral information on broadening and shifting of Raman bands with increasing temperature is lost, as are spectral details of interferences. When a CCD is used for detection, Raman channels are defined by on-chip binning, whereas in earlier approaches photomultiplier tubes were placed at fixed spectral positions at the exit plane of a large spectrometer. The signal vector is related to the corresponding vector of unknown species number densities, N_i, through the matrix equation

$$S_i = c_{ij}(T)N_j \tag{2.95}$$

where the matrix elements depend on temperature and the specific experimental setup. As introduced in Section 2.4.2, diagonal elements $c_{ii}(T)$ are the Raman responses of the various species, whereas off-diagonal elements $c_{ij}(T)$ represent crosstalk between Raman channels and from the fluorescence interference and background luminosity channels. In the polynomial matrix inversion the temperature dependence of each matrix element is represented as a polynomial and based on calibration measurements in cold gases, electrically heated gases, and well characterized laminar flames. Number densities in turbulent flames are determined by solving the inverse equation for the vector N_i. The local instantaneous temperature from simultaneously measured Rayleigh scattering is used in evaluating the matrix elements. Because the effective Rayleigh cross section depends on the gas composition, an iterative solution is applied. Consequently, the inverse matrix equation and all non-zero elements c_{ij} considered in this work are expressed by

$$\begin{bmatrix} N_{\mathrm{CO_2}} \\ N_{\mathrm{O_2}} \\ N_{\mathrm{CO}} \\ N_{\mathrm{N_2}} \\ N_{\mathrm{HCs}} \\ N_{\mathrm{H_2O}} \\ N_{\mathrm{H_2}} \\ N_{\text{CO-LIF}} \\ \widetilde{N}_{\mathrm{F560}} \\ \widetilde{N}_{\mathrm{bck}} \end{bmatrix} = \begin{bmatrix} c_{11} & c_{12} & & & c_{15} & c_{16} & c_{17} & & c_{19} & c_{1\,10} \\ c_{21} & c_{22} & & & c_{25} & c_{26} & c_{27} & & c_{29} & c_{2\,10} \\ & & c_{33} & c_{34} & c_{35} & & c_{37} & & c_{39} & c_{3\,10} \\ & & c_{43} & c_{44} & c_{45} & & & & c_{49} & c_{4\,10} \\ & & & & c_{55} & c_{56} & & & c_{59} & c_{5\,10} \\ & & & & & c_{66} & c_{67} & & c_{69} & c_{6\,10} \\ & & & & & c_{76} & c_{77} & & c_{79} & c_{7\,10} \\ c_{81} & & & & & & & c_{88} & & \\ & & & & c_{95} & & c_{97} & & c_{99} & c_{9\,10} \\ & & & & & & & & & c_{10\,10} \end{bmatrix}^{-1} \cdot \begin{bmatrix} S_{\mathrm{CO_2}} \\ S_{\mathrm{O_2}} \\ S_{\mathrm{CO}} \\ S_{\mathrm{N_2}} \\ S_{\mathrm{HCs}} \\ S_{\mathrm{H_2O}} \\ S_{\mathrm{H_2}} \\ S_{\text{CO-LIF}} \\ S_{\mathrm{F560}} \\ S_{\mathrm{bck}} \end{bmatrix} \tag{2.96}$$

Herein, $\widetilde{N}_{\mathrm{F560}}$ and $\widetilde{N}_{\mathrm{bck}}$ do not refer to real number densities which is denoted by the tilde. Crosstalk from background luminosity was treated linear with the measured signal S_{F560}, and all c_{i10} did not possess a temperature dependence, correspondingly. The remaining 35 non-zero elements c_{ij} were represented by temperature dependent polynomials of up to fifth order.

2.7.2 Spectral fitting

The second approach for processing Raman data is the spectral fitting method (SF) [43]. Based on Placzek's theory of polarizability, described in Section 2.3, individual rovibrational Raman transitions are calculated for each species, commonly in the temperature range of 250 K to 2500 K and are convolved with an appropriate apparatus function according to Section 2.4.1.

The spectral library for each molecule is then calibrated to an experimental spectrum measured in a gas sample with known mole fraction and temperature. This accounts for specific experimental conditions (detection and quantum efficiency, etc.). Subsequently, species concentrations in turbulent flames can be computed directly by fitting measured spectra with the calibrated libraries using an advanced routine [43]. Crosstalk is taken into account inherently, and the background is accounted for by fitting it simultaneously with the Raman spectra, using piecewise cubic splines or linear interpolation.

2.7.3 Hybrid matrix inversion

The hybrid method is strongly based on the polynomial matrix inversion method, but with the temperature dependence of fifteen matrix elements c_{ij} determined from integration of the spectral libraries over intervals corresponding to the binned Raman channels according to Eqs. (2.76) and (2.78). Furthermore, an additional dimension is introduced to the matrix Eq. (2.96) to account for differences in the response and crosstalk factors at different spatial positions along the imaged 6-mm line segment. The details of this method are presented in Chapter 3.

2.7.4 Calibration procedure

The temperature is calibrated in particle filtered ambient air using the thermocouple reference. Raman calibration factors $c_{\mathrm{Ram},ij}$ (or $c_{\mathrm{Ram},i}$ and $c_{\mathrm{Ram},i\leftarrow j}$) are determined at well defined conditions of temperature and composition for each nonzero matrix element $c_{ij}(T)$. Accordingly, before solving the matrix Eq. (2.96) each element $c_{ij}(T)$ is calibrated by the entrywise product expressed as

$$c_{ij}^{\mathrm{calibrated}}(T) = c_{\mathrm{Ram},ij} \circ c_{ij}(T)\,. \tag{2.97}$$

O_2 and N_2 and their crosstalks are calibrated in ambient air. CO_2, CO, H_2O, and H_2 and their crosstalks are calibrated in up to nine different laminar flat flames with equivalence ratios of $\phi = 0.8$ to 1.3. Crosstalk of the fuel is generally calibrated in a cold gas mixture with N_2. The fuel itself is either calibrated in this cold gas or on the investigated unburnt fuel/air mixture of the flame. Interference corrections are calibrated in rich laminar jet flames.

2.8 Measurement uncertainties

Precision Statistical noise in Raman measurements was well characterized by Miles [70]. Following the procedure therein, the total noise N_{tot} is expressed as

$$N_{\mathrm{tot}}^2 = n_{\mathrm{e}^-} + N_{\mathrm{detector}}^2 \tag{2.98}$$

where n_{e^-} is the shot-average number of detected photoelectrons per Raman-pixel. Single-shots follow a Poisson distribution and $\sqrt{n_{\mathrm{e}^-}}$ is known as shot noise, correspondingly. N_{detector} is the cumulated noise of the Raman camera for that pixel. In the present setup $N_{\mathrm{detector}} \approx 8\,\mathrm{e}^-$ for the applied binning by 10 pixels in spatial direction (along the imaged laser beam). For hardware-binning in spectral direction the value of N_{detector} does not change with respect to the resulting superpixel – for software-binning (sb) applied on the same pixel range it increases with

$$N_{\mathrm{detector}}^{\mathrm{sb}} = \sqrt{n_{\mathrm{pixel}}} N_{\mathrm{detector}} \tag{2.99}$$

where n_{Pixel} is the number of binned pixels in spectral direction. In present measurements these were in the range of 50 (O_2) to 162 (CH_4) pixels. The overall signal to noise ratio

Table 2.2: Theoretical 5σ laser single-shot detection limit in mole fractions at 300 K and 2000 K, 101.325 kPa, and 1.5 J/pulse.

	X_{CO_2}	X_{O_2}	X_{CO}	X_{N_2}	X_{CH_4}	X_{H_2O}	X_{H_2}
				$T = 300\,\mathrm{K}$			
hardware-binning	0.001	0.002	0.002	0.002	0.0003	0.001	0.001
software-binning	0.006	0.01	0.01	0.013	0.002	0.007	0.007
				$T = 2000\,\mathrm{K}$			
hardware-binning	0.007	0.012	0.01	0.014	0.002	0.006	0.008
software-binning	0.042	0.063	0.058	0.088	0.013	0.045	0.05

(*SNR*) is given by

$$SNR = \frac{n_{e^-}}{\sqrt{n_{e^-} + N_{\mathrm{detector}}^2}} \,. \tag{2.100}$$

To determine the overall detection limit of the system, Eq. (2.100) is written as

$$n_{e^-} = \frac{1}{2}\left((SNR)^2 + \sqrt{(SNR)^4 + 4(SNR)^2 N_{\mathrm{detector}}^2}\right) \,. \tag{2.101}$$

Correspondingly, for each Raman superpixel the signal detection limit at 5σ conditions (SNR=5, $N_{\mathrm{detector}} = 8\,\mathrm{e}^-$) for laser single-shot measurements calculates to $n_{e^-} = 55\,\mathrm{e}^-$. By using measured photon numbers from appropriate experimental data at known conditions and corresponding binning ranges[‡] in Eq. (2.99) the calculated limits were translated into mole fractions and are shown for hardware- and software-binning, at 300 K and 2000 K in Table 2.2. These theoretical values are in good agreement to experimental mole fractions at 5σ-conditions. To analyze precision values for derived quantities like mixture fraction or gradients, error propagation calculations which account for correlated samples must be used, e.g. the python uncertainties package [3]. Then, also excellent agreement with experimentally observed noise in these quantities is obtained. However, for practical purposes it is often more convenient to give experimental precision values at typical flame conditions. These are listed in % in Table 4.1.

Accuracy Accuracy was estimated as outlined in Barlow et al. [12]. Before and after each measurement, data in air and laminar CH_4/air flat flames were taken to account for drift in the overall response of the Raman/Rayleigh scattering and CO-LIF system. The observed drift is typically 1 to 3 % during a day (~6 h) for the Raman/Rayleigh system and

---

[‡] to split large signals and omit saturation, two and three Raman superpixels were used for CO_2 and CH_4 in the hardware-binning case, respectively

approximately up to 10 % in the CO-LIF system. Between two subsequent measurements (<1 h) it is mostly below 1 %. By application of appropriate recalibration based on these measurements in air, the drift can be well compensated and its impact is reduced to <1 %. Inaccuracies due to the calibration or data evaluation process, e.g. temperature of thermocouple, reference values from laminar flame calculations, nonlinearity of the detectors, or uncertainties in response and crosstalk curves were included into conservative values which are listed in Table 4.1 for selected flame conditions. For discussion on uncertainties and sensitivites of particular components see Seffrin [85]. In the following whenever possible, accuracies of particular measurements are discussed with the results explicitely. Special characteristics present in DME/air flames regarding the fuel and temperature measurement or impact of fluorescence interferences on species measurements are thoroughly discussed in Chapter 4.

3 Hybrid approach for data reduction

This chapter presents a hybrid approach for processing Raman data, combining the advantages of both methods, outlined in Section 2.7. In this hybrid approach the temperature dependence of each matrix element for Raman spectral response and crosstalk is determined by integrating the calculated spectral libraries over regions corresponding to on-chip binning. In the following sections the hybrid method is described, calculated and measured spectra and response curves are compared, and the different post-processing methods are evaluated using results from premixed methane-air flat flames and a laminar hydrogen jet diffusion flame. A great part of the results is already published in Fuest et al. [41].

3.1 Experimental setup and hybrid method

The details of the experimental setup for line-imaged multiscalar measurements at Sandia are described in Section 2.6. In all measurements the high-transmission linear polarizer was placed in front of the spectrometer to reduce the relative importance of fluorescence interference and chemiluminescence. Two sets of data were acquired, one with no binning in the spectral direction on the Raman camera and the other with wide regions of on-chip spectral binning corresponding to Raman bands for different molecules.

The Raman spectrometer combines commercial camera lenses with a high efficiency transmission grating to yield significant improvements in spatial resolution and optical throughput over the previously used Czerny-Turner spectrometer [14]. An intrinsic feature of this type of spectrometer is that the image of a straight entrance slit or laser beam is optically distorted or bowed [103]. This is illustrated in Fig. 3.1, which shows the curved image of N_2 Raman scattering from the laser beam in room temperature air. With the present system the location of the peak in the N_2 spectrum shifts by as much as $+10$ pixels, comparing the lower edge of the imaged region to the optical center. A shift of $+10$ pixels is equivalent to a shift of 1.2 nm toward the red, based on dispersion of 5.95 nm/mm at that wavelength. The problem presented by this bowing effect is similar to that caused by beam steering in turbulent flames. In both cases the imaged Raman scattering spectrum shifts relative to fixed binning regions on the CCD. Measurements of N_2 and H_2O are relatively

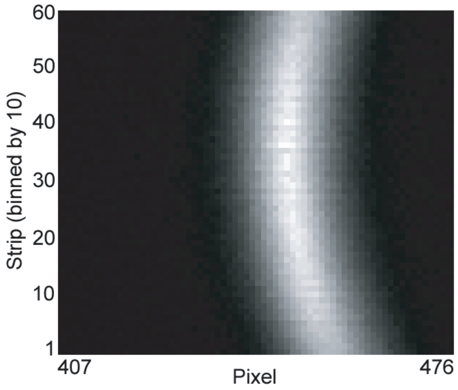

Figure 3.1: Illustration of the bowing effect in the transmission spectrometer showing the N_2 Raman band measured in air at 293 K. Vertical direction displays the spatial coordinate (60 strips corresponding to 6 mm along the laser beam) and horizontal direction the wavelength (pixel) coordinate. Binning by 10 is applied in spatial direction but full resolution for the spectral dimension. The width of the image (pixel range 407-476) corresponds to the on-chip binning region for N_2.

insensitive to these effects because binning regions are wide enough to include nearly the entire Raman spectrum at temperatures of interest. However, other species results can be quite sensitive, as will be shown. It would be impractical to account for bowing or beam steering using calibration based polynomials because extensive calibrations would have to be repeated for many different positions of the laser beam. However, both effects can be addressed in a straightforward manner by the hybrid method.

Figure 3.2 shows relative Raman scattering spectral signal intensities calculated for CO_2, O_2, CO, N_2, H_2O and H_2 using an extended version of RAMSES presented in the thesis of Geyer [43] and the diploma thesis of Fuest [39]. CH_4 is excluded from these calculations because reliable quantum mechanical models for CH_4 covering the whole temperature range are not available. However, in this work results for CH_4 from quantum mechanical calculations based on an updated version of the software package STDS [101] were as well implemented into the RAMSES code and the current status is discussed in Section 3.3.5. For each chemical species the perpendicular polarization direction of the Raman bands are calculated for temperatures ranging from 250 to 2500 K according to Eq. (2.70). Calculated spectral libraries account for the measured nonlinear dispersion of the spectrometer according to Eq. (2.73) ranging from 6 nm/mm at small pixel numbers to 5.4 nm/mm at high pixel numbers. The temperature dependence of the spectrum of each molecule and the overlap of spectra from different molecules are clearly illustrated in Fig. 3.2. Dashed vertical lines indicate the pixel boundaries for on-chip binning regions (Raman channels) used in the present experiments. In order to demonstrate that the quantum mechanical models reproduces experimental spectra reliably, it was essential to determine the apparatus function of the setup.

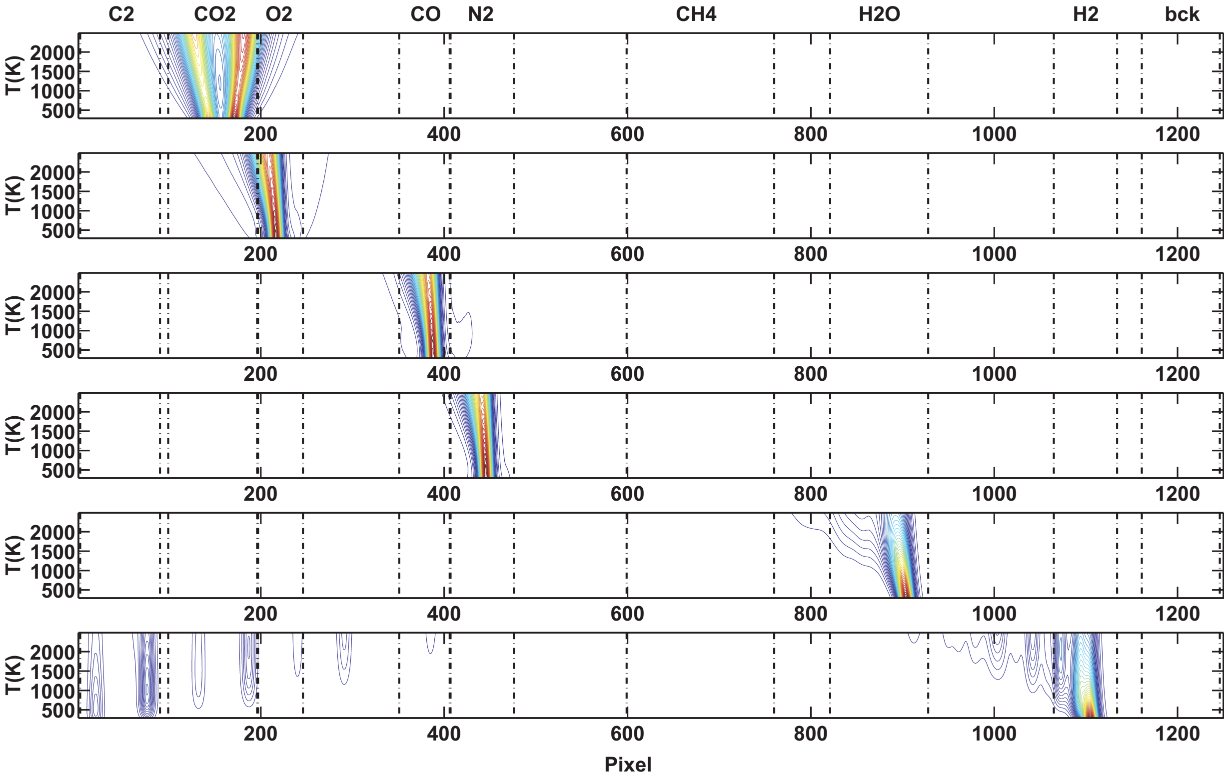

Figure 3.2: Calculated temperature dependence of relative Raman scattering spectral signal intensities from CO_2, O_2, CO, N_2, H_2O, and H_2. Dashed vertical lines indicate the pixel boundaries for on-chip binning regions (Raman channels) used in the present experiments.

3.2 Apparatus function

In general, it is rather elaborate to obtain a perfect apparatus function valid for the whole Raman image due to variations in wavenumber and spatial Raman-pixel space. Also, the function varies temporally due to changes of the beam profile in the focus, e.g. when the delay lines are subject to small thermal drifts or are being readjusted. However, these sensitivities were more important for data evaluation using the spectral fitting method and mostly negligible in case of the matrix inversion method. This was mainly due to the fact that convergence of the spectral fitting could be highly influenced by significant differences in spectral shape. Whereas convergence in the matrix inversion method is completely independent of the spectral shape and, in addition, differences in spectral shape due to variations in the apparatus function are mostly eliminated by proper calibration before the data evaluation.

For the experimental setup used in this work, the apparatus function is strongly dominated by the beam profile of the laser. Hence, the first choice for an apparatus function was the

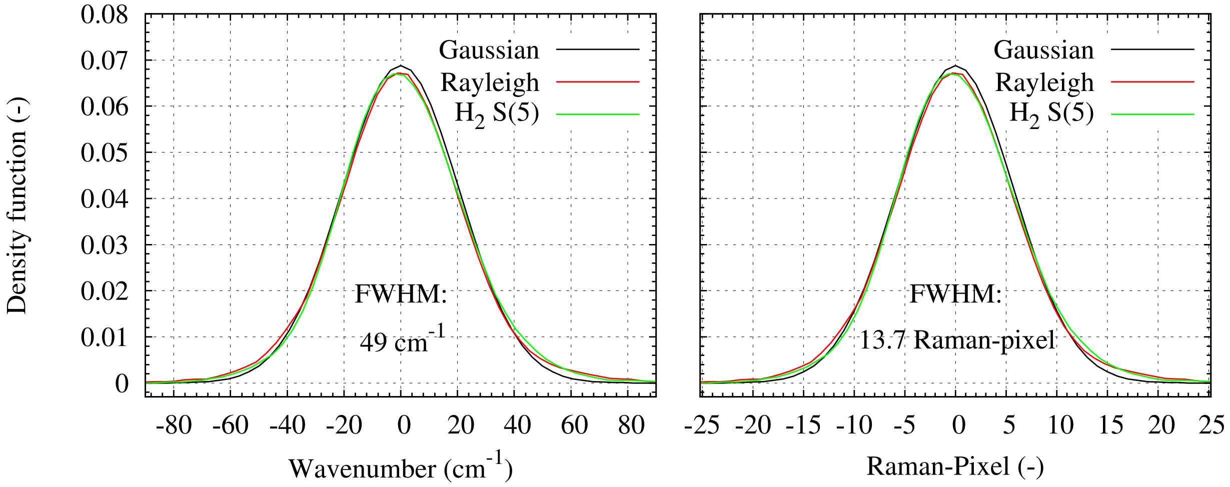

Figure 3.3: Experimental apparatus functions Γ_{app} in comparison with Gaussian function in wavenumber- and Raman-pixel space corresponding to a dispersion of $3.57\,\mathrm{cm}^{-1}$/pixel. A single-transition signal from one hundred detected photons would be stretched over approximately 40 pixels on the Raman camera with a resulting maximum of seven. Peaks which are separated by more than $50\,\mathrm{cm}^{-1}$ can be well distinguished. Just one peak is observable for separations smaller than $40\,\mathrm{cm}^{-1}$.

Rayleigh scattering image of the laser beam in air or cold gases, appropriately scaled in FWHM for the corresponding spectral and spatial positions on the Raman image.

In a second step, the pure rotational line $S_0(5)$ of hydrogen at 900 K in the laminar hydrogen diffusion jet was identified as the best resolved single transition line with a small bias from other transitions or transmission gradients and a spectral position ($1447.3\,\mathrm{cm}^{-1}$) close to CO_2 and O_2 providing reasonable comparability when used for convolution. A one hundred shot-average was taken, a small part from $S_1(5)$ was appropriately subtracted, and remaining noise was filtered using the Savitzky-Golay algorithm [83] with polynomial second order and frame size eleven. A difference in transmittance of ±4.5 % was determined for the region spanning ±20 pixels around the hydrogen peak from relative signals of hydrogen rotational lines. However, this difference is small, and no impact on convolved spectra was observed between a transmission corrected apparatus function and the uncorrected version. In the spectral fitting procedure, correction for spectral transmission effects are important for the lines of H_2 as these extend to the whole spectral range. A small effect due to transmission gradients is noted for CO_2.

To focus first on the curve shapes, all profiles were matched to the FWHM of the hydrogen line and were normalized to one. Figure 3.3 shows one Rayleigh profile from air and the hydrogen profile in comparison with a Gaussian normal distribution. The Rayleigh profile and the H_2 S(5) profile are very similar in shape and differences of this order do clearly not affect the matrix inversion method. However, by spectral fitting of calculated and convolved spectra against experimental data smaller residua were accomplished with the hydrogen profile used as convolution function. But most probably this can not be generalized as appearing differences are already close to uncertainties due to the $S_1(5)$ subtraction, the smoothing filter applied on the hydrogen line, and the differences due to the pixel discretization in the experiment. Compared to the Gaussian in Fig. 3.3, both the Rayleigh and the hydrogen profile are skewed to the left and are slightly wider at the bottom. However, as well these differences were not found to impact the generation of response curves for the matrix inversion method significantly, and the Gaussian function was also quite useful to investigate sensitivities of variations in FWHM. Common variations in FWHM were determined from various data sets taken at different days. Maximum differences in FWHM of ±25 % were found between Rayleigh images from one day. A maximum variation of ±10 % of the nitrogen Raman band was observed along the 6-mm spatial direction, respectively.

3.3 Raman spectra simulation

To demonstrate that the quantum mechanical model reproduces experimental spectra reliably, all species were calculated and convolved with the H_2 S(5) line. In addition, H_2 and CO_2 were corrected for transmission gradients. Finally, all calculated spectra were compared to experimental spectra from an average of one hundred single-shots. The agreement is very good. Hence, residua are shown below using a zoom factor of four. All CCD counts were translated into photon count numbers with the corresponding gain factor of the Raman camera ($2.6\,\mathrm{e}^-$/Count). If available, both polarization directions are shown for most of the species from experiment and simulation. In the calculation 5 % of the perpendicular component was added to all parallel polarized spectra to correct for a part of trace scattering present in the parallel polarized component.

3.3.1 CO_2

The simulation of CO_2 was presented in Geyer [43]. Geyer showed that a large increase in numbers of weak single transitions in higher polyades impacts the temperature dependence of the integrated Raman signal significantly and needs to be taken into account for correct prediction of CO_2 Raman signals spanning a large temperature range. Consequently, polyades up to $P = 30$ were included into the spectra simulation. Rotational transitions of O-, P-, Q-, R-, and S-branches and rotational quantum numbers up to $J^i = 200$ are considered. However, with the present resolution, just two rovibrational peaks of the Fermi doublet $\nu_1 + 2\nu_2$ are observable. First, with respect to the O_2 border, agreement is very good. Accordingly, the crosstalk on O_2 should be predicted reliably. Second, a small discrepancy is observed at the blue end (low pixel number). However, this shoulder is just slightly affecting the C_2 fluorescence correction channel and completely negligible compared to significant C_2 fluorescence count numbers. Third, a systematic difference for both temperatures is observed in relative heights between the ν_1 and $2\nu_2$ peaks. This is currently investigated by Geyer [44]. A significant impact on the response curves is not expected.

3.3.2 O_2

Details on the present simulation of O_2 are as well presented in Geyer [43]. The triplet structure of the electronic ground state, vibration-rotation interactions, and contributions from excited electronic states are taken into account. The agreement in spectral shapes between experiment and calculation shown in Fig. 3.5 is excellent and needs no further discussion.

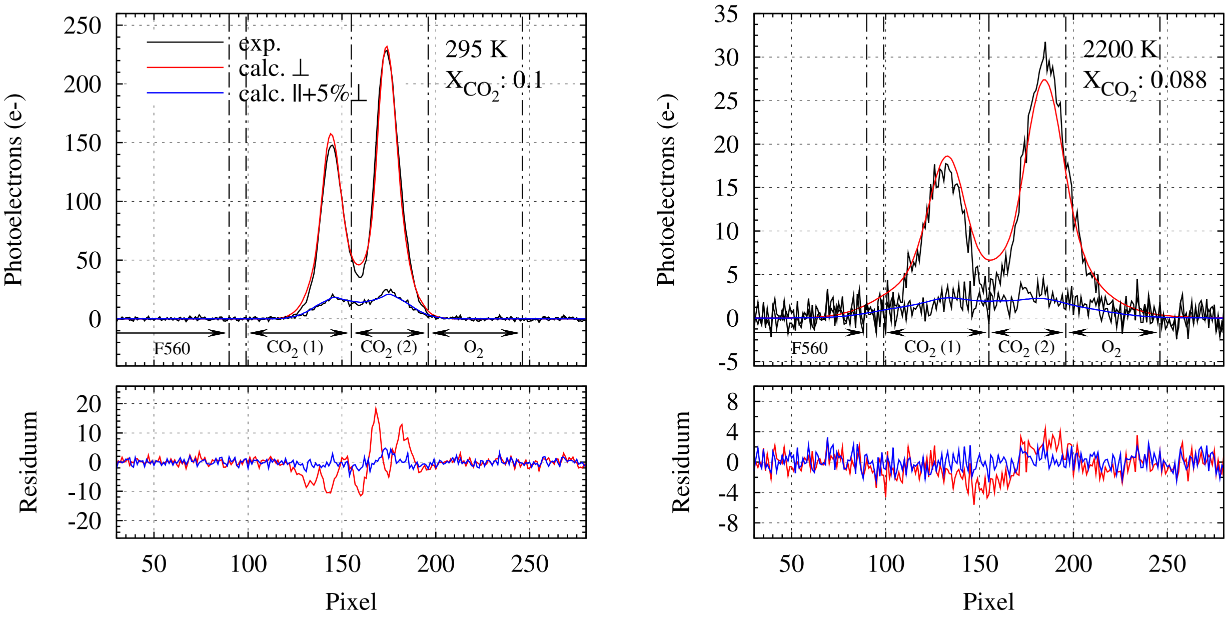

Figure 3.4: Parallel and perpendicular polarized Raman spectra of CO_2 cold gas diluted with 90 % nitrogen, and spectra in post-flame region of a stoichiometric laminar CH_4/air flat flame. The residuum after subtraction is shown. Dashed vertical lines mark the binning region.

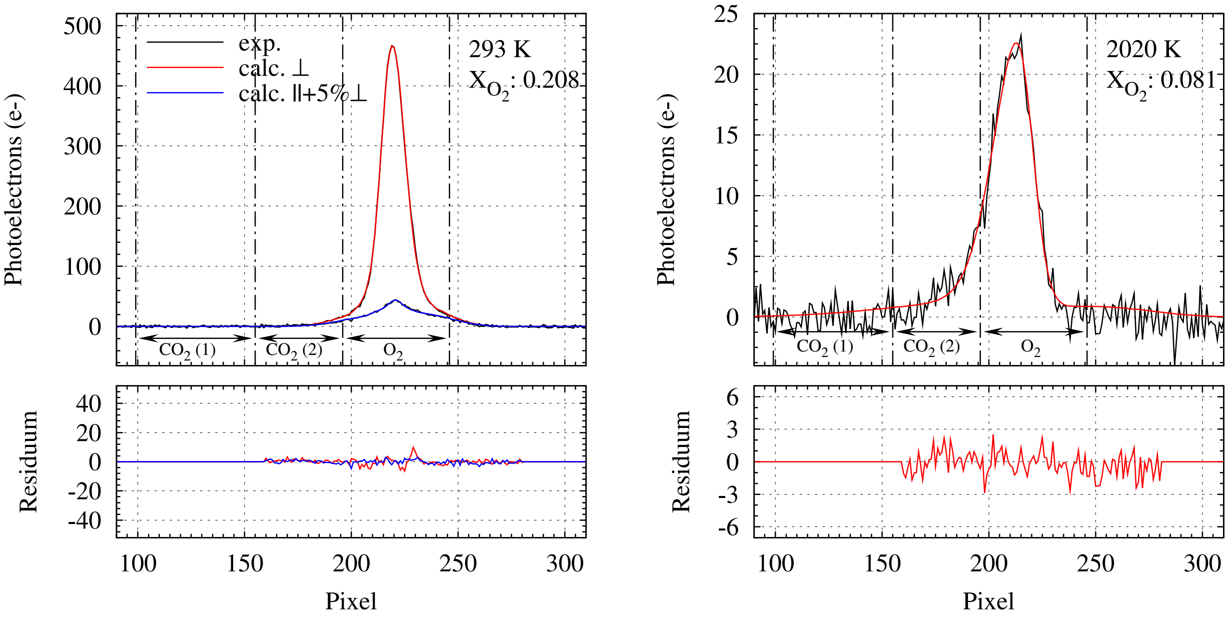

Figure 3.5: Left: Perpendicular and parallel polarized Raman spectra of O_2 in air comparing simulation and experiment. Right: Polarized Raman spectrum of O_2 in the laminar hydrogen jet flame at 2020 K - the parallel polarized part was not taken in that flame. Dashed vertical lines mark the binning region

3.3.3 CO

Again, the simulation of CO is presented in Geyer [45]. Vibration-rotation interactions are taken into account to improve the high-temperature predictability following the perturbation approach of Buldakov et al. [26]. Vibrational quantum numbers up to $v = 5$ and rotational quantum numbers of up to $J = 100$ and O-, Q, and S-branches are considered. For the comparison with the calculated spectra of CO, the most intense and less distorted CO-signal was identified in a laminar DME/air (11.4 % DME) jet flame at 1930 K. The spectral fitting was limited to the range with small impact of the crosstalk from nitrogen. The agreement in shape is perfect, as shown in Fig. 3.6.

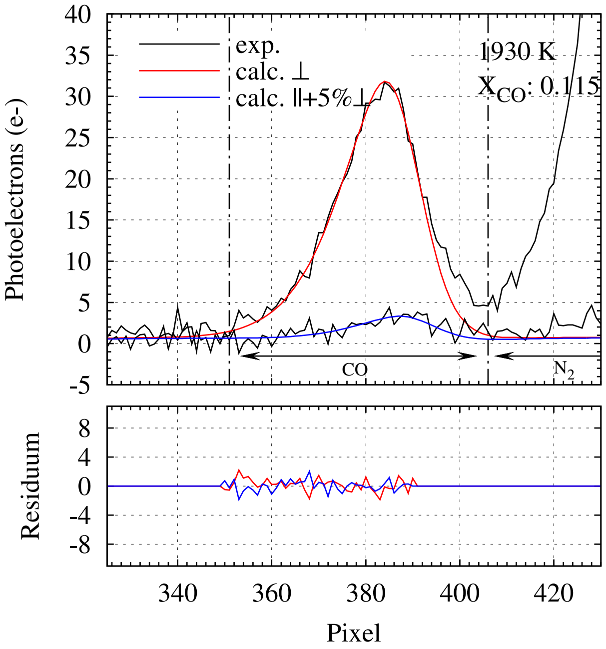

Figure 3.6: Perpendicular and parallel polarized Raman spectra of CO in a laminar DME/air jet (11.4 % DME) at 1930 K. Dashed vertical lines mark the binning regions. The right shoulder is affected by crosstalk from N_2.

3.3.4 H_2 and N_2

Both, H_2 and N_2 spectra are based on *ab initio* calculations presented in the diploma thesis [39]. Within the Born-Oppenheimer approximation pointwise functions for dynamic polarizabilities in Eqs. (2.37) and (2.38) were calculated at appropriate internuclear distances R for 532 nm excitation wavelength using the molecular electronic structure program DALTON [1]. Then, the one-dimensional Schrödinger equation

$$\left(-\frac{\hbar^2}{\mu}\frac{d^2}{dR^2}+\frac{\hbar^2 J(J+1)}{\mu R^2}+V(R)\right)\phi_{\mathrm{vib}}(R,v,J)=E_{v,J}\,\phi_{\mathrm{vib}}(R,v,J) \tag{3.1}$$

was solved using the computer program LEVEL [62] to obtain the accurate rovibrational wavefunctions $\phi_{\mathrm{vib}}(R,v,J)$ and eigenenergies $E_{v,J}$. In Equation (3.1), μ is the reduced mass of the molecule, $V(R)$ is the potential energy curve of the molecule, J is the rotational quantum number, and $\hbar$ is the reduced Planck constant. Finally, the matrix elements of polarizability required in Eqs. (2.39) and (2.40) are obtained from

$$\langle\phi^f_{\mathrm{vib}}|\ \overline{\alpha}\ |\phi^i_{\mathrm{vib}}\rangle=\int_0^\infty \phi_{\mathrm{vib}}(R,v^f,J^f)\,\overline{\alpha}(R)\phi_{\mathrm{vib}}(R,v^i,J^i)\,\mathrm{d}R\,, \tag{3.2}$$

$$\langle\phi^f_{\mathrm{vib}}|\,\Delta\alpha\,|\phi^i_{\mathrm{vib}}\rangle=\int_0^\infty \phi_{\mathrm{vib}}(R,v^f,J^f)\,\Delta\alpha(R)\phi_{\mathrm{vib}}(R,v^i,J^i)\,\mathrm{d}R\,. \tag{3.3}$$

Comparison with experimental spectra is shown in Figs. 3.7 and 3.8. Agreement is almost perfect, i.e. the observed residua for both molecules are well within the order of expected accuracies with the used apparatus function and the polynomial dispersion function in Eq. (2.73). Generally, a higher sensitivity to small changes in the apparatus function is found for cold gas spectra. An increasing deviation at lower pixel numbers is observed for H_2 at 2057 K. This indicates an imperfect correction for transmission gradients in the rovibrational band. This was also indicated by application of the hybrid matrix inversion method in the hydrogen jet flame with the lower binning border shifted to pixel 1032. However, H_2 results in different flames are consistent using the present binning region as shown in Fig. 3.7.

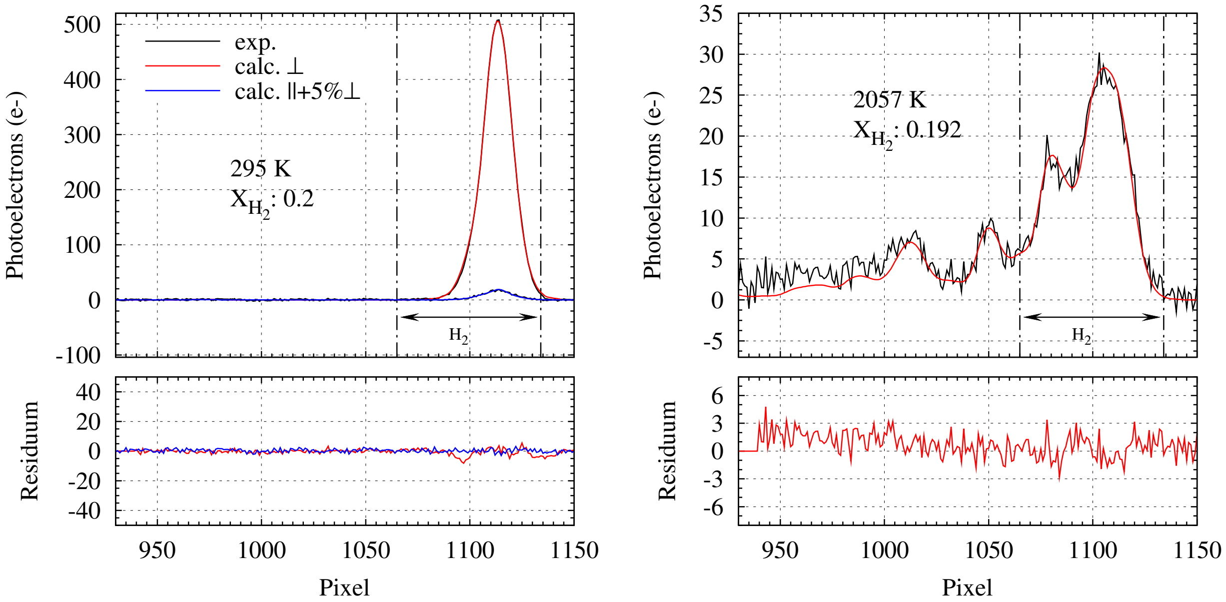

Figure 3.7: H_2 diluted with 80 % N_2 at 295 K for both polarization directions and the perpendicular polarized spectrum of H_2 in the laminar H_2 jet flame at 2057 K. Dashed vertical lines mark the binning region.

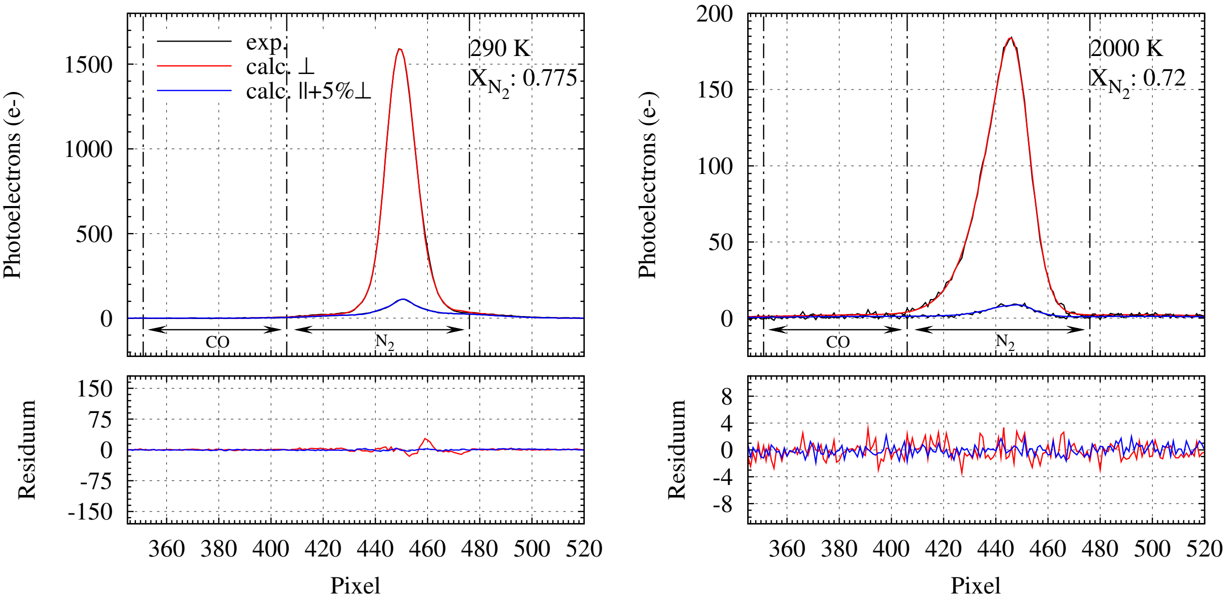

Figure 3.8: Rovibrational Raman spectra for N_2 in air and at 2000 K in post-flame region of a lean CH_4/air flat flame. The measured spectra (black) are averaged using 100 shots. Dashed vertical lines mark the binning region.

3.3.5 CH_4

Stick spectra for CH_4 were calculated using the Spherical Top Data System (STDS) software package [101]. Different polyades are considered (decade, pentade, and octade) resulting in half a million transitions. More information on the theory can be found in Champion et al. [28]. STDS does not allow for polarization dependent output. Thus, in the current implementation in RAMSES no polarization separation for CH_4 is possible. The spectral library of methane was used for the Raman data evaluation by spectral fitting in Gregor et al. [46], but was not used within the hybrid method here. The experimental CH_4 spectra without polarization filter were taken three months later than the other spectra presented in this section. However, the curves shown in Fig. 3.9 are based on the same apparatus function as used for the other molecules. The agreement for cold methane is good and slightly worse for the curves at 820 K. Probably, some improvement on the shape could be achieved with an apparatus function from that day. This was not considered further.

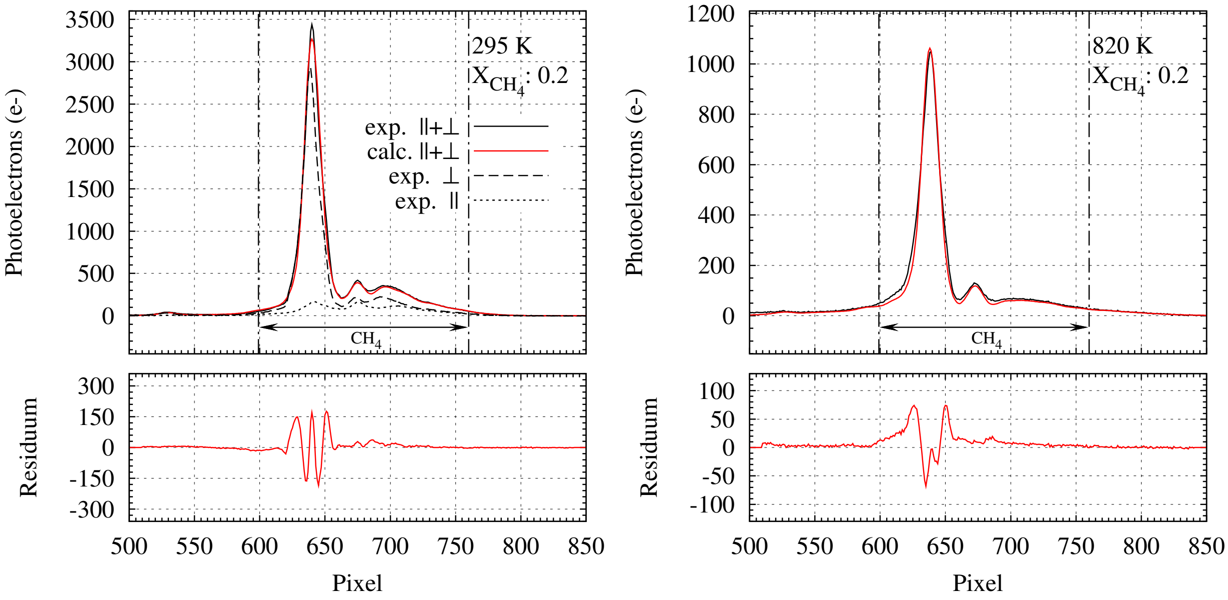

Figure 3.9: Calculated Raman spectra of CH_4 including both polarization directions obtained from Spherical Top Data System (STDS) software package [101]. Experimental data were taken diluted with 80 % N_2 in cold gas at 295 K and electrically heated gas at 820 K. Left part of the figure also shows perpendicular and parallel polarized components from experiment.

3.3.6 H_2O

Depended on temperature up to twenty six thousand transitions are included into the simulation of H_2O implemented by Geyer into the current RAMSES version. Calculations are based on the work of Avila et al. [6], Vidler and Tennyson [98], and others. Currently, just the isotropic part is included in RAMSES. Consequently, no polarization separation is possible in the simulation. The missing part in the perpendicular polarized spectrum can be quantified from the depolarization ratio by $\frac{4\rho}{3-4\rho}$ and for the spectrum composed of both polarization components by $\frac{7\rho}{3-4\rho}$. Experimental depolarization ratios are 0.0342 ±0.0005 for the ν_1 band of water according to Murphy [74, 75], yielding 4.8 % and 8.4 %, respectively. Figure 3.10 shows the perpendicular polarized Raman spectra of water in air at 290 K. The experimental spectra of both polarization directions is shown at 2000 K in the post-flame region of a lean CH_4/air flat flame. Agreement in air is perfect. The agreement of the hot spectra from simulation and experiment is also very good for the main peak, but slightly underestimated for the bands toward smaller pixel numbers. From comparison of the missing area in the calculated spectrum with the parallel polarized part from experiment it is concluded that this is only partly caused by the missing anisotropic part in the simulation because the parallel component is too small, especially around pixel numbers of 820. Other reasons might be an uncorrected transmission gradient or Raman scattering from OH ($X_{\mathrm{OH}} \approx 0.004$), see also Section 4.3.2.2. Accordingly, a small impact of a few percent on the Raman response curves of water is possible.

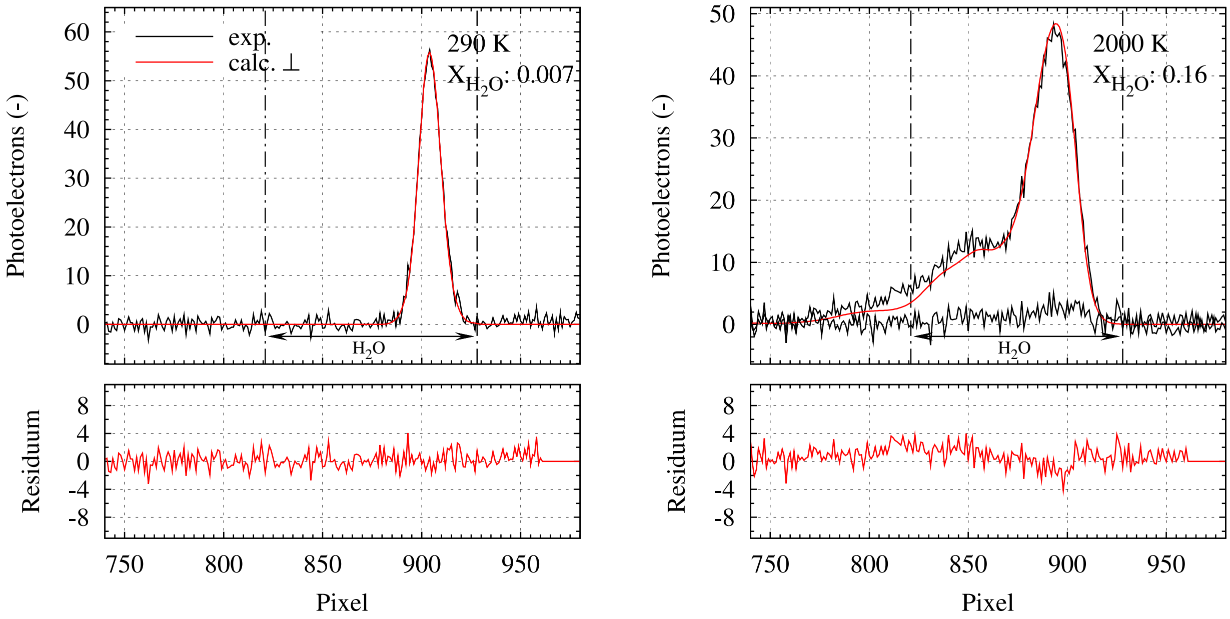

Figure 3.10: Rovibrational Raman spectra for H_2O in particle filtered ambient air and at 2000 K in post-flame region of a lean CH_4/air flat flame. Dashed vertical lines mark the binning region.

3.4 Hybdrid MI

The key to the hybrid method is to use these calculated spectral libraries rather than extensive calibrations to determine the temperature dependence of matrix elements in the MI method. This is done by integrating each calculated spectrum over the pixel regions of on-chip binning according to Eqs. (2.76) and (2.78) with $br_{\text{start}}(i)$ and $br_{\text{end}}(i)$ as indicated in Fig. 3.2. For example, the term for crosstalk from CO_2 onto the O_2 channel is determined by integrating the calculated CO_2 Raman spectrum at each library temperature over the pixel range of the O_2 channel. Furthermore, to allow for automatic compensation for the optical bowing effect and for beam steering in turbulent flames, the integration is performed multiple times with the pixel boundaries being shifted progressively relative to the calculated spectra. Results are stored in tabular form and normalized by the integrated signal intensity at 290 K and zero pixel shift. The calibration factor for each matrix element is determined from one or a few measurements at well defined conditions of temperature and composition. During the iterative solution of the inverse matrix problem, the table of integrated relative signal intensities is interpolated in two dimensions, based on the local temperature and pixel shift. For the present implementation, table entries are spaced by 20 K in temperature and by 1 in pixel shift. Pixel shift due to the bowing effect is represented by a second order fit, and pixel shift of the overall beam due to alignment drift or beam steering is determined from the Rayleigh scattering image of the laser beam profile on each shot. Matrix elements that are not calculated theoretically, such as CH_4 and its crosstalk onto O_2, are currently evaluated using calibrated polynomials from the original MI method.

This procedure can be extended to include interferences from C_2 LIF and hydrocarbons by generating experimentally based spectral libraries and integrating those over the pixel ranges of the binned Raman channels. This is presented in Chapter 4.

3.5 Results and discussion

For the main species appearing in hydrocarbon-air flames, CO_2, O_2, CO, N_2, H_2O and H_2, Fig. 3.11a shows a comparison of temperature-dependent response curves obtained from calibration measurements and from integration of calculated Raman spectra as described in the previous section. The calibration-based curves are also normalized by their values at 290 K. Note that the scales of the individual response curves vary significantly among species. Whereas CO_2 shows strong temperature dependence, the response for H_2O barely changes with temperature and the observed discrepancy is not significant. The sensitivity of the response curves to spectral shift of the Raman channels (binning region) is illustrated by including curves for shifts of ±5 pixels, which is representative of the shift caused by the bowing effect or strong beam steering in turbulent flames.

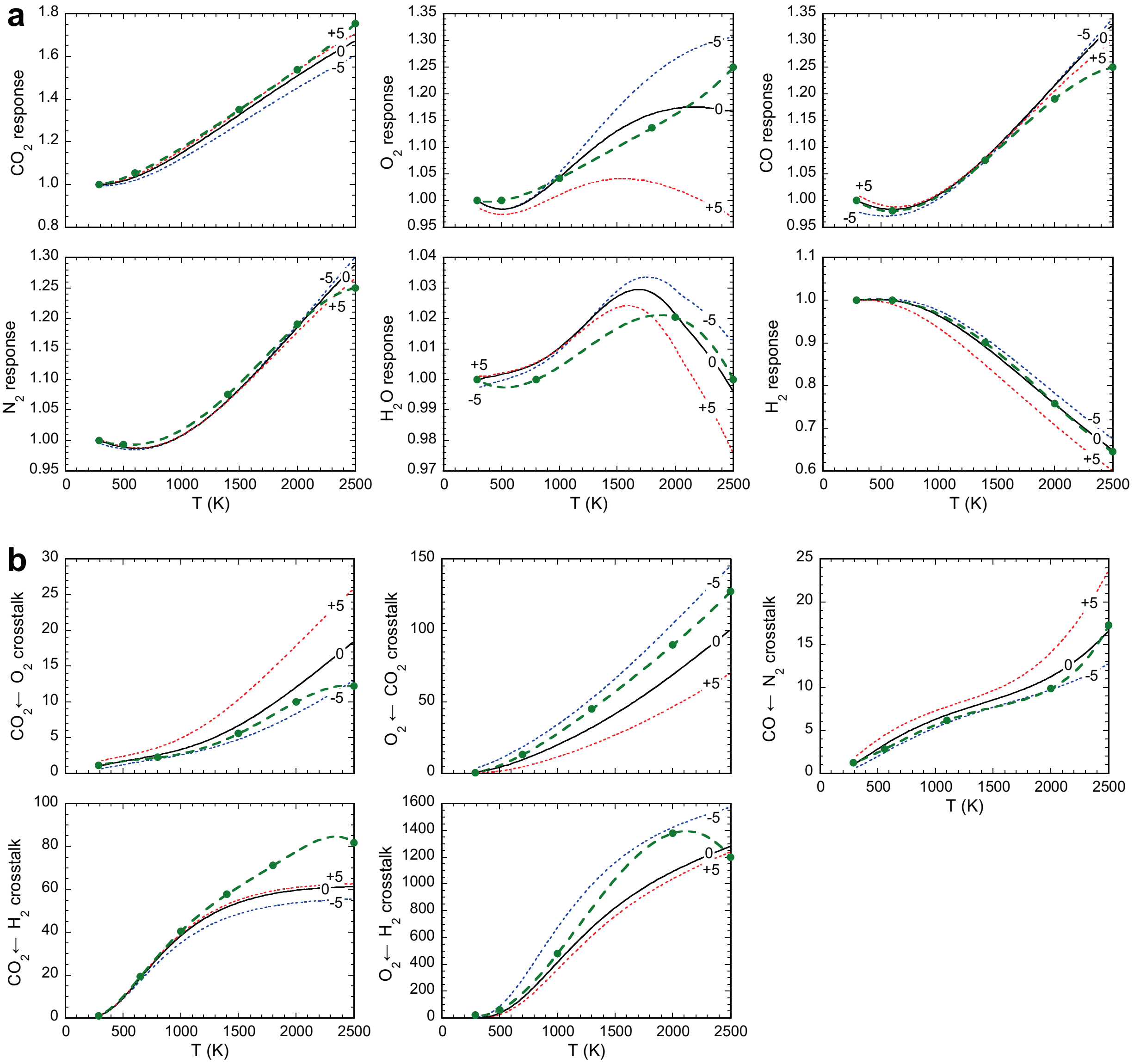

Figure 3.11: Comparison of: a) temperature dependent Raman response curves for CO_2, O_2, CO, N_2, H_2O, and H_2 and b) Raman crosstalk terms based on calibration polynomials (symbols show the tabulated fitting points) and integration of the calculated Raman spectra. The calculated curves are labeled 0, +5, and -5, corresponding to pixel shifts of the integration range.

The calculated response curves of CO_2, CO, N_2, H_2O, and H_2 are considered as the benchmark for the measured ones. Agreement between measured and calculated curves is very good for most of the temperature range. Trajectories of the response curves at rising temperatures are determined by competition between the increasing number of scattered photons and loss of signal as the spectrum of interest extends beyond the boundaries of the corresponding Raman channel due to the larger fractional population of the higher energy levels. Inspecting CO_2 signal intensity in Fig. 3.2, for temperatures exceeding approximately 800 K the Raman channel does not capture the whole Fermi-coupled $\nu_1 + 2\nu_2$ Raman bands but is still increasing because most of the transitions are within the binned region. In contrast, H_2 shows a decreasing response curve. Due to its large rotational constant the spacing between rovibrational Raman lines is much wider than for the other molecules. Consequently, due to the shift of the fractional population at higher temperatures, a smaller fraction of the overall increasing number of scattered photons is captured on the pre-defined H_2 Raman channel. For N_2 an excellent match between experimental and calculated response curves is observed, except at very high temperatures. Similar behavior is observed for CO. For O_2 there is a mismatch between shapes of experimental and calculated response curves at high temperature. Uncertainty in calibration increases at flame temperatures, especially for reactive species, because concentrations are low and luminosity can contribute significantly to the measured signal.

The results for the more important off-diagonal elements accounting for Raman crosstalk, see Eq. (2.78), are presented in Fig. 3.11b. Note that the scale on each plot indicates relative change over the temperature range rather than absolute magnitude because the curves are normalized to unity at 290 K. The most important crosstalk term in hydrocarbon flames is $O_2 \leftarrow CO_2$ because of significant spectral overlap (Figs. 3.2 and 3.4) and low O_2 concentration at high temperature. Although the overall trends between measured and calculated response curves coincide, a high sensitivity to pixel shift is observed. The response curve for O_2 in Fig. 3.11a is also sensitive to pixel shift. Sensitivity of these terms demonstrates the need to account for optical bowing. Equally important is an accurate calibration of wavelength vs. camera pixel, which was accomplished here using a target array of 50-micron holes back-illuminated by a Ne lamp. Whereas the crosstalk term $CO \leftarrow N_2$ can be accurately calibrated using lean H_2-air flames, uncertainty in the experimentally derived curve for the other crosstalk terms can be large. This gives significant advantage to the hybrid approach. Figure 5 illustrates the effect of bowing on Raman crosstalk by comparing spatial profiles of the mole fraction of O_2 measured in products over a fuel-rich premixed laminar flat flame, where the actual mole fraction is practically zero. For these spatially homogeneous conditions, the conventional MI method yields an inhomogeneous O_2 profile that is accurate only near the bowing center (-1 mm), where calibrations are tuned. Homogeneity of the results is significantly improved by application of the hybrid method to the same raw data file. Standard deviations, indicated by error bars in Fig. 3.12, are the same for the two methods.

3.5.1 Comparison of polynomial MI / Hybdrid MI / Spectral fitting

Scatter plots of single-shot results for T, O_2, and CO_2 obtained using four different processing approaches are compared in Fig. 3.13. Measurements are from products above a premixed laminar CH_4-air flat flame operated at five different equivalence ratios from lean

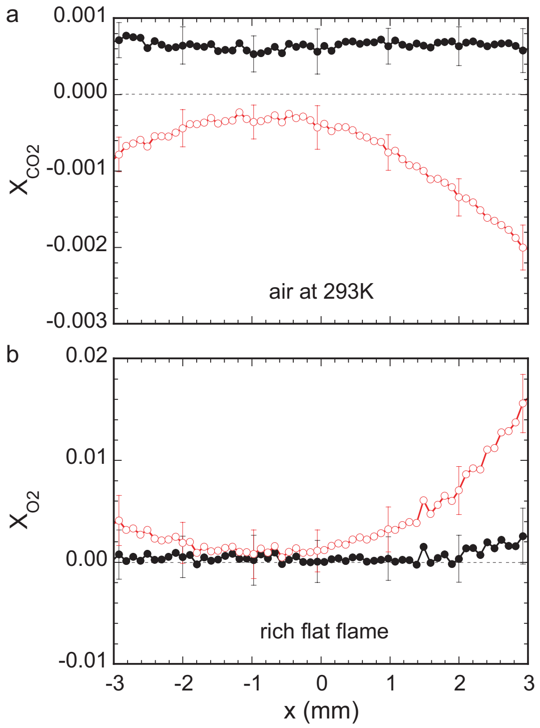

Figure 3.12: Illustration of the effect of optical bowing on crosstalk from (a) O_2 onto the CO_2 Raman channel in air and (b) CO_2 onto the O_2 Raman channel in flat flame products at $\phi = 1.16$. Error bars indicate standard deviation in the polynomial MI method (open symbols) and the hybrid method (closed symbols).

to rich. Data were acquired sequentially in two sets, one with no binning in the spectral direction and the other with on-chip binning as illustrated in Fig. 3.2. Only three equivalence ratios are shown for the cases with no binning to provide better separation. The four data evaluation methods were: MI using calibrated polynomials, hybrid MI, software binning of the spectrally resolved data followed by hybrid MI, and spectral fitting. Several observations can be made. First, with the present detection system, on-chip binning yields significant better precision at flame conditions. This is because the binned signals are limited primarily by photon shot noise and the relative contribution of camera readout noise is suppressed. Second, the effects of bowing are apparent in the polynomial MI scatter data, which show extended tails resulting from CO_2 crosstalk onto the O_2 channel. This crosstalk correlates directly with error in measured equivalence ratio. Temperature is also affected through a change in the apparent Rayleigh cross section. Specifically, bowing at the edges of the image moves CO_2 signal onto the O_2 channel, reducing the calculated Rayleigh cross section, so the same Rayleigh signal yields higher apparent total number density and lower temperature. These effects are corrected in the hybrid MI processing. Negative concentration results are prevented in the SF. Other differences between software binned MI and SF are small and probably caused by distinct calibration methods and

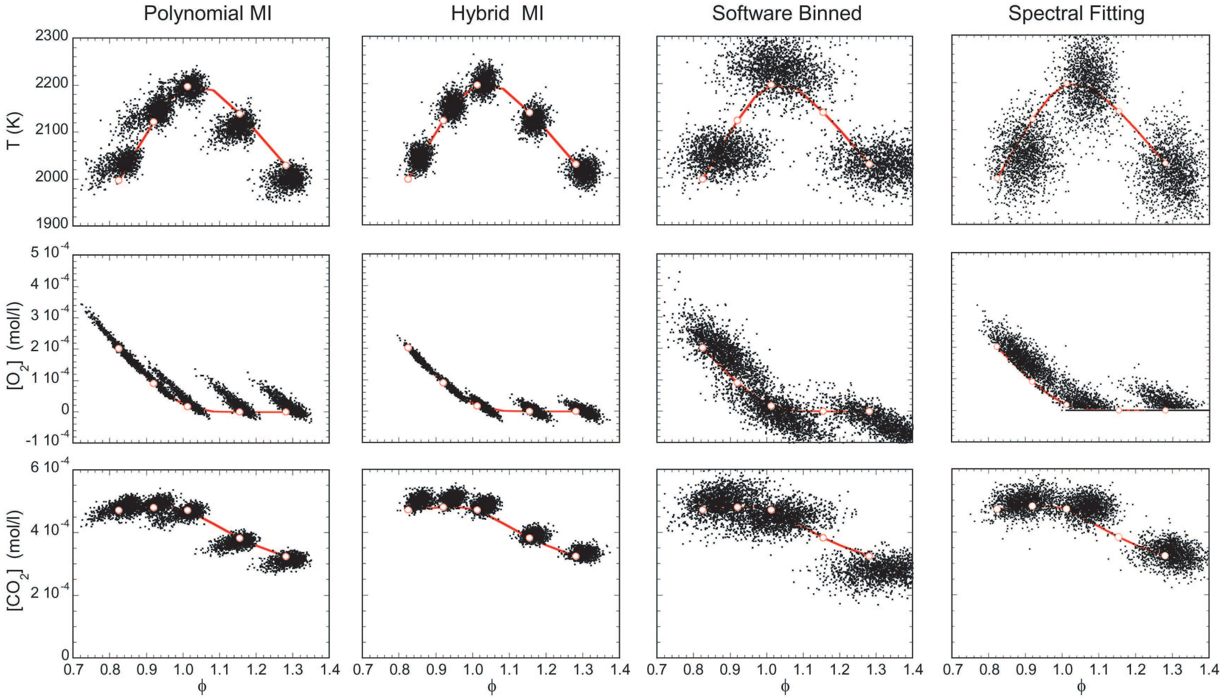

Figure 3.13: Scatter plots of temperature and the concentrations of O_2 and CO_2 measured above a series of premixed CH_4/air flat flames and processed using the indicated methods: matrix inversion with polynomials, the hybrid method, the hybrid method applied to software-binned Raman data, and spectral fitting. Curves through open circles show equilibrium values at 35 K below the adiabatic equilibrium temperature and are taken from laminar flamelet calculations.

background treatment.

Finally, the four data evaluation schemes are compared using measurements from a laminar H_2 jet flame. Figure 3.10 shows radial profiles of mean and rms mole fractions of N_2, O_2, and H_2O taken at an axial height of 30 mm. Profiles were acquired using 3-mm steps of the 6-mm probe, such that each radial location was measured by two different strips on the Raman CCD. Processed results were then averaged. The bowing effect causes discontinuities in mean and rms O_2 profiles from the polynomial MI method, and the software binned results for O_2 show a small offset due to an uncorrected drift in the readout offset of the CCD array, which is negligible for the hardware binned data. Otherwise, mean profiles are in good agreement. Greater differences among processing methods are seen in the rms profiles, where on-chip binning shows advantage across parts of the flame. For the same spectrally resolved data, the spectral fitting method yields lower rms values, especially for O_2, than software binning combined with the hybrid MI method. This shows that the fitting process can serve as a noise filter and, at least, does not add noise to the results. It is also clear that software binning can be applied to achieve rapid initial processing of spectrally resolved data.

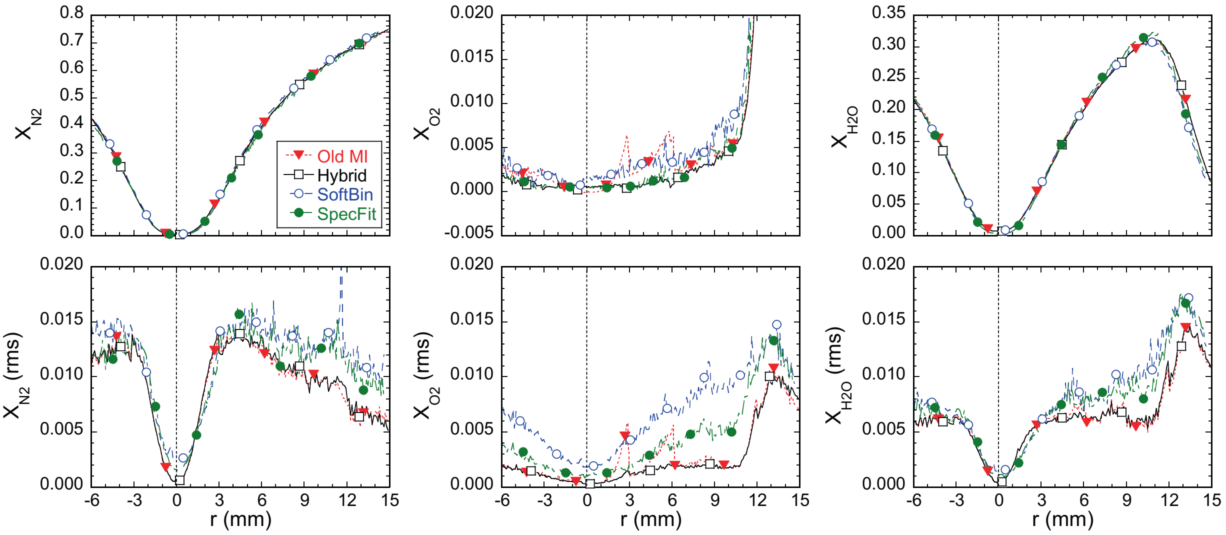

Figure 3.14: Radial profiles of Favre mean and rms species mole fractions based on the polynomial matrix inversion method (Old MI), bin-on-chip hybrid method, software binned hybrid method, and spectral fitting method of data analysis.

3.6 Conclusions

A method of analyzing 1D Raman/Rayleigh scattering data from flames has been developed, which combines advantages of two methods used by the contributing institutions: 1) fitting of spectrally-resolved, single-shot data with libraries of theoretically calculated Raman scattering spectra; and 2) iterative solution of a matrix equation for integrated Raman signals (binned on the CCD detector), using polynomials to represent the calibrated temperature dependence of matrix terms. In the resulting method the temperature dependence of matrix terms was determined by integrating calculated Raman spectral libraries over intervals corresponding to regions of on-chip binning. This hybrid matrix inversion approach retains the benefits of on-chip binning, including suppression of camera readout noise, faster data acquisition, smaller raw data volume, and faster processing. Use of the theoretical Raman spectral libraries eliminates the need for extensive calibrations of each matrix term, and this reduces uncertainty at conditions where calibrations are difficult. The method also allows for automatic correction of the effects of laser beam steering and optical distortion (bowing) of the laser image. The hybrid method was developed for a specific experimental setup but may be adapted to any Raman/Rayleigh scattering system that is optically well characterized.

4 Measurements in laminar and turbulent jet flames of DME

4.1 Introduction

The emission of carbon dioxide (CO_2) as a greenhouse gas enforces an increased use of renewable fuels. Among a variety of choices dimethyl ether (C_2H_6O) exhibits a number of interesting properties. Chemically dimethyl ether (DME) is the simplest ether. In atmospheric-pressure flames neither preheating of the fuel is necessary nor does condensation occur in the fuel feeding pipes due to sufficient vapor pressure at room temperature. DME is an excellent alternative for Diesel fuel, with low NOx emission levels, low particulate emissions, and a high cetane number for good auto-ignition performance. In terms of Raman/Rayleigh scattering DME stands out due to relatively low C_2 and soot precursor formation that causes significant fluorescence interferences on different Raman bands.

The extension of quantitative line-imaged Raman/Rayleigh scattering to turbulent flames of hydrocarbon species more complex than methane is an important research priority. The present work was initiated as an exploratory study to investigate the temperature-dependent Raman scattering properties of several simple hydrocarbon fuels (ethane, ethylene, propane, and DME) and to assess the prospects of obtaining turbulent flame measurements of the quality appropriate for combustion model validation. The focus was on DME because of the practical relevance noted above and also because, as an oxygenated fuel, DME has the lowest propensity to form soot or soot precursors, which generate strong fluorescence interference in Raman experiments.

Raman scattering spectra were measured in heated flows and in laminar jet flames. Early analysis made it clear that interpretation of Raman/Rayleigh signals from flames of DME (or any of the other tested fuels) was significantly more challenging than for methane flames. The main reason is that the hydrocarbon intermediates formed in these flames constitute significantly higher mole fractions than in corresponding methane flames and their Raman and Rayleigh scattering properties are, in some cases, significantly different than those of the parent fuel.

In partially premixed methane flames it has been demonstrated by Barlow et al. [12] that differences between the mass fraction of CH_4 and the total mass fraction of all hydrocarbons are relatively small. The Raman scattering signal corresponding to C-H bond stretch in the hydrocarbon intermediates overlaps the spectrum of CH_4. Consequently, with appropriate calibration of the temperature dependent response of the 'CH_4 channel', the processed results yield a good approximation of the total hydrocarbon mass fraction and good agreement with laminar flame calculations on profiles of major species, temperature and mixture fraction.

The above fortuitous condition does not hold for DME flames, where laminar calculations show that the total mole fraction of hydrocarbon intermediates can exceed 5% in the fuel-rich region of a partially premixed DME/air flame. Intermediate hydrocarbon species, such as methane (CH_4), ethane (C_2H_6), or ethylene (C_2H_4), exhibit rovibrational Raman bands that spectrally overlap the DME Raman bands and cannot easily be separated, especially when on-chip binning is used in the spectral direction as a noise reduction strategy demonstrated by Miles [70] and for the current experimental setup by Fuest et al. [41]. These intermediate species contribute to measured Raman signal intensities on the same detection channel as used for DME such that the Raman response of this channel depends strongly on the local hydrocarbon composition as well as temperature. Due to huge differences in particular Rayleigh cross sections of important intermediate hydrocarbons the effective Rayleigh cross section also depends on the local hydrocarbon composition. Furthermore, rovibrational Raman transitions of DME and hydrocarbon intermediates spectrally overlap with other species, including rovibrational lines of CO_2, CO, molecular oxygen (O_2), and molecular nitrogen (N_2), and also the spectral region used to monitor fluorescence interference. These crosstalk contributions need to be characterized in-depth when quantifying species mole fractions. In short, Raman/Rayleigh measurements cannot be interpreted in a quantitatively useful way without accounting for the concentrations and scattering properties of the main hydrocarbon intermediates.

This work presents a method for post-processing of line-imaged Raman/Rayleigh scattering measurements in DME/air flames. The method relies on species information derived from laminar flame calculations, as well as detailed information on the scattering properties of relevant molecules. The work is structured as follows: Section 4.2 discusses the experimental setup, briefly introduces the extended matrix inversion method [41], specifies the laminar and turbulent DME/air flames, and outlines laminar flame calculations. In Section 4.3 the role of intermediates in DME/air flames is addressed. It is shown that particularly hydrocarbon intermediates can not be neglected. The impact of the intermediate species upon Raman responses, crosstalks, effective Rayleigh cross sections and mixture fraction is examined. For the first time models to account for intermediate species impact on Raman and Rayleigh responses are proposed and detailed instructions are given to systematically obtain the Raman response characteristics of the fuel and crosstalk channels which rely upon a priori information from laminar flame calculations. At appropriate stages, sensitivity studies are used to show the influence of simplifying assumptions. Following the conceptual explanations, Section 4.4 presents Raman response and crosstalk curves specifically used in this study. Broadband and C_2 interferences are discussed in detail followed by results and discussions of laminar DME/air flames. The applicability of instantaneous line-imaged Raman/Rayleigh/LIF measurements in piloted turbulent premixed and partially-premixed DME/air flames is demonstrated. Finally the most important findings are summarized. Comprehensive details are particularly addressed to readers using combined Raman/Rayleigh- or just Rayleigh- measurements to study any complex hydrocarbon flames.

4.2 Experimental and numerical approach

4.2.1 Experimental setup and data post-processing

Line-imaged multi-scalar measurements were conducted at the Combustion Research Facility of the Sandia National Laboratories with the experimental setup described in Section 2.6. Raman scattering passed a high-transmission thin-film polarizer reducing the crosstalk of depolarized broadband and C_2-fluorescence interferences by up to 50 %. All measurements were repeated with the polarizer turned by 90° to monitor the background and minor contributions from depolarized Raman scattering. Using shot-averaged data subtraction of the depolarized spectra from the polarized spectra was applied to gain insights into the spectroscopic nature of the observed signals. In wavelength direction spectral ranges for both hardware and software binning were selected according to Fig. 3.2. Data post-processing was based on the hybrid matrix inversion method described in Chapter 3 and necessary extensions described in the following.

For hydrocarbon species the hybrid approach purely based on quantum chemical calculations is not feasible because of lacking reliable spectra simulations, particularly for calculating reliable temperature dependencies of integrated Raman signals. Moreover, in DME/air flames, a variety of hydrocarbons contribute to the same channel and a special treatment is required as detailed in Section 4.3. Temperature dependent Raman responses and crosstalk curves for the stable hydrocarbons of interest were determined from measurements in electrically heated gas mixtures and various laminar flames. In Section 4.4.1 Raman response and crosstalk curves are discussed and Appendix A provides supplementary crosstalk curves used in this work.

Representative values for precision and accuracy in temperature and non-hydrocarbon species measurements are detailed in Table 4.1. In this work, measurements in turbulent flames are evaluated using spectrally resolved Raman-data in combination with software-binning, resulting in higher cumulated readout-noise from the CCD. Note that using software-binning shifts the overall precision-limit of the system at flame temperatures from being shot-noise limited to readout-noise limited.

Table 4.1: Average values along the 1D line segment (differences between the outer edges and the center are within a few percent) and selected worst-case values for precision and accuracy at flame conditions in laminar premixed methane/air flat flames for software- (sb) and hardware-binned (hb) data-acquisition. The increase in accuracy values for the turbulent flames is due to higher flame luminosity, fluorescence interference, uncertainties in Rayleigh cross section and Raman responses as discussed in detail in Sections 4.3 and 4.4. Turbulent data was acquired using software-binning.

Scalar	Precision σ (%) hb/sb	Accuracy (%)	Premixed flame	Turbulent flame Accuracy (%)
T	0.9/3	2	$\phi = 0.97, T = 2171\,\mathrm{K}$	3-8 (Max. of 8 % @1400 K, fuel-rich)
N_2	0.8/4	2		3
CO_2	3/9	4		6
H_2O	2.3/6.5	3		6
O_2 ($X_{O_2} = 0.01$)	35/150	2		50 (strong LIF interference in T2)
ϕ or F	2.3/11	5		10
CO	7.5/30	10	$\phi = 1.28, T = 2029\,\mathrm{K}$	20
CO-LIF	6.5/9	10		15
H_2	7.5/40	10		15

4.2.2 Flame configurations

In this study laminar and turbulent rich premixed and rich partially premixed DME/air jet flames were investigated. DME is advantageous compared to other fuels, such as C_2H_4, C_2H_6, or C_3H_8 because of less fluorescence interference levels. The stoichiometric point for DME in air is 6.5 vol%. For the laminar jet flames a nozzle diameter of 8 mm was used. Bulk flow velocities of premixed and partially premixed jets were 2.7 and 2.3 m/s, respectively. Corresponding Reynolds numbers are below 2000. Stoichiometric values of the mixture fraction are $F_{\mathrm{st}} = 0.59$ and 0.26 for L1 and L2, respectively. The jet was shielded from the surrounding environment by a low-velocity (0.3 m/s) laminar coflow of air. All electronic flow controllers (MKS or Tescom) were calibrated against laminar flow elements. Line-imaged multi-scalar measurements were conducted 20 mm downstream of the nozzle exit in radial direction. Two different mixture compositions were used that are termed L1 and L2. The gas compositions of these two flames are provided in Table 4.2. Flame L1 burned with a central premixed cone (tip height ~80 mm) surrounded by a stratified post-oxidation region (Bunsen type flame), where a methane-counterpart was investigated by Chou et al. [30]. Flame L2, having a richer jet mixture, did not exhibit an inner premixed reaction zone and, therefore, provides a flame structure more typical of non-premixed flames, with a single reaction zone near the stoichiometric condition.

Table 4.2: Unburnt gas compositions of laminar premixed and partially premixed DME/air flames in mole fractions, with Ar and CO_2 based on the composition of standard air with 5 % relative humidity. In the experiment the co-flowing air contained 35 % relative humidity (0.007 mole fractions). The gas temperature was 290 K.

	DME	N_2	O_2	Ar	H_2O	CO_2	u (m/s)	*Re*	ϕ
L1	0.114	0.6911	0.1854	0.0083	0.0009	0.0003	2.7	∼1730	1.85
L2	0.281	0.5608	0.1504	0.0067	0.0007	0.0003	2.3	∼1880	5.6

Table 4.3: Unburnt gas compositions of turbulent DME/air flames in mole fractions.

	DME	N_2	O_2	Ar	H_2O	CO_2	u (m/s)	*Re*	ϕ
T1	0.114	0.6911	0.1854	0.0083	0.0009	0.0003	41.0	∼23500	1.85
T2	0.197	0.6264	0.1680	0.0075	0.0008	0.0003	41.0	∼26500	3.5

Multi-scalar measurements were applied to piloted, turbulent DME/air jet flames to investigate the feasibility of applying the present approach to flames of relevance to turbulent combustion model validation. For this purpose the well-known burner configuration of the Sandia-Sydney piloted flame series A - F was used [9–11, 13, 55, 84]. Two DME/air flames were investigated, as detailed in Table 4.3. The gas composition of the lean premixed pilot was CH_4/H_2/air: 0.055/0.055/0.89. This pilot composition was used for simplicity in this first study, knowing that it will be appropriate in future work to match the enthalpy and atom balance of pilot to that of the main fuel at the same equivalence ratio. Stoichiometric values of the mixture fraction are $F_{\mathrm{st}} = 0.59$ and 0.36 for T1 and T2, respectively. The total bulk velocity of the main jet was fixed at 41 ms^{-1}, but the DME/air ratio was varied. Reynolds numbers are 23.500 and 26.500 for T1 and T2, respectively, recalling characteristics of piloted CH_4/air flame D. As will be shown, T2 has a scalar flame structure analogous to the piloted partially premixed CH_4/air jet flames, with most of the heat release occurring in a diffusion controlled reaction zone at the stoichiometric condition. In contrast, flame T1 is a turbulent Bunsen flame, with much of the heat release occurring in a rich premixed reaction zone.

4.2.3 Numerical procedure

The analysis of DME/air flames was supported by 1D computations using three different 1D flame codes as outlined below. Variation of the inflow velocities or strain rate, respectively, was used as the free parameter to reflect the flow velocities of the fuel stream and oxidizer stream in the experiment along the measured 1D line segment.

UC Berkeley Laminar flames were simulated by Chen [29] using both the Tsuji and opposed jet geometries (Fig. 4.1). In the Tsuji geometry, the flame is stabilized in the forward stagnation region of a porous cylinder immersed in a uniform oxidizer flow. The imposed strain on the flame is calculated as

$$a = 2U/R\,, \tag{4.1}$$

where U is the approaching velocity of the oxidizer and R is the radius of the cylinder. With a stagnation flow formulation, the Tsuji flames were computed using the OPPFLOW code developed by Miller et al. [72].

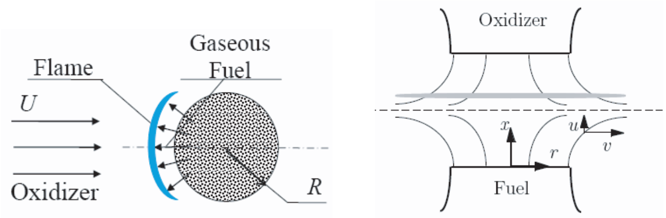

Figure 4.1: Sketch of Tsuji burner (left) and opposed flow burner (right).

In the opposed jet configuration fuel and oxidizer issue from two opposed nozzles and imping against each other. The flame is stabilized between the two jets near the stagnation plane. The global strain rate of the flame is calculated as proposed by Seshadri and Williams [87]

$$a = \frac{U_\mathrm{o}}{H}\left(1 + \frac{U_\mathrm{f}}{U_\mathrm{o}}\sqrt{\frac{\rho_\mathrm{f}}{\rho_\mathrm{o}}}\right)\,. \tag{4.2}$$

Where U_o is the velocity and ρ_o the density of the oxidizer stream and U_f, ρ_F of the fuel stream, respectively. H is the distance between nozzles. The computer code OPPDIF developed by Lutz et al. [65] was used. In case of rich partially-premixed jets, two flame zones form consisting of a rich premixed flame and a diffusion flame. Both flame zones partly overlap resulting in a flame structure more complex than pure premixed or diffusion flames.

Two reaction mechanisms from Zhao et al. [104] (55 species) and Kaiser et al. [54] (78 species) were compared. Planar premixed flame speeds were computed using the PREMIX code by Kee et al. [58] as one method of evaluating differences between the mechanisms. Laminar flame speeds resulting from the two reaction mechanisms are compared in Fig. 4.2. The Kaiser mechanism overpredicts laminar flame speeds, whereas good agreement between results obtained from the Zhao mechanism and experimental data is found by Zhao et al. [104]. Based on this comparison, the Zhao mechanism was used primarily in this work.

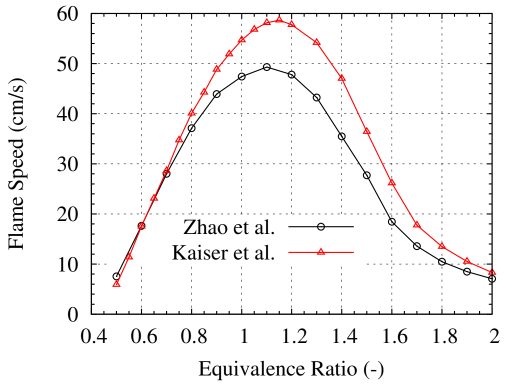

Figure 4.2: Laminar flame speed of DME/air vs. equivalence ratio comparing both mechanisms. Lines between calculated equivalence ratios are interpolated and only included to guide eyes.

However, the differences in species prediction between the two mechanisms are briefly considered in Section 4.3.1. Tsuji flames were simulated over a range of strain rates from $a = 100\,\mathrm{s}^{-1}$ to near-extinction for each of the four DME/air mixtures (L1, L2, T1, and T2), using both multi-component transport and equal diffusivities (mass diffusivity equals thermal diffusivity), with the latter results expected to be more representative of turbulent flames where differential diffusion effects become less obvious. Opposed jet calculations with multi-component transport were done just for L1 and T1 at strain rates of $a = 50$ and $100\,\mathrm{s}^{-1}$. Results are used in the analysis that follows.

TU Darmstadt All configurations were also simulated at different strain rates using the 1D flame solver CHEM1D developed at the Eindhoven University of Technology [4, 21, 96, 97]. Both, the Zhao and Kaiser mechanisms, were used in the opposed jet geometry. The Tsuji geometry was not implemented in the code at TU Darmstadt. As outlined above, both, multi-component and equal diffusivities transport models were used. A detailed comparison of the codes is beyond the scope of this work. However for some of the results curves from all three codes are shown and briefly commented. Figure 4.3 compares results from OPPDIF with CHEM1D, both based on the opposed jet geometry and Zhao mechanism. Boundary conditions of temperature and composition were matched. Strain rates are defined differently in both codes. Hence, the temperature profile of CHEM1D was matched in FWHM to that from OPPDIF. Resulting strain rates were $a = 110\,\mathrm{s}^{-1}$ (CHEM1D) and $a = 50\,\mathrm{s}^{-1}$ (OPPDIF). Used grid points were 262 in the OPPDIF calculation and 200 grid points in CHEM1D. With respect to the comparison in Fig. 4.3 no differences for higher numbers of grid points were observed. Major species and temperature shown in Fig. 4.3a are quite similar for both calculations. Largest differences are observed for CH_4, C_2H_4, C_2H_2, and C_2H_6 which barely shows up in the CHEM1D calculation. Reasons for these differences could not be identified and are not further considered here.

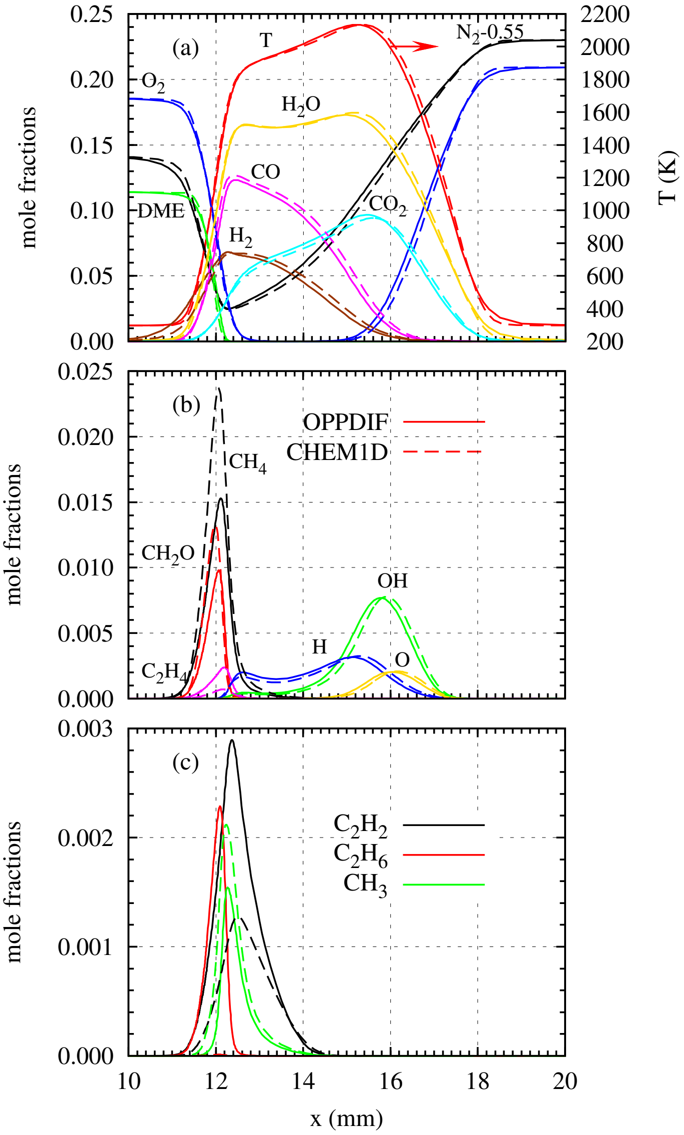

Figure 4.3: OPPDIF (solid) versus CHEM1D (dashed) with Zhao mechanism in L1 configuration, using multi-component transport and strain rates $a = 50\,\mathrm{s}^{-1}$ and $a = 110\,\mathrm{s}^{-1}$, respectively.

In the following, the study of Raman/Rayleigh scattering in DME/air flames is focused on the results from Chen outlined above. Sensitivities with respect to boundary conditions were calculated with CHEM1D and are detailed in the results part below. The impact of radiation on the maximum temperatures was calculated using the Planck mean absorption model [61] included in the CHEM1D code.

4.3 Analysis based on laminar flame calculation

In hydrocarbon flames, Raman and Rayleigh scattering originates from educts, products (major species) and intermediates. In CH_4/air flames these intermediates so far have not been treated systematically because of comparatively low concentrations and relatively minor influence on effective scattering cross sections. As stated in the introduction, Raman/Rayleigh measurements from flames of DME and other more complex fuels cannot be processed using the same simple methods from CH_4 flames; initial attempts in the present study revealed significant inconsistencies.

In this section, results of the laminar DME/air flame calculations are used together with data on integrated Raman signal intensities and Rayleigh scattering cross sections to analyze the influence of hydrocarbon intermediates on Raman and Rayleigh scattering measurements. Details of scattering properties needed for this analysis are provided in Sections 4.3.2 and 4.3.3. Following the identification of all relevant intermediates, the special circumstances resulting from the matrix inversion (MI) method commonly used for evaluation of Raman/Rayleigh scattering are addressed. In the present experimental setup, the spectral region for Raman shifts located between 2775 and 3263 cm^{-1} (hydrocarbon channel) is used to detect the Raman scattering signal from DME and some of the intermediate hydrocarbon species. Details of the superposed spectral signature of the hydrocarbon mix are lost due to pixel binning. Consequently, *a priori* information on composition and temperature must be used. In the approach presented, different models for the Raman response within the hydrocarbon channel, the effective Rayleigh cross section, and the calculation of the mixture fraction are introduced.

4.3.1 Identification of species relevant to Raman/Rayleigh scattering in DME flames

Based on laminar flame calculations described in Section 4.2.3 major and intermediate species are now identified that significantly contribute to Raman and Rayleigh scattering in DME/air flames. This analysis, however, is focused only on fuel/air mixture compositions introduced in Tables 4.2 and 4.3. General observations are reported using just case L2 followed by a discussion of the impact of mixture composition variations, reaction mechanisms from Zhao et al. and Kaiser et al., strain rate variation, and flow geometry (opposed jet and Tsuji). To select relevant species contributing significantly to Raman and Rayleigh scattering a minimum mole fraction of 0.001 was used as threshold. Thereby the seven common major species (CO_2, O_2, CO, N_2, DME, H_2O, H_2), and additionally ten minor species (CH_4, CH_2O, Ar, OH, C_2H_2, H, C_2H_4, O, C_2H_6, CH_3) were identified for further analysis.

For case L2 (28.1 % DME in air) the spatial profiles for mole fractions and temperature are presented in Fig. 4.4. In the top of Fig. 4.4 the common seven major species are shown in comparison to the total mole fraction of nine intermediates (excluding Ar from the ten minor species above). Intermediate species contribute up to a mole fraction of 0.078 at maximum. This peak is located at the fuel-rich side of the flame, with a corresponding temperature of 1239 K at $x = 2.57\,\mathrm{mm}$. The bottom of Fig. 4.4 shows the ten species individually and all remaining low-concentration species are summed up in 'other'. The following observations can be made from these profiles: First, CH_4 and CH_2O are the most abundant intermediates with maximum mole fractions of 0.048 and 0.02, respectively. At $x = 2.66\,\mathrm{mm}$ (1287 K), the corresponding DME mole fraction has approached already 0.03, corresponding to less than half of the intermediates. Second, four intermediate hydrocarbons (CH_4, C_2H_2, C_2H_4, C_2H_6, CH_3) add up to a mole fraction of 0.07. Just these four intermediates contribute to the hydrocarbon Raman channel in the present measurements, but all of them contribute to the effective Rayleigh cross section as shown in Section 4.3.2.3 and 4.3.4. Third, all other species excluded from the seventeen species mentioned above never exceed a total mole fraction of 0.002. In spite of typical experimental sensitivities, especially for single laser shot Raman scattering, such low concentrations are well justified to be neglected.

To evaluate the sensitivity of these findings, a parametric variation of laminar flame calculations was conducted. Using a mixture composition of 19.7 % DME in air, the reaction intermediates sum up to a mole fraction of 0.052, compared to 0.07 in the 28.1 % DME in air flame, both $a{=}100\,\mathrm{s}^{-1}$, multi-component transport. Switching to equal diffusivity transport, the maximum intermediates mole fraction decreases to 0.05. Increasing the strain rate to just below the extinction limit (multi-component: $a{=}1750\,\mathrm{s}^{-1}$ and equal diffusivity: $a{=}2500\,\mathrm{s}^{-1}$) the intermediates mole fraction reduces to 0.035 and 0.028, respectively. The same trends are observed when replacing the Zhao et al. mechanism by the Kaiser et al. mechanism. However, using the Kaiser et al. mechanism, the mole fractions summed up from the same intermediate species in total is reduced by approximately 10 %. It is apparent from these calculations that the total mole fraction of hydrocarbon intermediates decreases with decreasing DME fraction in the fuel/air mixture, decreases with increasing strain rate, and decreases when equal diffusivities are applied rather than multi-component transport. However, the intermediates mole fraction remains important in all cases and must be considered because scattering cross sections, molar masses, and atomic constitutions differ significantly from the parent fuel. Neglecting hydrocarbon intermediates in the evaluation procedure would result in systematic errors in assumed scattering properties, as is detailed in the following sections.

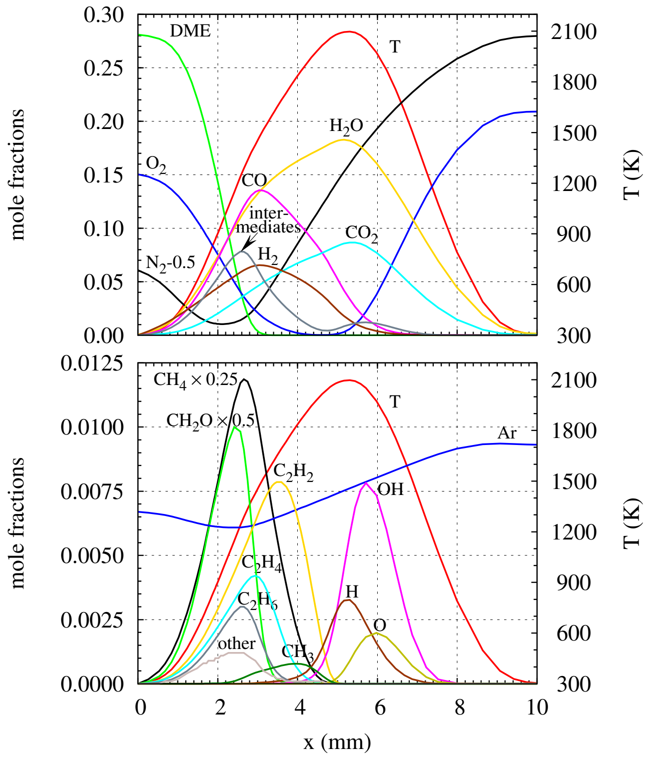

Figure 4.4: Species and temperature profiles from laminar flamelet calculation. Tsuji geometry, Zhao et al. mechanism, a=50 s^{-1}, L2, multi-component transport. In (top) the sum of the species from (bottom) except Ar is shown as 'intermediates'. These seventeen species always represent more than 0.998 mole fractions of all 55 species from the mechanism.

4.3.2 Analysis of Raman scattering from DME and intermediate species

4.3.2.1 Raman spectra

This section provides the spectroscopic details on Raman scattering from DME and important intermediate species. This information is essential for all conclusions derived in Section 4.3 regarding the data processing of the present Raman/Rayleigh measurement in DME/air flames. In the following treatment selected hydrocarbon Raman bands and crosstalks to other Raman channels are examined. For this purpose Raman scattering from DME, CH_4, C_2H_4, or C_2H_6 diluted by ~91 % N_2 were measured in electrically heated jets. The temperature was varied in steps of ~100 K from 295 to 820 K and measured by Rayleigh-scattering. A thin-film polarizer was placed in front of the Raman spectrometer, such that only the polarized or depolarized part was detected, respectively. Figure 4.5 shows two relevant spectral ranges at 295 K (top) and 820 K (bottom), respectively. The

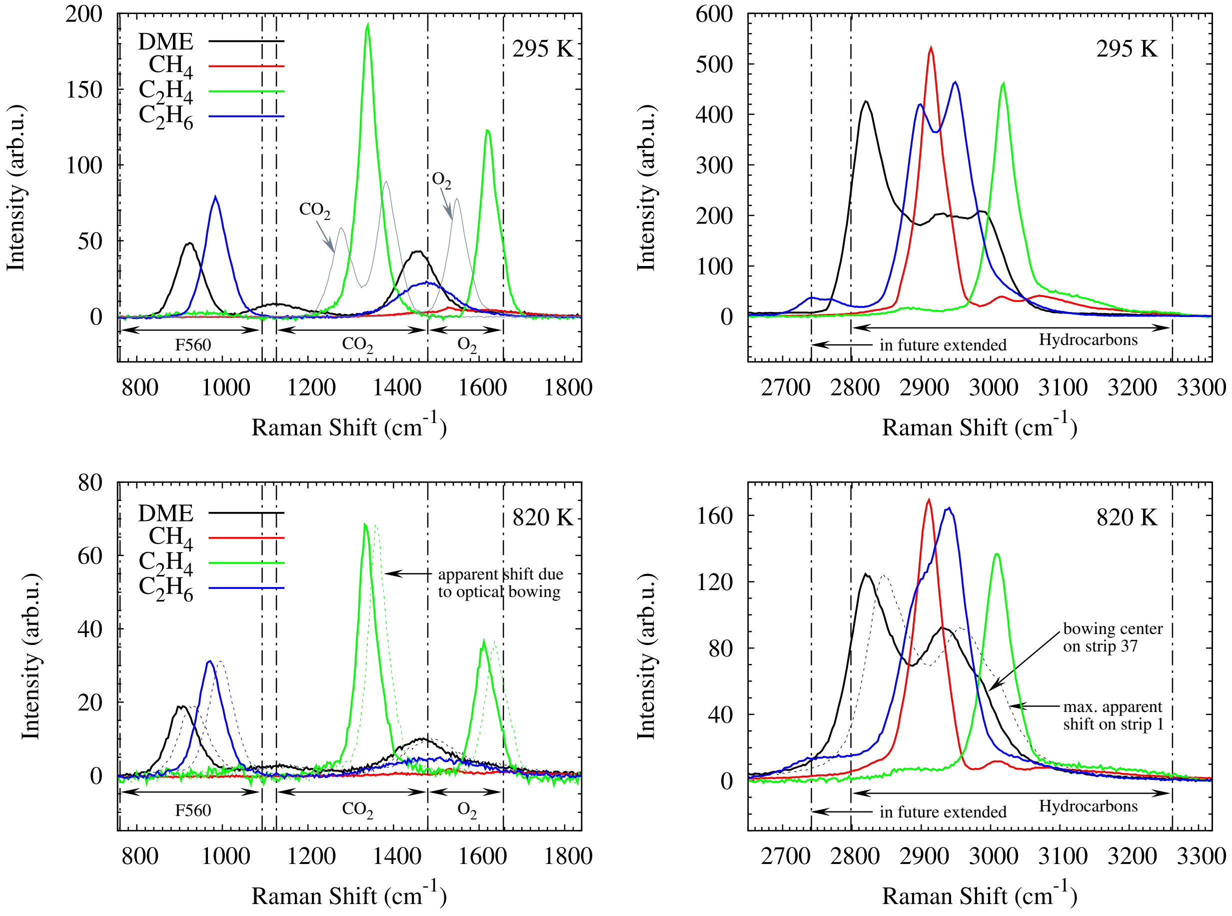

Figure 4.5: Polarized Raman spectra from DME, CH_4, C_2H_4, and C_2H_6, CO_2, O_2 at 295 K (top) and 820 K (bottom). Binning regions for LIF interference (F560), CO_2, O_2, and for the hydrocarbon channel are marked by dash-dotted lines. The hydrocarbon channel already used in previous CH_4/air flame measurements spans from 2800 to 3270 cm^{-1}. In future studies, however, the low-wavenumber edge of the hydrocarbon channel will be shifted to 2740 cm^{-1} to minimize bowing effects and is already marked in the figure. Thus, in addition to CH_4 and C_2H_4, Raman bands of DME and C_2H_6 are contained nearly completely in the hydrocarbon channel. The effect of optical bowing is illustrated by an apparent shift (25 cm^{-1}) of the spectra (bottom, dotted lines) with respect to the binning regions. On bottom right just shown for DME for the sake of clarity.

spectra comprise Raman shifts from 800 to 1800 cm^{-1} and 2650 to 3300 cm^{-1} containing the most intense Raman bands. Relative signal intensity ratios between the molecules scatter within ±10 %. These uncertainties were caused inter alia by flow controllers, remaining uncertainties in crosstalks, temperature measurements via Rayleigh scattering, and laser shot energy correction. Signals at the low wavenumber end were attenuated by decreasing transmission/detection efficiency by roughly 15 %. From Fig. 4.5 it is obvious that DME and the intermediate species C_2H_4, C_2H_6 cause significant crosstalks at lower Raman shifts.

The C_2 fluorescence/broadband interference channel around 760 to 1090 cm^{-1} is affected particularly by DME and C_2H_6. The CO_2 and O_2 channels are heavily influenced by C_2H_4, DME, and C_2H_6 but much less by CH_4. For this reason CH_4/air flames are less sensitive to this specific crosstalk. Another crosstalk on N_2 was observed in DME/air mixtures, causing a systematic increase of the N_2/O_2 ratio by approximately 5 % (for 28.1 % DME in air, see N_2 channel in Fig. 4.18).

Due to the limited spectral resolution of the transmission spectrometer and the complexity of the DME molecule, exact assignments of the DME Raman bands evident from Fig. 4.5 are difficult. However, four separated bands I-IV are observed here and are briefly discussed relying on bands assignments by Allan et al. [5], Blom et al. [19], and Hameka [48]:

I. 2750-3100 cm^{-1}: This is the CH-stretching region that is mainly constituted of five strongly polarized Raman peaks with Raman shifts of 2823 cm^{-1}, 2872 cm^{-1}, 2926 cm^{-1}, 2963 cm^{-1} and 2999 cm^{-1} as reported by Blom et al. [19]. Here, two Raman peaks are most notably because of their apparent change in relative signals at higher temperature. First, the dominating peak in cold gas here observed at 2820 cm^{-1}, which probably results from Fermi resonance of symmetric out-of-plane (C-O-C plane) CH_2 stretch and in-plane CH stretch vibrations as stated by Allan et al. [5]. Second, the peak at 2926 cm^{-1} which is very likely assigned to the asymmetric CH_2 out-of-plane stretch mode (Allan et al.). This peak is notable because it is increasing with temperature, even exceeding the peak at 2820 cm^{-1} for temperatures above 1300 K. This observation is not compulsory an attribute of DME alone, as species such as CH_4 and C_2H_6 are formed at higher temperatures. The superposition of CH_4 and C_2H_6 Raman spectra can be estimated from chemical kinetic calculations evaluating gas compositions at intermediate temperatures around 1300 K and corresponding pure gas spectra. This is supported experimentally by comparing to Raman spectra from laminar jet flames.

II. 1300-1600 cm^{-1}: This range is due to CH_3 deformation modes. The observed DME-peak at 1453 cm^{-1} is formed by three overlapping CH_3 deformation modes, two symmetric and one asymmetric at 1442 cm^{-1}, 1453 cm^{-1}, and 1462.5 cm^{-1}, respectively.

III. 1050-1300 cm^{-1}: CH_3 rocking mode $rCH_3(a_2)$ with a peak at 1131 cm^{-1} and νCOC+ $rCH_3(b_1)$ at 1099 cm^{-1}, which are both comparably weak.

IV. 800-1050 cm^{-1}: COC-stretching region and a peak at 930 cm^{-1}.

Another very weak and polarized Raman scattering feature is observed around 2550 cm^{-1} (not shown) that is not mentioned in the literature cited above. However, a very similar but narrower feature is observed for CH_4, too, which is assigned to a sublevel of the pentad polyad (Boudon et al. [22]).

The other species CH_4, C_2H_4, and C_2H_6 contribute differently to the regions denoted by I to IV. The ν_3 vibration at 994.6 cm^{-1} and ν_{11} at 1468.1 cm^{-1} of C_2H_6 coincide with the regions IV, III, and II from DME, respectively. The first very strong ν_3 peak of C_2H_4 at

1342.4 cm^{-1} from symmetrical CH_2 deformation/bending vibration contributes to regions III and II. The ν_2 peak at 1623.3 cm^{-1} from C=C vibration (see Herzberg [51]) causes severe crosstalk on O_2, especially at higher temperatures and small O_2-concentrations which is extremely difficult to compensate. The crosstalk from ν_2 from CH_4 (Jourdanneau et al. [53]) on O_2 around 1530 cm^{-1} is quite small compared to the other hydrocarbons. The ν_1 band from CH_3 has a Raman shift of 3002 cm^{-1}. The $2\nu_2$ band at 1284 cm^{-1} scatters on the CO_2 channel, and $\nu_1 + 2\nu_2$ is observed at 4286 cm^{-1} (Kelly and Westre [59]), where the channel to monitor the background starts. The relative signal intensity of the CH_3-ν_1 band has been measured by CARS by Hädrich et al. [47] and is one quarter relative to CH_4. The transferability from this narrow peak value to the relative signal intensity across the entire hydrocarbon channel is somehow speculative and causes uncertainties. However, the methyl radical occurs only at low concentrations (Fig. 4.4), and its contribution to the hydrocarbon channel at intermediate temperatures is rather small. At high temperatures, however, its concentration relative to other hydrocarbons is high but its absolute concentration level is very low.

4.3.2.2 Relative Raman signals

Following these general discussions of species-specific Raman spectra, this section provides relative Raman signals that were obtained from integration of the different detection channels at one center strip. In addition to the species DME, CH_4, C_2H_4, and C_2H_6 measured in this study, contributions by other species such as CH_2O, C_2H_2, OH, and indirect contributions from Ar, O, and H are discussed. Tables 4.4 to 4.7 summarize integrated Raman signals $S_{\mathrm{Ram,i}}/S_{\mathrm{Ram,DME}}$ of species i relative to DME. Information on species not measured in this work is addressed below.

Table 4.4: Relative integrated Raman signals $S_{\mathrm{Ram},i}/S_{\mathrm{Ram,DME}}$ for the hydrocarbon channel.

Molecule	Relative integrated Raman signals for 2798 to 3263 cm^{-1}	
	295 K	820 K
DME	1	1
CH_4	0.64	0.64
C_2H_4	0.55	0.57
C_2H_6	1	1
CH_3		0.16[a]
C_2H_2		0
CH_2O		0

[a] from Hädrich et al. [47], ν_1, 450 K.

CH_2O: Information on the Raman scattering from formaldehyde is available for a temper-

Table 4.5: Relative integrated Raman signals $S_{\mathrm{Ram},i}/S_{\mathrm{Ram,DME}}$ for crosstalk on the F560 channel.

Molecule	Relative integrated Raman signals for 761 to 1093 cm^{-1}	
	295 K	820 K
DME	1	1
CH_4	0	0.003
C_2H_4	0.203	0.91
C_2H_6	1.43	1.37
CH_3		0

Table 4.6: Relative integrated Raman signals $S_{\mathrm{Ram},i}/S_{\mathrm{Ram,DME}}$ for crosstalk on the CO_2 channel.

Molecule	Relative integrated Raman signals for 1127 to 1481 cm^{-1}	
	295 K	820 K
DME	1	1
CH_4	0.064	0.09
C_2H_4	2.83	3.28
C_2H_6	0.51	0.54
CH_3		0.02[a]

[a] from Hädrich et al. [47], ν_1, 450 K.

ature of 423 K measured by Wiegeler and Bleckmann [102] while Bruna et al. [25] report on *ab intio* calculations. All six normal mode vibrations are Raman active, but only three of them exhibit significant intensities. The strongest one originates from the symmetric C-H stretch ν_1 at 2782.2 cm^{-1} and contributes partly to the blue end to the hydrocarbon channel but only at the outside strips (approximately strip 1 to 5), due to the optical bowing effect. This peak were searched in from shot-averaged and spectrally resolved data recorded in laminar jet flames of various fuels (CH_4, DME, C_2H_4, C_2H_6, C_3H_8). Only in case of C_2H_4 with the most separated Raman band located around 3020 cm^{-1}, a small peak is observable near 2780 cm^{-1}. This might be explained by the fact that CH_2O is mainly occurring at temperatures below 1800 K and the spectral region below 2800 cm^{-1} is dominated by scattering from other intermediate hydrocarbons. The peaks from the C-O stretch ν_2 at 1745.1 cm^{-1} (between O_2 and CO) and CH_2 stretch ν_3 at 1500.2 cm^{-1} (on O_2) are ten times weaker than the feature at 2780 cm^{-1} and were neglected here.

C_2H_2: Acetylene is considered separately here because it does not contribute to any Raman channels in the present experiments. Information on fundamental vibration modes and corresponding Raman shifts for acetylene were taken from Herzberg [51]. The C≡C vibration Raman shift of 1973.8 cm^{-1} is positioned between the channels of O_2 (O_2 channel ends

Table 4.7: Relative integrated Raman signals $S_{\mathrm{Ram},i}/S_{\mathrm{Ram,DME}}$ for crosstalk on the O_2 channel.

Molecule	Relative integrated Raman signals for 1484 to 1657 cm^{-1}	
	295 K	820 K
DME	1	1
CH_4	0.53	0.27
C_2H_4	4.41	3.21
C_2H_6	1.19	0.85
CH_3		0.07[a]

[a] from Hädrich et al. [47], ν_1, 450 K.

between 1635 and 1657 cm^{-1}) and CO (CO channel starts between 1990 and 2015 cm^{-1}). The Raman band of the C-H vibration is about nine times weaker and has a Raman shift of 3373.7 cm^{-1}, which is located close to the H_2O channel starting at 3409-3430 cm^{-1}. Considering the intensity ratio of acetylene (Stephenson [90], Wiegeler and Bleckmann [102]), its spectral broadening at flame temperature (Mokhov et al. [73]), maximum concentrations deduced from laminar flame calculations, and experimental spectra, it was concluded that no signal will be detected on any of the adjacent channels.

Ar, O, H, OH: The atomic species Ar, O, and H are not Raman active but contribute to Rayleigh scattering. Assuming room temperature, N_2, and O_2 calibration on exact concentrations in air, neglecting Argon would result in a 0.5 % too high effective Rayleigh cross section and temperature in the unburnt DME/air mixture of T2. This deviation decreases to about 0.1 % at flame temperature. O and H atoms occur only in a narrow temperature band around 2100 K and their negligence would evoke an error at these high temperatures of about +0.8 %. However, the major part of this inaccuracy will decrease to 0 to 0.3 % when concurrently assuming parts of the hydroxyl radical being detected on the Raman channel for water or when even neglecting the OH contribution completely as in Sutton et al. [92]. In fact, the main Raman band from OH at 3568.4 cm^{-1} coincides with the Raman channel for water. Assuming $S_{\mathrm{Ram,OH}} = 0.5 S_{\mathrm{Ram,H_2O}}$ as described by Linow et al. [63], considering common OH/H_2O ratios around 5 to 6 % at locations of the highest OH concentrations would lead to a maximum overestimation of $X_{\mathrm{H_2O}}$ of 2 to 3 %. Generally, this Raman crosstalk on H_2O was partly compensated due to a H_2O calibration in flat flames with similar equilibrium OH concentrations, and was not treated particularly here, too.

4.3.2.3 Analysis of Raman scattering response

Temperature dependent distributions of DME and relevant intermediate hydrocarbon species from laminar flame calculations are now used with the information from the preceding section to quantify their impact on the Raman response of the hydrocarbon channel. A strong Raman crosstalk on CO_2 and O_2 is further addressed in Section 4.4. In the following treatment sensitivities of Raman response to strain, transport, mixture composition, and geometry are investigated. For this sensitivity study, integrated Raman signal intensities from DME and intermediate hydrocarbons are assumed not to vary with temperature. Referring to Table 4.4, this simplification is well justified up to 820 K as measured in the heated gas flows. However, this restriction is not applied for the final data evaluation of the flames. Response curves in Section 4.4 differ accordingly and linear extrapolations of measured temperature dependences to higher temperatures are included (compare Fig. 4.14). Note also that the effects of optical bowing in the spectrometer as indicated in Fig. 4.5 and resulting strip-dependence of the Raman response are included in the final data analysis. This is not discussed here for simplicity of presenting the conceptual approach.

The analysis that follows is for the center of the bowed image. The hydrocarbon channel ranging on this center strip from $2798\,\mathrm{cm}^{-1}$ to $3263\,\mathrm{cm}^{-1}$ covers a major part of the spontaneous Raman scattering originating from DME, CH_4, C_2H_4, C_2H_6, and CH_3. Concurrently, remaining hydrocarbons like CH_2O and C_2H_2 are not contributing to this spectral range because of their different Raman shifts. As the integrated Raman scattering signal is linear with number density, the temperature dependence of the collective response on the hydrocarbon channel $S_{\mathrm{Ram,HC}}$ is described by a linear combination of the five relative hydrocarbon mole fractions $X_i(T)/\sum_{j=1}^{5} X_j(T)$ weighted by their corresponding relative signals $S_{\mathrm{Ram},i}/S_{\mathrm{Ram,DME}}$

$$S_{\mathrm{Ram,HC}}(T) = \frac{\sum_{i=1}^{5} X_i(T) \frac{S_{\mathrm{Ram},i}}{S_{\mathrm{Ram,DME}}}}{\sum_{j=1}^{5} X_j(T)} \,. \tag{4.3}$$

This temperature dependence solely comes from the decomposition and oxidation reactions of hydrocarbons at rising temperatures. Density effects are excluded from Eq. (4.3). Raman responses based on Eq. (4.3) are shown in Fig. 4.6.

Obviously, the consumption of hydrocarbon species by chemical reactions depends on boundary conditions. Therefore the Raman response in Eq. (4.3) has been derived using $X_i(T)$ from laminar flame calculations, various strain rates, transport models, flow geometries, and mixture compositions. For the T2 mixture composition (19.7 % DME in air), the Raman response differs up to 20 % at 1500 K when the strain rate increases from $100\,\mathrm{s}^{-1}$ to $2500\,\mathrm{s}^{-1}$. Switching the transport model from multi-component to equal diffusivities yields small differences in the range of 1 to 3 %. Similar variations are observed for the mechanism by Kaiser et al. (not shown). Results of the L1 mixture composition (11.4 % DME in air) are shown for the opposed flow configuration. Although this flame burns with an inner premixed cone the Raman response is bounded by the results for the diffusion-flame-like cases. It is concluded from this analysis that the proposed model approach simplifies the physical-chemical processes, especially for turbulent flames with varying influence of molecular transport effects, strain, flow patterns, or even local extinc-

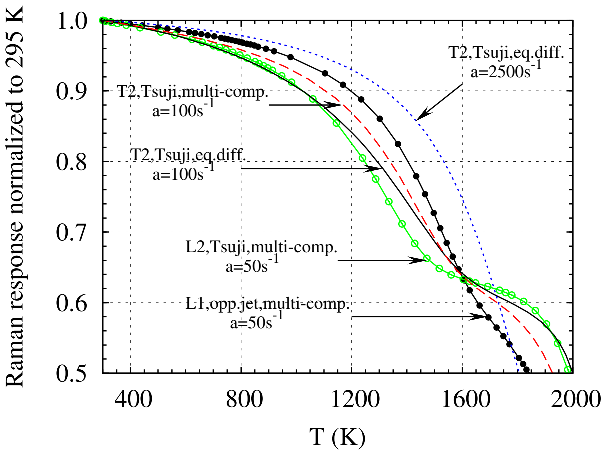

Figure 4.6: Sensitivity of the Raman response on the hydrocarbon channel to strain, transport model, and geometry using Eq. (4.3) and constant signal intensity ratios from Table 4.4 (right column, 820 K).

tion. However, Section 4.4 will show its practicability by presenting results which are based on different Raman responses, each corresponding to an appropriate laminar calculation.

Intensity ratios describing the crosstalk onto detection channels for the fluorescence interference channel, CO_2, and O_2 at lower Raman shifts are provided in Tables 4.5-4.7. At these lower Raman shifts differences in scattering intensities are much more pronounced among the individual hydrocarbon molecules because their rovibrational bands are separated. The crosstalks onto the O_2, CO_2, and fluorescence channels are discussed in detail in Section 4.4.

4.3.3 Rayleigh cross sections of relevant species

In DME/air flames various intermediate species in addition to educts and products are identified that contribute to Rayleigh scattering (see Section 4.3.1). Referring to Eq. (4.13) the effective Rayleigh cross section contains mole fraction weighted species-specific cross sections. These cross sections are needed as a basis for the discussions in Section 4.3.4.

In this study data from the literature were screened. For a few hydrocarbons additional measurements were performed. Table 4.8 summarizes Rayleigh cross sections and depolarization ratios relative to N_2 for different excitation wavelengths. Values in bold type were used for the Rayleigh cross section model discussed in Section 4.3.5. DME was substituted by 8.9, the average value measured in laminar jet flows. Some values for common species like C_3H_8, He, NO, C_2H_5OH, C_2H_4O, C_3H_6O were actually not used in this study but derived and listed as well.

The Eqs. (2.93) and (2.94) are the base to calculate values in the rightmost column in

Table 4.8. All values are listed normalized to nitrogen. Following the procedure applied for $\lambda_0 = 488\,\mathrm{nm}$ by Carter [27] refractive indices were calculated from Gardiner et al. [42] – except for CH_2O where no data on the refractive index are available – using $(n-1) = a/(b - \lambda_0^{-2})$ with $\lambda_0 = 532\,\mathrm{nm}$. Depolarization ratios for linear polarized incident light are listed in the second column of Table 4.8 based on experimental values from Bridge and Buckingham [23], Rowell et al. [82], Bogaard et al. [20], Murphy [76], and a static calculation by Bacskay et al. [7]. Most of them were derived from interpolation to 532 nm using values for 488 nm and 632.8 nm or 514.5 nm and 632.8 nm. In the following some more background information is provided detailing assumptions and sensitivities regarding depolarization ratios, treatments of CH_3 and CH_2O and the experimental measurements performed to cross-check the Rayleigh cross sections of DME, CH_4, C_2H_4, and C_2H_6 versus values listed in the rightmost column of Table 4.8.

Impact of uncertainties in depolarization ratios upon Rayleigh cross sections

The contribution of the depolarization ratio ρ on a species-specific cross section constitute a few percent only. Thereby the sensitivity of species-specific total Rayleigh cross sections upon the depolarization ratio generally is low. Uncertainties in ρ resulting from measurement uncertainties are of minor impact and negligible. For example CO_2 exhibits the largest depolarization ratio. Even assuming an error of $\pm 10\,\%$ in $\rho_{\mathrm{CO_2}}$, which is five times larger than given by Bogaard et al. [20] for the experimental uncertainty in $\rho_{\mathrm{CO_2}}$ impacts $\sigma_{\mathrm{Ray,CO_2}}$ by just $\pm 1\,\%$ using Eq. (2.93).

Linear interpolation of depolarization values

As mentioned values for depolarization ratios ρ were derived by interpolation using values at 488 nm or 514.5 nm and 632.8 nm. Exemplified by N_2, interpolation errors are negligible. Using the dispersion relation for N_2 calculated by Pecul and Rizzo [78] from quantum mechanical ab initio methods, values for 488, 532 and 632.8 nm were derived. The linear interpolation using 488 and 632.8 nm mismatches the value at 532 nm by less than 0.05 %, which is below the smallest experimental uncertainties discussed by Bogaard et al. [20] and does not impact the calculation of the N_2 Rayleigh cross section significantly.

Treatment of CH_3

For the methyl radical CH_3 no measurements of refractive index and depolarization ratio are available. Therefore the refractive index was estimated using atomic and bond refractivities from Gardiner et al. [42]. Applied to CH_4 indeed this estimation provides values quite close to the value derived from Eq. (2.93) based on a measured refractive index (rightmost column in Table 4.8 for CH_4: cross section derived by atomic and bond refractivities is 2.2016 and

Table 4.8: Differential Rayleigh cross sections relative to N_2 and depolarization ratios ρ for linear polarized incident light and specific detection geometry outlined in the text. Cross sections used in the present work are highlighted by bold types and are based on Eqs. (2.93) and (2.94).

		$(\partial\sigma/\partial\Omega)/(\partial\sigma/\partial\Omega)_{N_2}$		
Molecule	100ρ ^{b,g,h,i,j,k}	532 nm^{exp}	488 nm^{a}, 632 nm^{b,c}, static^{d}	532 nm^{e,f}
CO_2	4.0798^{g}		2.32^{a}, 2.3866^{c}	**2.3907**
O_2	2.9434^{h}		0.85^{a}, 0.855^{b}	**0.8592**
CO	0.5132^{g}		1.25^{a}, 1.237^{b}, 1.2346^{c}	**1.2446**
N_2	1.0612^{h}	1	1	**1**
CH_4	0.02^{k}	2.14±0.3	2.16^{a}	**2.1337**,2.2016^{f}
H_2O	0.03^{i}		0.71^{a}	**0.6946**
H_2	0.9044^{h}		0.22^{a}, 0.216^{b}	**0.2124**
OH				**1.4859**
Ar	0		0.87^{a}	**0.8650**
O	0		0.17^{a}	**0.1713**
H	0		0.15^{a}	**0.1479**
DME	0.3679^{g}	**8.9**±0.35	8.5841^{c}	8.6473
C_2H_4	1.2411^{g}	4.7±0.7	5.85^{a}, 5.776^{b}, 5.7312^{c}	**5.8029**
C_2H_6	0.1847^{g}	6.22±0.9	6.33^{b}, 6.3558^{c}	**6.2984**
C_3H_8	0.2061^{g}	12.2±1.7	12.6835^{c}	12.7542
CH_2O	0.95^{j}		**1.99**^{d}	
C_2H_2	1.8834^{g}		4.01^{b}, 3.9658^{c}	**4.0096**
CH_3				**1.5770**^{f}
He	0		0.013^{a}	0.0132
NO	1.54^{b}			0.9834
C_2H_5OH (Ethanol)				8.0026
C_2H_4O (Acetaldehyde)	0.3292^{g}			6.7971
C_3H_6O (Acetone)	0.5862^{g}			13.2247

[exp] present measurements.
[a] from Carter [27].
[b] exp. at 632.8 nm from Bridge and Buckingham [23].
[c] exp. at 632.8 nm from Bogaard et al. [20].
[d] static calc. from Bacskay et al. [7], referenced on calculated static value for N_2 from Pecul and Rizzo [78], Table I, d-aug-cc-pVQZ.
[e] from exp. refractive indices at 532 nm from Gardiner et al. [42].
[f] from refractive indices based on atomic and bond refractivities at 532 nm from Gardiner et al. [42].
[g] linear interpolation to 532 nm from exp. using 514.5 nm and 632.8 nm from Bogaard et al. [20].
[h] linear interpolation to 532 nm from exp. using 488 nm and 632.8 nm from Rowell et al. [82].
[i] from exp. at 515.5 nm from Murphy [76].
[j] derived from static calc. by Bacskay et al. [7], $\rho = \Delta\alpha^2/(15\overline{\alpha}^2 + 4/3\Delta\alpha^2)$.
[k] from Sneep and Ubachs [88].

deviates by less than 4% from the value based on measured refractive index 2.1337). This provides confidence that the calculated value 1.5770 of the relative cross section for CH_3 is trustworthy. The depolarization ratio of CH_3, however, is arbitrarily set to zero. This is justified by the generally low impact of the depolarization ratio upon the cross section that is negligible compared to the uncertainties in the refractive index.

Treatment of CH_2O

The Rayleigh cross section for CH_2O was derived from calculations of static polarizabilities by Bacskay et al. [7] in the molecule fixed coordinate system. These were converted to the polarizability tensor invariants, see Eqs. (2.37) and (2.38), by

$$\overline{\alpha}^2 = \frac{1}{9}(\alpha_{\underline{\underline{\mathrm{xx}}}} + \alpha_{\underline{\underline{\mathrm{yy}}}} + \alpha_{\underline{\underline{\mathrm{zz}}}})^2 \tag{4.4}$$

and

$$\Delta\alpha^2 = \frac{1}{2}\left\{(\alpha_{\underline{\underline{\mathrm{xx}}}} - \alpha_{\underline{\underline{\mathrm{yy}}}})^2 + (\alpha_{\underline{\underline{\mathrm{yy}}}} - \alpha_{\underline{\underline{\mathrm{zz}}}})^2 + (\alpha_{\underline{\underline{\mathrm{zz}}}} - \alpha_{\underline{\underline{\mathrm{xx}}}})^2\right\} . \tag{4.5}$$

These were inserted into

$$\frac{(\partial\sigma_{\mathrm{Ray}}/\partial\Omega)_i}{(\partial\sigma_{\mathrm{Ray}}/\partial\Omega)_{\mathrm{N_2}}} = \frac{\overline{\alpha}_i^2 + (7/45)\Delta\alpha_i^2}{\overline{\alpha}_{\mathrm{N_2}}^2 + (7/45)\Delta\alpha_{\mathrm{N_2}}^2} \tag{4.6}$$

to obtain the differential Rayleigh cross section for CH_2O relative to nitrogen, see Eq. (2.84). To minimize systematic deviations due to use of polarizabilities of different excitation wavelengths as well static N_2-values for $\overline{\alpha}$ and $\Delta\alpha$ were used from Pecul and Rizzo [78]. With this procedure one obtains a relative CH_2O Rayleigh cross section of 1.99 listed in the forth column of Table 4.8. The depolarization ratio was calculated by Eq. (2.88). Note that in these calculations a static polarizability was used because of lack of values at 532 nm. However, the wavelength dependence is rather small. Comparing for example polarizabilities of N_2 at 315 nm versus the static value the deviation is about 4 % Pecul and Rizzo [78]. The impact is even smaller when cross sections relative to N_2 are considered, as the mean polarizability $\overline{\alpha}$ rises with increasing excitation frequencies similarly for the other molecules. The change in the anisotropy $\Delta\alpha$ in this context can be completely neglected.

Based on Eq. (4.6) differential Rayleigh cross sections were calculated additionally for CO_2, O_2, CO, H_2, C_2H_4, C_2H_6, and C_2H_2 using literature values from Bridge and Buckingham [23] and Bogaard et al. [20] for an excitation wavelength of 632 nm. The anisotropy $\Delta\alpha$ of C_2H_4 is not listed by Bridge and Buckingham and was calculated using Eq. (2.88). Resulting values are listed in the forth column of Table 4.8. A comparison to the values based on Eq. (2.93) and 532 nm in the fifth column shows a close agreement with typical deviations in the order of 1 %.

Experimental determination of Rayleigh cross sections for DME and selected hydrocarbons

Combined Raman/Rayleigh scattering measurements were performed in air, DME/N_2 and DME/air mixtures issuing from the jet nozzle. Using pure DME jets was not possible with the present focusing of the laser beam because of optical breakdown, i.e. described by Raizer [81], even at the lowest laser pulse energy. Measurements of DME/air and DME/N_2 were necessary to evaluate the unknown Raman crosstalk from DME on N_2 (quantification of this crosstalk was complicated by the fact that no data without presence of N_2 was available in the present investigations). This was achieved by the following steps. First, the crosstalk of DME upon the O_2-channel ($O_2 \leftarrow$DME) was quantified from the DME/N_2 jet measurements. Second, the DME/air jet was examined. Using the corrected O_2 mole fractions based on the crosstalk $O_2 \leftarrow$DME, the crosstalk of DME upon the N_2-channel was adjusted to recover the correct ratio of N_2/O_2 mole fractions in air. For each mixture composition and temperature setting 100 single shots were recorded. The reference gas temperature was monitored by a thermocouple. Inaccuracies of the flow controllers were avoided by measuring absolute Raman scattering from O_2 before recording the different DME/air mixtures. The DME/N_2 measurement was used to quantify the crosstalk from DME on O_2 and accounted for it in the DME/air measurements. The mole fraction of DME was specified by $1 - X_{\mathrm{air}}$, where X_{air} was determined from the measured O_2 concentration adding the corresponding parts of N_2, CO_2, Ar and H_2O in air. By this procedure mole fractions of DME, O_2, N_2, CO_2, Ar, and H_2O in the jet were known and subsequently used to compute the Rayleigh cross section of DME from the corresponding Rayleigh measurement to match the temperature reading of the thermocouple. The corresponding Eqs. (4.7) to (4.12) used for these calculations are given below. This procedure was repeated for various DME/air ratios on different days, comparing shot-averaged and single-shot evaluation. Finally, the resulting value for the Rayleigh cross section of DME relative to N_2 was 8.9 ± 0.35. Within the error margins this value coincides with values listed in the rightmost column of Table 4.8. Uncertainties of this method are dominated by the remaining uncertainty in the O_2 concentration. This uncertainty was below 0.5% difference in successive measurements of O_2 in air. Assuming $\pm 0.5\,\%$ in the O_2 concentration yields an uncertainty in the relative DME cross section of ± 0.35. This is in agreement with deviations between different measurements.

$$\sigma_{\mathrm{eff}} = TS_{\mathrm{Ray}}/c_{\mathrm{Ray,calib}} \tag{4.7}$$

$$\sigma_{\mathrm{eff}} = X_{\mathrm{air}}\sigma_{\mathrm{air}} + (1 - X_{\mathrm{air}})\sigma_{\mathrm{DME}} \tag{4.8}$$

$$X_{\mathrm{air}} = \frac{1}{0.20914} X_{\mathrm{O_2}} \tag{4.9}$$

$$X_{\mathrm{O_2}} = C_{\mathrm{O_2}} \cdot 22.413996 \cdot 10^{-3}\,\mathrm{m^3 mol^{-1}} \frac{T}{273.15\,\mathrm{K}} \frac{101.325\,\mathrm{kPa}}{p} \tag{4.10}$$

$$\begin{aligned} C_{\mathrm{O_2}} = \frac{1}{c_{\mathrm{Ram,O_2}}} \Bigg(S_{\mathrm{Ram,O_2}} - \frac{c_{\mathrm{Ram,O_2 \leftarrow DME}}}{c_{\mathrm{Ram,DME}}} \Bigg(S_{\mathrm{Ram,DME}} - \\ S_{\mathrm{Ram,bck}} \frac{n_{\mathrm{pixel,DME}}}{n_{\mathrm{pixel,bck}}} \Bigg) - S_{\mathrm{Ram,bck}} \frac{n_{\mathrm{pixel,O_2}}}{n_{\mathrm{pixel,bck}}} \Bigg) \end{aligned} \tag{4.11}$$

$$\Rightarrow \sigma_{\mathrm{DME}} = \frac{TS_{\mathrm{Ray}} - c_{\mathrm{Ray}} X_{\mathrm{air}} \sigma_{\mathrm{air}}}{c_{\mathrm{Ray}}(1 - X_{\mathrm{air}})} \tag{4.12}$$

σ_{eff}	: Effective Rayleigh cross section in the probe volume
T	: Temperature in probe volume determined by thermocouple
S_{Ray}	: Integrated Rayleigh scattering signal
$c_{\mathrm{Ray,calib}}$	: Rayleigh temperature calibration constant, determined in pure air
X_i	: Mole fraction of species i in probe volume
σ_{air}	: Relative Rayleigh cross section of air (0.9693)
σ_{DME}	: Relative Rayleigh cross section of DME
0.20914	: Mole fraction of O_2 in air containing 0.0015 water
$C_{\mathrm{O_2}}$	: Concentration of O_2 in $10^3\mathrm{m^{-3}mol}$ (mol/l)
p	: Pressure in laboratory, measured with manometer
$c_{\mathrm{Ram,O_2}}$	: Raman calibration constant for O_2, determined in pure air
$\frac{c_{\mathrm{Ram,O_2 \leftarrow DME}}}{c_{\mathrm{Ram,DME}}}$	: Ratio of Raman calibration constants for crosstalk of DME on O_2 ($c_{\mathrm{Ram,O_2 \leftarrow DME}}$) and DME ($c_{\mathrm{Ram,DME}}$). Determined in DME/$N_2$ ($\sim 9\,\%$ DME) mixture.
$S_{\mathrm{Ram,O_2}}$	: Signal (counts - (averaged dark image)) on Raman O_2 channel
$S_{\mathrm{Ram,DME}}$	: Signal on Raman DME channel
$S_{\mathrm{Ram,bck}}$	: Signal on Raman background channel
$n_{\mathrm{pixel},i}$	: Number of pixels of Raman channel i
$22.143996 \cdot 10^{-3}\,\mathrm{m^3mol^{-1}}$	: Molar volume of ideal gas (273.15 K, 101.325 kPa)

The relative Rayleigh cross sections of CH_4, C_2H_4, C_2H_6 , or C_3H_8 were determined by diluting these gases with $(91 \pm 1.5)\,\%$ N_2. The mixture composition was determined by relying on the flow controller settings. Thus, differences to literature values particularly for C_2H_4 and C_2H_6 may be caused by flow controller uncertainties.

Other possible sources of experimental errors

The large solid angle of the first collection lense has a different impact on the angular dependence of the Rayleigh signal for species with different depolarization ratios. Therefore, it affects even values normalized to nitrogen. The effect was computed using equations (53)-(55) from Miles et al. [71] and appropriate integration over ±15° detection angle corresponding to the used collection lense. It is found $+0.1\,\%$ for the values of oxygen and carbon dioxide and much smaller for all other molecules. Accordingly, this effect is negligible compared to other experimental uncertainties. A slightly bigger impact ($<0.5\,\%$) can be due to variations in the index of refraction in the beam path of the laser and the scattered light which cause slight differences in the optical imaging for different gases measured. In the same order all experimentally derived values were particularly affected by the background treatment of the Rayleigh image. Here background contributions to the Rayleigh signal were estimated from pixel rows above and below the line Rayleigh image: representative background intensities were calculated by averaging few rows that are clearly separated from the Rayleigh image. Pixel-wise interpolation in vertical pixel direction provided then an estimation of the background underlying the Rayleigh image and was subtracted as the first step in data post-processing. Another source for minor deviations between measured and literature data may result from impurities of the gases as remarked in Bogaard et al. [20].

4.3.4 Effective Rayleigh cross section

The laminar flame calculations from Section 4.3.2.3 are also used to understand the influence of the intermediate species on the Rayleigh temperature measurements. The Rayleigh signal intensity is proportional to the effective Rayleigh cross section. The effective Rayleigh cross section is determined from a linear combination of species-specific Rayleigh cross sections $\sigma_{\mathrm{Ray},i}$ weighted by the respective mole fractions X_i

$$\sigma_{\mathrm{Ray,eff}} = \sum_i X_i \sigma_{\mathrm{Ray},i}. \tag{4.13}$$

In the data evaluation of simultaneous Raman/Rayleigh measurements, species mole fractions are determined from the Raman responses on the different channels. These mole fractions are used to calculate the Rayleigh cross section of the mixture. Then the matrix Eq. (2.96) is solved iteratively since Raman responses depend on temperature as outlined in Section 2.4.2. In contrast, Rayleigh cross sections are independent or only weakly dependent on temperature. In practice, Rayleigh cross sections measured at room temperature are used throughout the whole temperature range in flames. This assumption of constant cross sections may cause a bias towards low temperatures by up to 2 % as remarked by Sutton et al. [92], see also discussion in Section 2.5.2. However, according to the authors' experience for the present flames, this systematic deviation is below 1 %. Hence, temperature dependencies of Rayleigh cross sections are neglected in the following analysis.

In this study Rayleigh cross sections based on refraction indices from Gardiner et al. [42] for 532 nm excitation wavelength along with a static value from Bacskay et al. [7] for formaldehyde are used. All values are normalized to N_2 and were given in Table 4.8. The seventeen relevant species identified in Section 4.3.1 are now further considered to assess their contributions to Rayleigh scattering. Contributions to the Rayleigh signal from all other lower-concentrated species are not significant and are neglected. Contributions from Ar, O, H, and OH are neglected as well (see Section 4.3.2.2). Therefore, thirteen species remain (CO_2, O_2, CO, N_2, DME, H_2O, H_2 ,CH_4, CH_2O, C_2H_2, C_2H_4, C_2H_6, CH_3), and the effective Rayleigh cross section for DME/air flames reads,

$$\sigma_{\mathrm{Ray,eff,ref}} = \frac{\sum_{i=1}^{13} X_i(T,a)\sigma_{\mathrm{Ray},i}}{\sum_{i=1}^{13} X_i(T,a)} \,. \tag{4.14}$$

Mole fractions are denoted here as functions of both temperature T and strain rate a, expressing their dependence upon the specific laminar flame calculation. This Rayleigh cross section is denoted as 'reference' because all mole fractions X_i of the contributing species are assumed to be known, whereas, in the experiment, this assumption is true only for the major species (CO_2, O_2, CO, N_2, H_2O, H_2). Since both C_2H_2 and CH_2O do not contribute to the signal on the hydrocarbon channel, data from this channel represent contributions from five remaining hydrocarbons (DME, CH_4, C_2H_4, C_2H_6, and CH_3). Therefore, information accessible from the experiment reduces to only eleven species. Accordingly, the 'experimental' effective Rayleigh cross section is composed only by eleven species and can be described as

$$\begin{aligned}\sigma_{\mathrm{Ray,eff,exp}} &= \frac{\sum_{i=1}^{6} X_i(T,a)\sigma_{\mathrm{Ray},i} + \sum_{i=7}^{11} X_i(T,a)\sigma_{\mathrm{Ray,HC}}}{\sum_{i=1}^{11} X_i(T,a)} && \text{(4.15a)}\\ &= \frac{\sum_{i=1}^{6} X_i(T,a)\sigma_{\mathrm{Ray},i} + X_{\mathrm{HC}}(T,a)\sigma_{\mathrm{Ray,HC}}}{\sum_{i=1}^{6} X_i(T,a) + X_{\mathrm{HC}}(T,a)} \,. && \text{(4.15b)}\end{aligned}$$

In Eq. (4.15b) contributions from the six major non-hydrocarbon species and the five hydrocarbon species (excluding C_2H_2 and CH_2O) are grouped in two terms, $\sum_{i=1}^{6} X_i(T,a)\sigma_{\mathrm{Ray},i}$ and $X_{\mathrm{HC}}(T,a)\sigma_{\mathrm{Ray,HC}}$. In the latter, instead of the species-specific Rayleigh cross sections an effective, mole-weighted cross section $\sigma_{\mathrm{Ray,HC}}$ is used for the hydrocarbons. Because mole fractions of the five hydrocarbon species remain unknown from the experiment, a model has to be implemented providing a sound estimation of the hydrocarbon contribution to the Rayleigh scattering signal, $\sum_{i=7}^{11} X_i(T,a)\sigma_{\mathrm{Ray,HC}} = X_{\mathrm{HC}}(T,a)\sigma_{\mathrm{Ray,HC}}$. Prior to introducing the model for this term, the temperature dependent deviation between Eq. (4.14) and (4.15b) is considered with the Rayleigh cross section of DME being used for all five in Eq. (4.15b), i.e. $\sigma_{\mathrm{Ray,HC}} = \sigma_{\mathrm{Ray,DME}}$. This is effectively what is assumed in Raman/Rayleigh processing measurements from methane flames, where the Rayleigh cross section for CH_4 is applied to all molecules contributing to the fuel Raman channel, without causing significant error.

Figure 4.7 provides temperature dependent effective cross sections normalized to nitrogen. Results for $\sigma_{\mathrm{Ray,eff,ref}}$ and $\sigma_{\mathrm{Ray,eff,exp}}$ (assuming $\sigma_{\mathrm{Ray,HC}} = \sigma_{\mathrm{Ray,DME}}$) are shown for both transport models and various strain rates. The deviations of $\sigma_{\mathrm{Ray,eff,exp}}$ are quantified by the ratio $\sigma_{\mathrm{Ray,eff,exp}}/\sigma_{\mathrm{Ray,eff,ref}}$. With rising temperature in DME flames the true value of $\sigma_{\mathrm{Ray,HC}}$ becomes significantly smaller than $\sigma_{\mathrm{Ray,DME}}$ due to the build-up of the intermediate hydrocarbons that exhibit smaller Rayleigh cross sections. Significant differences between

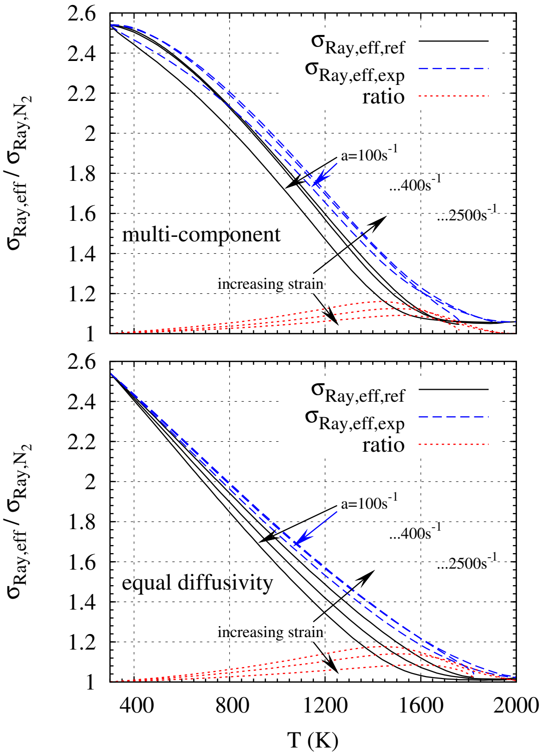

Figure 4.7: Effective Rayleigh cross section for T2 configuration (19.7 % DME) from laminar flame calculation in Tsuji geometry, mechanism from Zhao et al., using (top) multi-component and thermal diffusivity transport and (bottom) equal diffusivity. Solid lines show the cross sections for different strain rates including the thirteen most relevant species deduced from Eq. (4.14). Dashed lines are derived following Eq. (4.15b), where $\sigma_{\mathrm{Ray,HC}} = \sigma_{\mathrm{Ray,DME}}$ is assumed for the five hydrocarbons. Dotted lines show the ratio $\sigma_{\mathrm{Ray,eff,exp}}/\sigma_{\mathrm{Ray,eff,ref}}$.

$\sigma_{\mathrm{Ray,eff,exp}}$ and $\sigma_{\mathrm{Ray,eff,ref}}$ are observed. These differences would translate directly to systematic error in temperature measured in fuel rich conditions. For the lowest strain rate $a = 100\,\mathrm{s}^{-1}$ the maximum of $\sigma_{\mathrm{Ray,eff,exp}}/\sigma_{\mathrm{Ray,eff,ref}}$ around 1435 K is slightly larger for equal diffusivity (18 %) than for the multi-component transport model (16 %). Independent of the transport model the ratio decreases with increasing strain rates due to diminishing of variation in $\sigma_{\mathrm{Ray,eff,exp}}$ for rising strain.

4.3.5 Temperature and strain rate dependent Rayleigh cross section model

In order to avoid the unacceptably large systematic errors illustrated by Fig. 4.7, a model must be used to account for species specific Rayleigh cross sections of the important hydrocarbon intermediates that contribute signal to the Raman fuel channel. The following expression follows straightforwardly from Eqs. (4.14) and (4.15b) and is used to represent the weighted Rayleigh cross section for hydrocarbons as it depends on temperature and strain rate, based on laminar flame calculations.

$$\sigma_{\mathrm{Ray,HC}}(T,a) = \frac{\sigma_{\mathrm{Ray,eff,ref}} \sum_{i=1}^{11} X_i(T,a) - \sum_{i=1}^{6} X_i(T,a)\sigma_{\mathrm{Ray},i}}{\sum_{i=7}^{11} X_i(T,a)} \tag{4.16}$$

This equation is inserted in Eq. (4.15b), which is used within the iterative Raman/Rayleigh data evaluation. Based on the input of laminar flame calculations, by nature the model varies with strain, transport model etc. This dependence is shown in Fig. 4.8 for two different transport models at various strain rates. In addition the integrated mole fraction $\sum_{i=7}^{11} X_i(T,a) = X_{\mathrm{HC}}(T,a)$ is included to the figure. Whereas $\sigma_{\mathrm{Ray,HC}}$ shows a sensitivity with regard to strain and transport model, X_{HC} is much less dependent on strain. However, slight differences especially at low temperatures are observed between the two transport models. Significant values of X_{HC} are present throughout the whole temperature range underlying the important role of intermediate hydrocarbons in Raman and Rayleigh scattering. Considering the sensitivity on the strain rate, deviations for $a = 100\,\mathrm{s}^{-1}$ and $a = 2500\,\mathrm{s}^{-1}$, respectively, are up to +60 % relative to the result for $a = 100\,\mathrm{s}^{-1}$ at 1550 K. Differences resulting from the two transport models at equal strain rate are smaller. At 1300 K differences add up to 8 % but increase for temperatures above 1700 K. Increased sensitivity of the model at these high temperatures is of minor influence because of the relatively low value of X_{HC}. The impact of the sensitivity of $\sigma_{\mathrm{Ray,HC}}$ upon $\sigma_{\mathrm{Ray,eff,exp}}$ calculated from Eq. (4.15b) is now evaluated by using the following expression:

$$\Delta\sigma_{\mathrm{Ray,eff}} = \frac{\sigma_{\mathrm{Ray,eff,ref}} - \sigma_{\mathrm{Ray,eff,exp}}\left(\sigma_{\mathrm{Ray,HC,a=400\,s^{-1}}}\right)}{\sigma_{\mathrm{Ray,eff,ref}}} \cdot 100\,\% \,. \tag{4.17}$$

Results shown in Fig. 4.9 are based on the effective cross section of hydrocarbons, $\sigma_{\mathrm{Ray,HC}}$, calculated with an intermediate strain rate of $a = 400\,\mathrm{s}^{-1}$ and equal diffusivity. For the

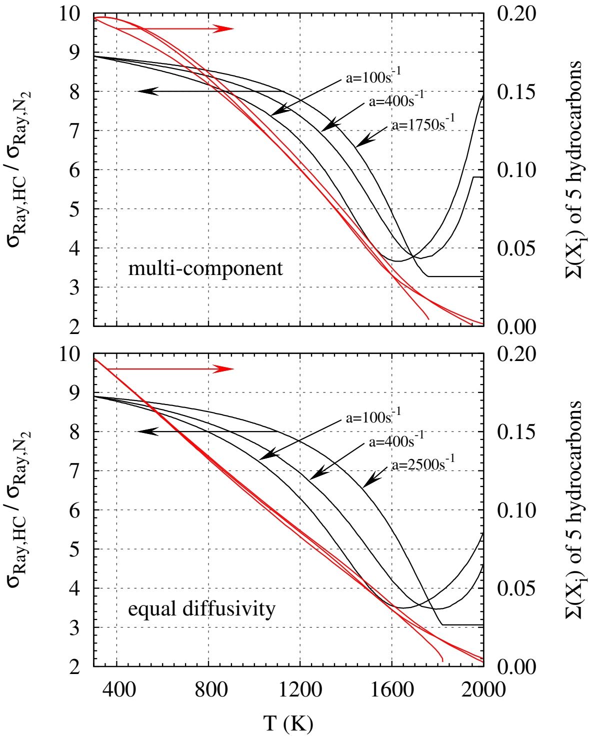

Figure 4.8: Effective Rayleigh cross section of the combined hydrocarbons DME, CH_4, C_2H_4, C_2H_6, and CH_3, based on mole fractions from laminar calculations for the two transport models and the T2 boundary conditions (same calculations as in Fig. 4.7).

reference effective cross section, $\sigma_{\text{Ray,eff,ref}}$, strain and transport model are varied. For equal diffusivities deviations sum up to ±4.5 % at 1400 K. For multi-component transport models $\Delta\sigma_{\text{Ray,eff}}$ is reduced to approximately 2.5 % using the identical strain rate of $a = 400\,\text{s}^{-1}$. In case of turbulent flames with varying strain inaccuracies will depend on instantaneous flow properties and can be as high as 4.5 %. Note that all these considerations affect the effective Rayleigh scattering cross section only. In the iterative Raman/Rayleigh data evaluation procedure these model-based inaccuracies do have a continuative impact because of the mutual interaction of temperature and mole fraction determination. Using one particular laminar flame calculation for both the Raman response and the Rayleigh cross section model, inaccuracies may partly compensate or amplify. In the end, final inaccuracies of the entire evaluation scheme can be assessed best by benchmarking measurements against laminar flame calculations. Another issue is how the time-average in physical space and the conditional average on mixture fraction in turbulent flames are affected. This will be discussed in Section 4.4.3 on the experimental results of T2 (compare Fig. 4.24).

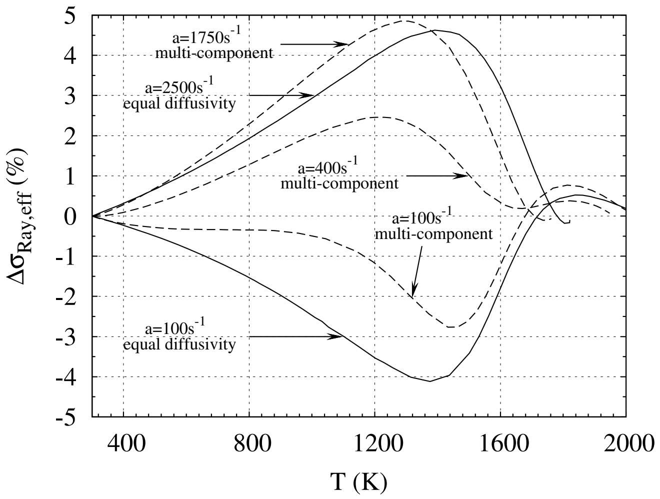

Figure 4.9: Emerging differences between effective Rayleigh cross sections using just one particular model ($a = 400\,\mathrm{s}^{-1}$, equal diffusivity) for distinct strain rates and transport.

4.3.6 Mixture fraction space, mass fractions, and atom ratios

The presence of intermediate hydrocarbon species in the DME flames impacts the calculation of mixture fraction. Thus in this section the determination of mixture fraction is examined, using laminar flame calculations as well as information about experimentally accessible data. The impact of detection issues regarding the hydrocarbons described in Sections 4.3.1-4.3.5 is discussed in the context of molar masses and atom numbers. The mixture fraction is calculated following the method of Barlow and Frank [9], where oxygen is excluded from the expression of Bilger et al. [18]:

$$F = \frac{2(Y_\mathrm{C} - Y_{\mathrm{C},2})/w_\mathrm{C} + (Y_\mathrm{H} - Y_{\mathrm{H},2})/2w_\mathrm{H}}{2(Y_{\mathrm{C},1} - Y_{\mathrm{C},2})/w_\mathrm{C} + (Y_{\mathrm{H},1} - Y_{\mathrm{H},2})/2w_\mathrm{H}} \,. \tag{4.18}$$

Herein Y_C, Y_H are local elemental mass fractions, w_C, w_H are atomic masses, and subscripts 1 and 2 refer to the inflow conditions of the main jet and co-flowing air, respectively. This expression has some advantage in partially premixed flames, where oxygen mass fraction boundary conditions are similar in the two streams, making the full Bilger expression more sensitive to experimental noise. Elemental mass fractions are derived from the species mass fractions $Y_{\mathrm{C}_x\mathrm{H}_y\mathrm{O}_z}$

$$Y_\mathrm{C} = w_\mathrm{C} \sum_i x_i \frac{(Y_{\mathrm{C}_x\mathrm{H}_y\mathrm{O}_z})_i}{(w_{\mathrm{C}_x\mathrm{H}_y\mathrm{O}_z})_i} \,, \tag{4.19}$$

$$Y_\mathrm{H} = w_\mathrm{H} \sum_i y_i \frac{(Y_{\mathrm{C}_x\mathrm{H}_y\mathrm{O}_z})_i}{(w_{\mathrm{C}_x\mathrm{H}_y\mathrm{O}_z})_i} \,, \tag{4.20}$$

where x, y and z refer to the corresponding number of C, H, O atoms and $w_{\mathrm{C}_x\mathrm{H}_y\mathrm{O}_z}$ to the respective molar mass of the species i. Raman measurements provide species concentrations $C_{\mathrm{C}_x\mathrm{H}_y\mathrm{O}_z}$. Species mass or mole fractions are derived via post-processing, using a molar mass weighted normalization or simple normalization, respectively:

$$Y_{\mathrm{C}_x\mathrm{H}_y\mathrm{O}_z} = \frac{C_{\mathrm{C}_x\mathrm{H}_y\mathrm{O}_z} w_{\mathrm{C}_x\mathrm{H}_y\mathrm{O}_z}}{\sum_i (C_{\mathrm{C}_x\mathrm{H}_y\mathrm{O}_z} w_{\mathrm{C}_x\mathrm{H}_y\mathrm{O}_z})_i} \,, \tag{4.21}$$

$$X_{\mathrm{C}_x\mathrm{H}_y\mathrm{O}_z} = \frac{C_{\mathrm{C}_x\mathrm{H}_y\mathrm{O}_z}}{\sum_i (C_{\mathrm{C}_x\mathrm{H}_y\mathrm{O}_z})_i} \,. \tag{4.22}$$

In practical Raman/Rayleigh measurements, hydrocarbon species are cumulated into the hydrocarbon channel. Thus, individual concentrations of fuel and intermediate hydrocarbons (HC) are summarized in

$$C_{\mathrm{HC}} = \sum_i (C_{\mathrm{C}_x\mathrm{H}_y\mathrm{O}_z})_i \,, \quad x \wedge y \neq 0 \,. \tag{4.23}$$

Accordingly, information on $C_{\mathrm{C}_x\mathrm{H}_y\mathrm{O}_z} w_{\mathrm{C}_x\mathrm{H}_y\mathrm{O}_z}$ for intermediate hydrocarbons necessary for calculation of Eq. (4.21) is not available from the measurements. In the present approach the molar mass of DME is used for representing all hydrocarbons cumulated into the Raman channel:

$$(w_{\mathrm{C}_x\mathrm{H}_y\mathrm{O}_z})_i = w_{\mathrm{DME}} \,, \quad x \wedge y \neq 0 \,. \tag{4.24}$$

This is a crude simplification. However, as will be shown, comparisons between experiments and calculations can still be made on a consistent basis, and an additional level of complexity is avoided in the implementation of the overall method of Raman/Rayleigh data analysis for DME flames. The assumption (4.24) causes significant deviations in calculated mass fractions and mixture fraction from normally defined values, so adapted mass and mixture fraction definitions are introduced and denoted by Y^* and F^*, respectively. The cumulated mass fractions of hydrocarbons and non-hydrocarbons read

$$Y^*_{\mathrm{HC}} = \frac{C_{\mathrm{HC}} w_{\mathrm{DME}}}{C_{\mathrm{HC}} w_{\mathrm{DME}} + \sum_i (C_i w_i)_{\mathrm{nonHC}}} \tag{4.25}$$

and

$$(Y^*_i)_{\mathrm{nonHC}} = \frac{(C_i w_i)_{\mathrm{nonHC}}}{C_{\mathrm{HC}} w_{\mathrm{DME}} + \sum_i (C_i w_i)_{\mathrm{nonHC}}} \,. \tag{4.26}$$

Note, that normalization in Eq. (4.25) and (4.26) affects mass fractions of all species. This is shown in Fig. 4.10.

To derive corresponding elemental mass fractions, Eq. (4.19) and (4.20) are split into two

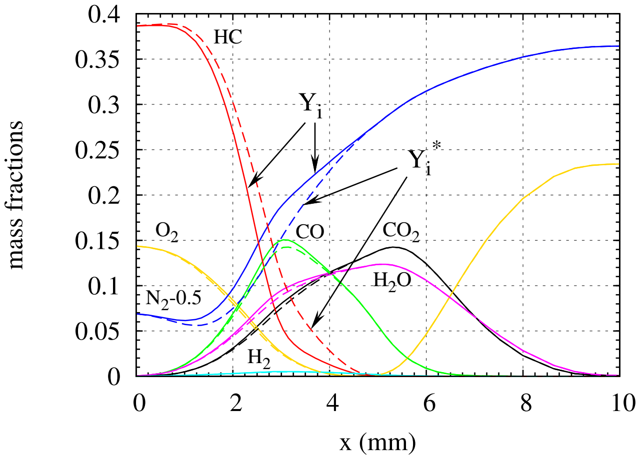

Figure 4.10: Effect on species mass fractions due to the approximation (4.24) of using the molar mass of DME for all hydrocarbons. This molar mass and the resulting mass fraction is generally too high: $Y^*_{\mathrm{HC}} \geq Y_{\mathrm{HC}}$. Thus, all other species mass fractions are too small due to the normalization: $(Y_i)^*_{\mathrm{nonHC}} \leq (Y_i)_{\mathrm{nonHC}}$. Based on a laminar calculation for L2 conditions, Tsuji geometry with $a = 50\,\mathrm{s}^{-1}$, Zhao mechanism, and multi-component.

terms

$$Y^*_{\mathrm{C}} = Y^*_{\mathrm{C}_{\mathrm{nonHC}}} + Y^*_{\mathrm{C}_{\mathrm{HC}}} \,, \tag{4.27}$$

$$Y^*_{\mathrm{H}} = Y^*_{\mathrm{H}_{\mathrm{nonHC}}} + Y^*_{\mathrm{H}_{\mathrm{HC}}} \,. \tag{4.28}$$

For species emerging from the reaction mechanism by Zhao et al. the non-hydrocarbon part is provided by

$$Y^*_{\mathrm{C}_{\mathrm{nonHC}}} = Y^*_{\mathrm{C}_{\mathrm{CO}_2}} + Y^*_{\mathrm{C}_{\mathrm{CO}}} \tag{4.29}$$

and

$$Y^*_{\mathrm{H}_{\mathrm{nonHC}}} = Y^*_{\mathrm{H}_{\mathrm{H}_2}} + Y^*_{\mathrm{H}_{\mathrm{H}_2\mathrm{O}}} + (Y^*_{\mathrm{H}_{\mathrm{OH}}} + Y^*_{\mathrm{H}_{\mathrm{H}}} + Y^*_{\mathrm{H}_{\mathrm{HO}_2}} + Y^*_{\mathrm{H}_{\mathrm{H}_2\mathrm{O}_2}}) \,. \tag{4.30}$$

Minor species contributions to $Y_{\mathrm{H}_{\mathrm{nonHC}}}$ are summarized in parentheses. Their total contribution is small as will be shown in Section 4.3.7 below, and they are neglected. The hydrocarbon part reads

$$Y^*_{\mathrm{C}_{\mathrm{HC}}} = 2Y^*_{\mathrm{HC}} w_{\mathrm{C}} / w_{\mathrm{DME}} \tag{4.31}$$

and

$$Y^*_{\mathrm{H}_{\mathrm{HC}}} = 6Y^*_{\mathrm{HC}} w_{\mathrm{H}} / w_{\mathrm{DME}} \,. \tag{4.32}$$

Consistent with Eq. (4.24) numbers of C and H atoms are those for DME. Accordingly, corresponding atom ratios are also affected and denoted by C*/H*, C*/O* and so forth. Species which contribute significantly in Eq. (4.25) to the cumulated mass fractions of hydrocarbons, Y^*_{HC}, within Raman measurements in DME/air flames are discussed below. Finally, the adapted mixture fraction F^* reads

$$F^* = \frac{2(Y^*_{\mathrm{C}} - Y_{\mathrm{C},2})/w_{\mathrm{C}} + (Y^*_{\mathrm{H}} - Y_{\mathrm{H},2})/2w_{\mathrm{H}}}{2(Y_{\mathrm{C},1} - Y_{\mathrm{C},2})/w_{\mathrm{C}} + (Y_{\mathrm{H},1} - Y_{\mathrm{H},2})/2w_{\mathrm{H}}}\,, \tag{4.33}$$

Clearly, the use of the adapted mass fractions Y^* and the corresponding F^* must be justified. First, this is the approach that is used in analyzing Raman/Rayleigh data from CH_4 flames, where hydrocarbon intermediates have a much smaller influence on results. Second, species mass fractions and mixture fraction are quantities derived only in the post-processing; they are not used within the iterative evaluation of Raman/Rayleigh data. Third, because of lack of knowledge of individual intermediate hydrocarbon species concentrations, simplifying assumptions must be made. In order to keep the approach as simple as possible, the assumption (4.24) for the molar mass and the assumptions in Eq. (4.31) and (4.32) for corresponding atom numbers are preferred to other conceivable approaches, such as taking the concentration-weighted molar masses from specific laminar flame calculations. Fourth, the differences $\Delta(F^* - F)$ seen below in Fig. 4.11 can be minimized by selecting an optimal number of intermediate hydrocarbon species within the entire evaluation procedure. This selection is presented in the next section. Finally, by applying the same method of post processing to both computational and experimental results, consistent quantitative comparisons can be carried out, as will be demonstrated in Section 4.4.3. Note that especially for comparison of species mass fractions this procedure is essential, as easily seen from the differences shown in Fig. 4.10.

4.3.7 Impact of intermediates on mixture fraction determination

Laminar flame results are now used to investigate the impact of different sets of hydrocarbon intermediates on the computed mixture fraction. Mixture fraction deviations are compared to a reference case, which is calculated from Eq. (4.18). Results are found similar for all laminar flame calculations used in this work and are presented for the Tsuji flame geometry using 28.1 % DME in air (L2 configuration), multi-component transport, and a strain rate of $a = 50\,\mathrm{s}^{-1}$. The reference case is listed as case 1 in Table 4.10. The case 'Bilger' in the second row refers to the original mixture fraction definition including oxygen [18] and all 55 chemical species in the Zhao mechanism. Cases 2a-f refer to the mixture fraction definition from Eq. (4.18), excluding oxygen and progressively omitting the less significant hydrocarbon species. Elemental mass fractions are calculated from Eq. (4.19) and (4.20) before insertion into Eq. (4.18). These cases 2 show the impact of particular species and from an experimental point of view they reflect a separate measurement of correct species mass fractions. A conclusion can be drawn regarding which species would be necessary to allow accurate mixture fraction measurements in DME/air flames.

1. Reference case using all 55 species mass fractions.
2. (a) 16 species mass fractions, Y_{CO_2}, Y_{O_2}, Y_{CO}, Y_{N_2}, Y_{H_2O}, Y_{H_2}, Y_{DME}, Y_{CH_4}, Y_{CH_2O}, $Y_{C_2H_2}$, $Y_{C_2H_4}$, $Y_{C_2H_6}$, Y_{CH_3}, Y_{OH}, Y_O, Y_H.
    (b) 13 species, omitting Y_{OH}, Y_O, Y_H in 2a.
    (c) 12 species, omitting Y_{CH_3} in 2b.
    (d) 11 species, omitting Y_{CH_2O}, $Y_{C_2H_2}$ in 2b.
    (e) 7 species, omitting Y_{CH_4}, $Y_{C_2H_4}$, $Y_{C_2H_6}$, Y_{CH_3} in 2d.
    (f) 7 species, same as 2e, but normalized to $\sum_{i=1}^{7} Y_i$.

Additionally, two cases 3a and 3b are defined to mimic the actual experimental condition where fuel and intermediate hydrocarbons are cumulated in a single detection channel. Both cases require simplifying assumptions regarding the molar masses and atom numbers of intermediate hydrocarbons corresponding to the assumptions leading to the adapted mixture fraction F^* given by Eq. (4.33). They are defined on the basis of mole fractions, which here is equivalent to the Raman-measured concentrations in Eq. (4.25) and (4.26).

3. (a) 6+(7) species, X_{CO_2}, X_{O_2}, X_{CO}, X_{N_2}, X_{H_2O}, X_{H_2}, (X_{DME}, X_{CH_4}, X_{CH_2O}, $X_{C_2H_2}$, $X_{C_2H_4}$, $X_{C_2H_6}$, X_{CH_3}).
    (b) 6+(5) species, as above but omitting X_{CH_2O}, $X_{C_2H_2}$.

Case 3b, containing 6 non-HC species and 5 HC species, corresponds to the selection of species already introduced in Sections 4.3.2.3 and 4.3.4 above. Elemental mass fractions, Eq. (4.27) and (4.28), were calculated from the species mass fractions, Eq. (4.25) and (4.26), using mole fractions X_i and employing the approximations (4.24), (4.31), and (4.32), which assign the molar mass and atom numbers of DME to all considered hydrocarbon intermediates. This simplification leads to differences between the corresponding cases 2b ↔ 3a and 2d ↔ 3b, despite of identical species considered.

Maximum differences of all cases relative to the reference case are summarized in Table 4.10 for selected measures as specified in the table caption. From cases 2 it turns out that the separate detection of twelve species of case 2c would suffice to allow mixture fraction and temperature measurements in the order of current measurement precisions. Further negligence of species leads to unacceptable distortions, i.e. for case 2e with just seven species of up to $\Delta F_{\max} = -0.2$ causing a $\Delta T_{\max} = -472\,\mathrm{K}$. Unacceptable distortions are also obtained for the cases 3a and 3b due to the loss of information on particular hydrocarbons.

Figure 4.11 shows distortions of the mixture fraction with respect to the reference case for the entire mixture fraction space. Note that mixture fraction $F_{\mathrm{all}} > 1$ is accessed.

Table 4.10: Maximum deviations in mixture fraction ΔF_{max} (column 3) and resulting deviations in temperature ΔT_{max} (column 5) for various cases relative to the reference case 1 as detailed in the text. Mixture fraction of reference case at respective maximum deviation ΔF_{max} (column 4) and ΔT_{max} (column 6) from all other cases, respectively. Columns 7, 8 provide the minimum of sums of mass and columns 9, 10 minimum of mole fractions within the entire mixture fraction space.

case	no. species	ΔF_{max}	F_{all} @ΔF_{max}	ΔT_{max} (K)	F_{all}, T @ΔT_{max}	min $(\sum_i Y_i)$ w Ar	min $(\sum_i Y_i)$ w/o Ar	min $(\sum_i X_i)$ w Ar	min $(\sum_i X_i)$ w/o Ar
1,Bilger w/o O	all(55)	-	-	-	-	1	0.987	1	0.991
Bilger	all[a]	-0.0056	0.238	20	0.145,478	1	0.987	1	0.991
2a	16	-0.0027	0.668	-6	0.608,1382	0.998	0.987	0.999	0.991
2b	13	-0.0032	0.251	11	0.289,1963	0.994	0.983	0.988	0.980
2c	12	-0.0034	0.638	11	0.289,1963	0.994	0.983	0.988	0.980
2d	11	-0.0569	0.699	-130	0.998,516	0.971	0.962	0.974	0.968
2e	7	-0.2097	0.668	-472	0.492,1854	0.935	0.926	0.920	0.914
2f	7norm	-0.1741	0.638	-394	0.611,1776	1[b]	1[b]	0.920	0.914
3a	6+(7)	0.0997	0.668	170	1.037,531	1[c]	1[c]	0.988	0.980
3b	6+(5)	0.0318	0.584	99	1.022,461	1[c]	1[c]	0.974	0.968

[a] using the definition by Bilger et al. [18].

[b] sum of mass fractions is that from 7, but renormalized.

[c] mass fractions are calculated based on mole fractions, this implicates renormalization.

This is a consequence of differential diffusion effects and is especially pronounced in the rich-premixed laminar configuration L1 (see Fig. 4.22). As expected, missing species in Eq. (4.18) cause the mixture fraction to go down. Deviations for 2e and 2f, using only 7 species, peak at -0.2 near $F_{\mathrm{all}} = 0.65$. The deviations are up to two orders of magnitude larger than in comparable flames of methane and extend over a wide range in fuel-rich conditions where significant intermediate hydrocarbons are present. Obviously, differences for all cases 2 decrease with increasing number of species considered. In case of 13 species (case 2b) the deviations are even below present experimental precision denoted by $\sigma_{\mathrm{F,exp}}$ (crosses in Fig. 4.11). This is still satisfied for the case of 12 species (2c) but is not shown. Cases 3a and 3b, which represent the actual experimental situation, exhibit deviations from F_{all} exceeding experimental uncertainties. In contrast to the cases 2, cases 3a and 3b show an overestimation of the mixture fraction and decreasing deviation with decreasing number of species considered. Closer agreement between F_{all} and $F^{*}_{6+(5)\mathrm{species}}$ is favourable and even provides a benefit of the exclusion of C_2H_2 and CH_2O from the processing of the Raman response.

A distortion of the mixture fraction coordinate impacts correspondingly the scalar profiles in mixture fraction space. This is shown for temperature in Fig. 4.12. The temperature of the reference case 1 is plotted versus its mixture fraction F_{all}. Cases 2d, 2e, 2f, 3a, and 3b are compared to the reference case. As mentioned already, apparent deviations ΔT are due to a distortion of the mixture fraction coordinate and can reach up to 500 K depending on case and mixture fraction. The case 3b selected in previous sections shows the smallest deviation.

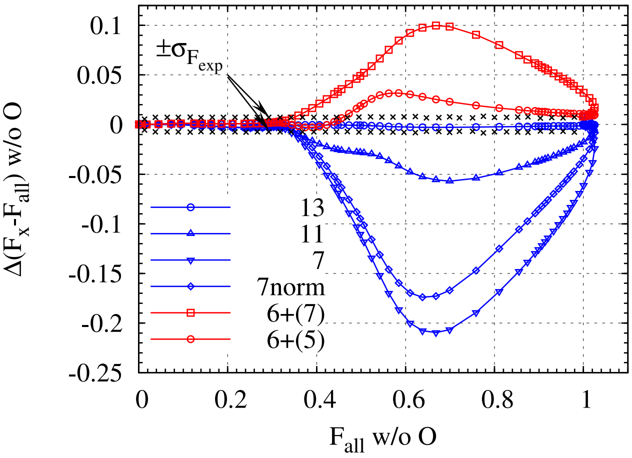

Figure 4.11: Deviation of mixture fraction for cases 2b, 2d, 2e, 2f, 3a, and 3b plotted vs. mixture fraction of the reference case. Crosses represent experimental precision of the mixture fraction in actual L2 experiments using on-chip binning.

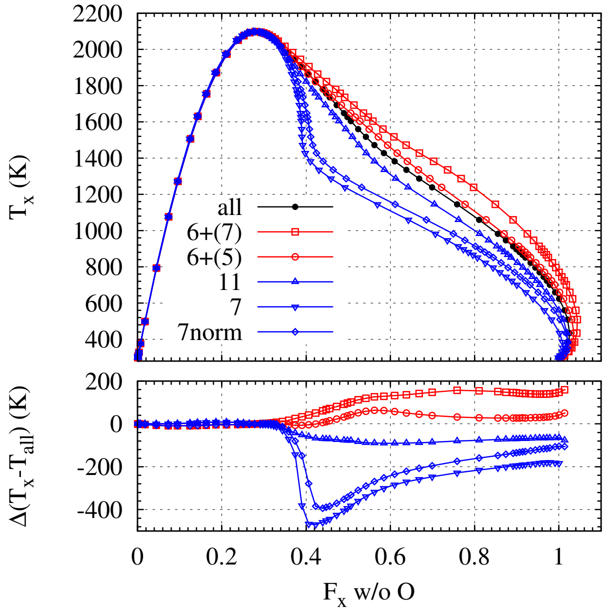

Figure 4.12: Impact of differences in the mixture fraction calculation on scalars, exemplified here for temperature. Closed circles denote the reference case 1 using Eq. (4.18) and including all species. Blue curves shifted to the left relative to the reference case show the influence of neglecting species in Eq. (4.18). Red curves represent the adapted mixture fraction calculation defined by Eq. (4.33).

4.3.8 Summary on sensitivity analysis of the mixture fraction calculation

The starting point for the sensitivity analysis was that Raman signals of intermediate hydrocarbons and fuel spectrally overlap and are cumulated into a single detection channel in the context of the matrix inversion method. Consequently, the local composition of intermediate hydrocarbons cannot be determined directly from the experiments. Thus, using laminar flame calculations two different approaches were conceived to judge on the importance of particular hydrocarbon intermediates regarding the calculation of the mixture fraction. First, contributions of twelve species mass fractions are found to impact the mixture fraction significantly. Second, hydrocarbon mole fractions are summarized in X_{HC}, reflecting the actual experimental conditions. Instead of species-specific molar masses and atom numbers those of DME were used for the following conversion from species mole fractions to mixture fraction. These assumptions distort the calculated mixture fraction. To account for the difference, the adapted mixture fraction F^* was introduced. In consistence with conclusions from Sections 4.3.2.3 and 4.3.4, a case of 6+(5) species (CO_2, O_2, CO, N_2, H_2O, H_2) + (DME, CH_4, C_2H_4, C_2H_6, and CH_3) was investigated and found to yield smaller deviations in mixture fraction $\Delta(F_{\mathrm{all}} - F^*_{6+(5)\mathrm{species}})$ than the case including all significant hydrocarbons. However, remaining differences are still too high to be ignored. Therefore, all plots in mixture fraction space shown in Section 4.4 are based on $F^* = F^*_{6+(5)\mathrm{species}}$ rather than F_{all}. This adapted mixture fraction is proposed as an appropriate basis for comparison of Raman/Rayleigh measurements with both laminar calculations and turbulent combustion modeling results. That is, mixture fraction should be calculated from the modeled species results using the adapted F^* definition before comparison with experimental results in mixture fraction space.

4.4 Results

This part is composed of three sections. Section 4.4.1 provides the temperature dependent Raman response and crosstalk curves essential for the data evaluation. In Section 4.4.2 important corrections of broadband and C_2-LIF interferences are discussed. Finally, Section 4.4.3 shows results of laminar and turbulent DME/air flames for the mixture compositions provided in Section 4.2.2.

4.4.1 Hydrocarbon Raman response and crosstalk curves

In conclusions from Section 4.3 the Raman scattering from DME/air flames detected on the seven species-channels is treated as being composed of 6+(5) species. The signal of the hydrocarbon channel is composed of contributions from DME, CH_4, C_2H_4, C_2H_6, and CH_3. This is labeled DME+4HCs in the following.

Calculation of temperature-dependent rovibrational Raman spectra of hydrocarbon species such as DME, CH_4, C_2H_4, or C_2H_6, from first principles is not available or not sufficiently accurate to replace calibration measurements. For this reason relative Raman intensities within the hydrocarbon channel are extracted from Raman measurements in electrically heated gas mixtures. The temperature accessed is limited to the range between 295 K and 820 K. For temperatures exceeding 820 K relative Raman intensities are extrapolated linearly to 2500 K. Four different mixtures of 9 % hydrocarbon in nitrogen, DME/N_2, CH_4/N_2, C_2H_4/N_2, C_2H_6/N_2, were investigated and Raman intensities were measured for the entire spectral range (720-4600 cm^{-1}) that is monitored in the experiment. Contributions from individual hydrocarbon species onto the hydrocarbon channel and all other species channels (crosstalk) were thereby quantified.

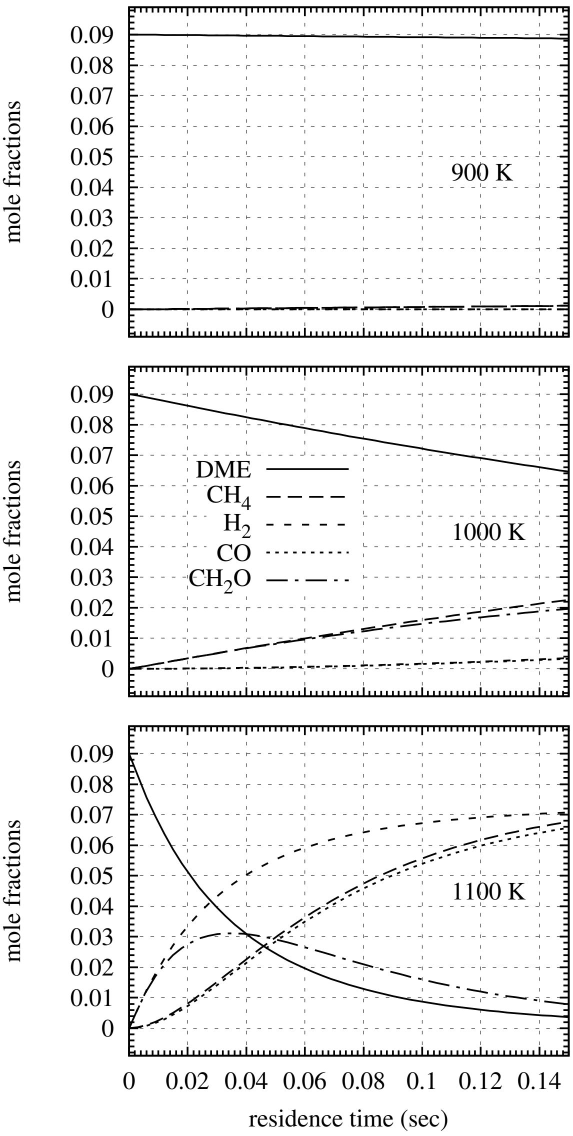

Figure 4.13: Computation of thermal decomposition of DME in a flow plug reactor conducted by Chen [29].

To assess the possibility of thermal decomposition of DME in the heating process a computation of pyrolysis of the same DME/N_2 mixture was conducted by Chen [29] using the plug flow reactor code by Lutz et al. [66]. Results for the three highest temperatures are shown in Fig. 4.13. For experimental-like residence times of mostly 0.15 s pyrolysis is just starting at 900 K (loss in $X_{\mathrm{DME}} < 0.001$). To further ensure that no pyrolysis locally occured near the heating elements, the Raman channels of two products of the pyrolysis, CO and H_2, were carefully monitored where no evidence of pyrolysis was found either. However, small parts of methane and formaldehyde cannot be distinguished from DME in the Raman spectrum due to spectral overlap. Hence, a small uncertainty of approximately 2 % in the measured Raman intensity from DME at 820 K is left.

For all strips the relative intensity from CH_3 is treated as one quarter of the CH_4 response ($0.25\times S_{\mathrm{Ram,CH_4}}$) following the findings in Hädrich et al. [47]. In contrast to the response curves shown in Fig. 4.6, linear extrapolation of Raman responses and an accounting for the effect of optical bowing [41], illustrated in Fig. 4.5, are applied for each species before summing up the hydrocarbon contributions to the final response curves using Eq. (4.3). Apart from the bowing effect, the resulting difference between the curves in Fig. 4.6 (based on constant integrated Raman signal ratios) and those computed here using elaborated temperature dependencies for each species, is rather small ($< 5\,\%$, maximum at 1400 K). This small difference is a good indication of the hydrocarbon response curve being dominated by the mixing process of species and not by unknown Raman intensities at higher temperatures. Especially for temperatures above 1400 K, the relative importance of this response curve is attenuated due to upcoming LIF-interferences. The amount of hydrocarbons, which are finally measured, is then dominated by the accuracy of the LIF-interference correction. Starting with the reference strip 37 (bowing center), Fig. 4.14 shows the Raman response curve for the hydrocarbon channel DME+4HCs and the most important crosstalk curves, CO_2←DME+4HCs, O_2←DME+4HCs, and F560←DME+4HCs, derived using on-chip binning. Smaller crosstalk contributions from N_2←DME+4HCs and CO←DME+4HCs were found at low temperatures and were corrected without temperature dependence. Other hydrocarbon-specific crosstalk curves are of less importance and taken from previous methane-air flame investigations (see Appendix A). Note that for CO_2←DME+4HCs and O_2←DME+4HCs two sets of curves are shown. The upper ones were adjusted for temperature exceeding 820 K and account for possible errors introduced by the extrapolation of the crosstalk-response to higher temperatures, additional broadband interferences, that are missed in the F560-channel (see next section), or differences between the species composition of the underlying 1D-calculation and those from the measured jet flame. These corrections are justified by better matching experimental results with laminar flame calculations as shown in Appendix B. The high importance of these crosstalks is demonstrated in Fig. 4.18. For example at the fuel-rich side of the flame the crosstalk from DME on O_2 is as high as the signal from O_2 itself.

The spectrometer dispersing the Raman bands has a short focal length, which leads to optical bowing of the image of the entrance slit and laser beam as shown in Chapter 3. In consequence Raman bands shift relative to rectangular regions of hardware binning (see Fig. 4.5) causing space-dependent variations in all response and crosstalk curves $c_{ij}(T)$

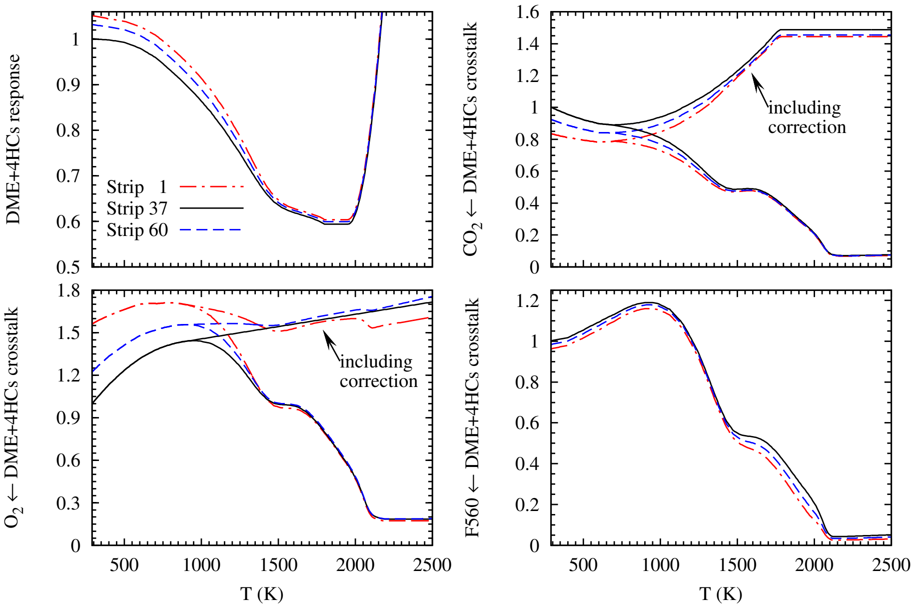

Figure 4.14: Response and crosstalk curves from measuring electrically heated gas mixtures of N_2/DME, N_2/CH_4, N_2/C_2H_4, N_2/C_2H_6 and using Eq. (4.3) in connection with laminar flame calculation for L2 configuration, multi-component transport, $a = 50\,\mathrm{s}^{-1}$. For the centrally located strip 37, curves are derived from hardware-binned data. All other strips are corrected for bowing effects relative to strip 37 using spectrally resolved data.

in Eq. (2.96). Whereas for diatomic species, CO_2, and H_2O, these bowing effects can be accounted for by calculations, hydrocarbon species still must be treated empirically. First, the effect of optical bowing is separated from the response and crosstalk characteristics. This is expressed by the entrywise product

$$[c_{ij}(T)]_k = [c_{ij}(T)]_{37}^{\mathrm{hardware-binned}} \circ [(f_{\mathrm{bowing}})_{ij}(T)]_k^{\mathrm{software-binned}} \,, \tag{4.34}$$

where the index k embraces all strip numbers from 1 to 60. In order to take advantage of lower readout noise from hardware-binned data the temperature dependence of curve p_{ij} is determined from measured Raman intensities from hardware-binned data at the bowing center on strip 37. The same measurements on strip 37 from spectrally resolved data are used to determine the strip-dependent variations in the measured Raman intensities for the corresponding shift on strip k. The resulting correction functions f_{bowing} were already implied in Fig. 4.14 and are shown explicitly in Fig. 4.15.

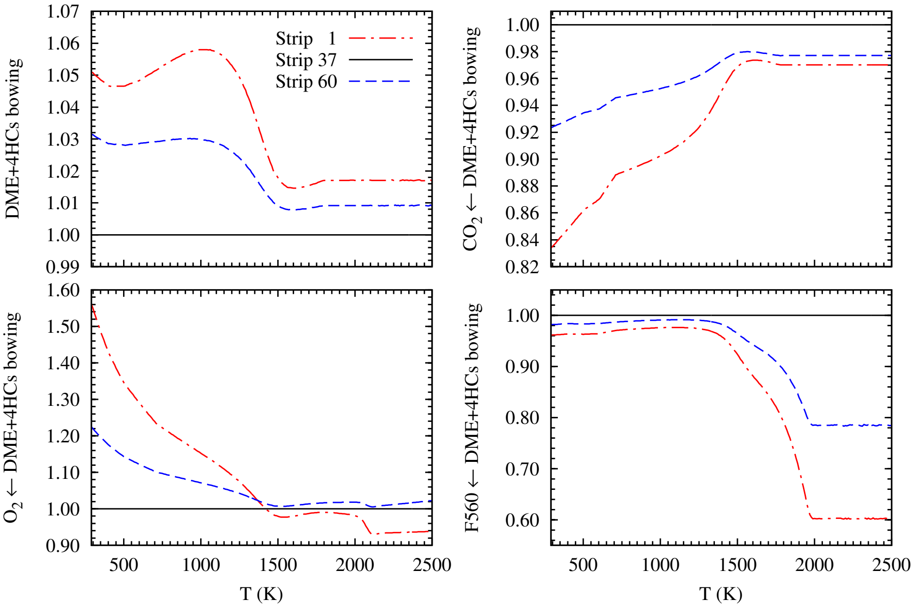

Figure 4.15: Bowing correction vs. temperature of DME+4HCs response and its crosstalks relative to the center strip 37.

4.4.2 Broadband and C_2 interferences

A spectrally flat background was determined around 4300 cm^{-1} (b3) and was subtracted from all Raman channels. In addition, at rich mixture composition in hydrocarbon-air flames, a variety of intermediate species and diatomic C_2 are formed. These intermediate species are excited by 532-nm radiation and give rise to fluorescence signals interfering with rovibrational Raman bands and rotational H_2 Raman lines. These interferences are monitored by an additional channel located near 560 nm (F560 channel spanning from ∼730 to 1100 cm^{-1} in the Raman spectrum). Temperature and bowing dependencies of the corresponding crosstalks were treated empirically.

First, to demonstrate the significance of the LIF interferences, Fig. 4.16 shows the temperature dependent signal cumulated in the F560 channel for both laminar and turbulent flames. These interferences impact the Raman responses over a wide temperature range above 1000 K with a peak between 1600 and 1700 K dependent on the mixture composition. Small scatter for the laminar cases are self-evident, but the large scatter in both turbulent cases with a wide spread of interfering signal intensities for temperatures above 1000 K indicates intense turbulence-chemistry interactions. For comparison, a laminar jet with a mixture of 25/75 vol% methane/air has a count level of 340 and a mixture of 44/66 vol% methane/air a level of 1000 (not shown). This is slightly smaller than in corresponding DME/air mixtures, but still very close and one of the main reasons DME is considered a relatively Raman-friendly hydrocarbon fuel. However, the crosstalk of LIF interferences

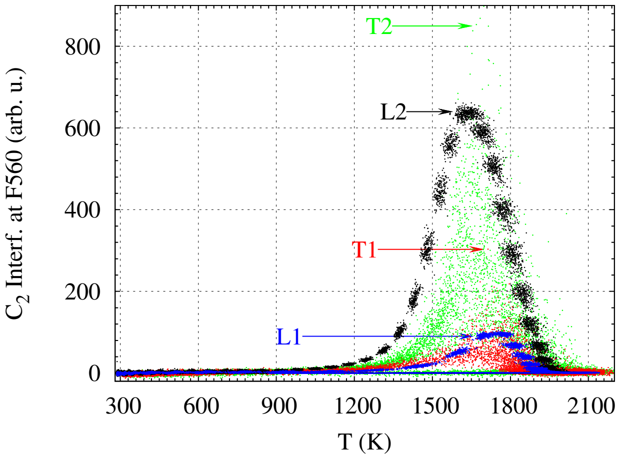

Figure 4.16: LIF signal cumulated in the F560 channel from mostly diatomic C_2 following excitation at 532 nm in different laminar and turbulent DME/air flames.

at temperatures exceeding 1000 K is significant and must be accounted for. The peak is located near 1650 K. The highest signals are found in the turbulent T2 case of up to 900, where on average the mixture composition of 28.1 %DME in air (L2 configuration) generates the highest LIF interference signals of about 650 at the F560 channel. This signal intensity corresponds to 31.000 photoelectrons e- ($\sigma_{\text{shot-noise}} = 176\,\text{e}-$ or 0.6 %). The crosstalk onto the N_2 channel for these specific conditions contributes by approximately 3450 e−, which corresponds to almost half of the total intensity of 7000 e−. The dependence of F560 response on temperature and the associated important crosstalk curves are plotted in Fig. 4.17 for central strip 37 and the most exterior strips 1 and 60, respectively. The bowing effect at the F560 response crosstalk curve is accounted for by using a similar approach as described in Section 4.4.1. Temperature dependencies for particular channels were derived from comparison with laminar calculations in physical, temperature, and mixture fraction space. To provide reasonable agreement of the same measurements at inner and outer strips, linearly increasing (O_2, CO) or decreasing (N_2) bowing corrections were introduced. Neither temperature- nor strip-dependence was found for H_2 at all.

Based on the temperature dependent Raman responses and crosstalk curves from Figs. 4.17 and 4.18 provide a survey of the relative crosstalk contributions (from 100-shot average at most interesting position in the L2 flame, centered at $r = 4.5$ mm) for selected channels in physical space marks, with nonlinearly mapped temperature and mixture fraction coordinates also displayed. Examining the L2 configuration at the maximum signal level in the F560 channel, the crosstalk contributions from various species compared to the Raman signal from the corresponding molecule are: 1) at the N_2 channel 100 %, 2) 30 % at the CO_2 channel, 3) 300 % at the CO channel, 4) 400 % at the DME channel, 5) 35 % at the H_2O channel, and 6) 100 % at the H_2 channel. Around 1850 K almost no oxygen is left and the crosstalk dominates completely. Since the crosstalk impact of the LIF interferences

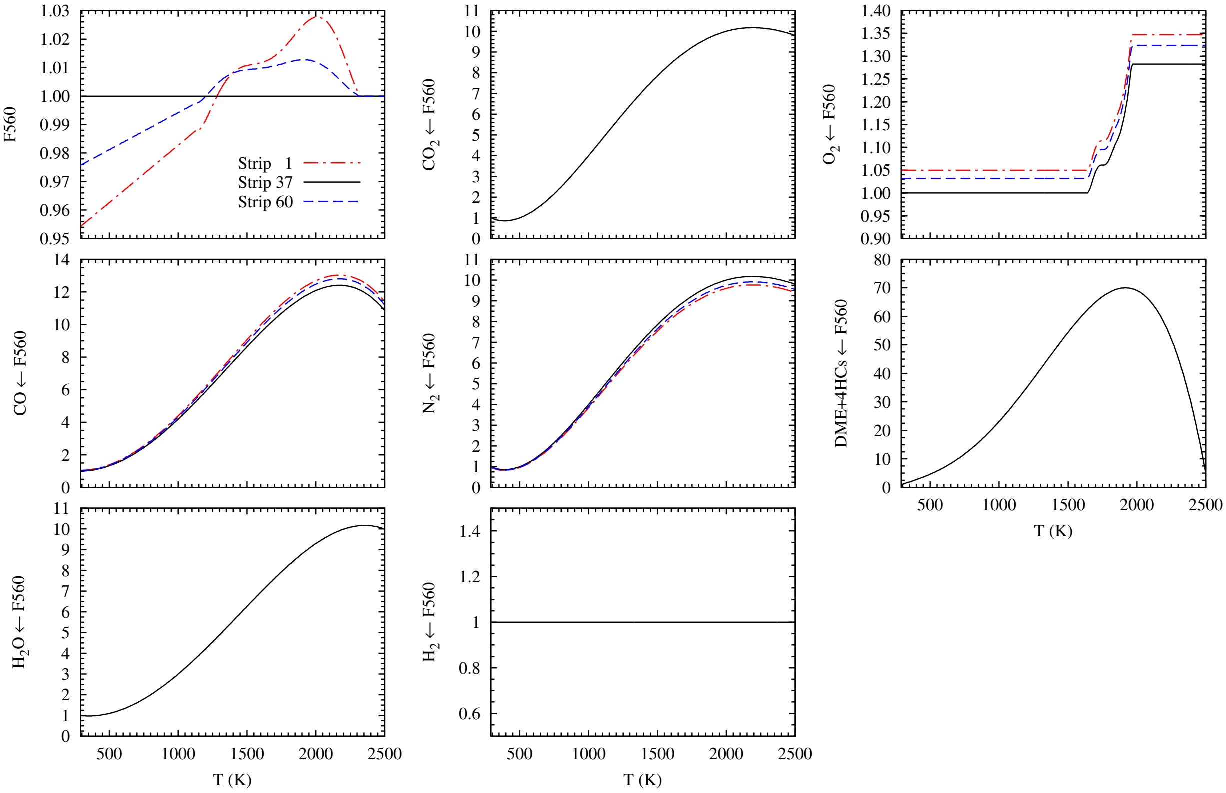

Figure 4.17: Top left: Temperature dependent response curve at the F560 channel caused by diatomic C_2 and other unspecified species LIF interferences. All other graphs: Corresponding crosstalk curves accounting for the impact of LIF interference on the respective Raman channel.

decreases with decreasing fractions of DME in air (see Fig. 4.16), just small deviations from a linear dependence on the signal measured at F560 is found between the L1 and L2 cases. Hence, a correspondingly smaller crosstalk is observed in the L1 case (11.4 % DME in air) at the thermo-chemical state with highest F560 impact. The CO channel is influenced by 50 % LIF interferences or the DME+4HCs channel by up to 40 %.

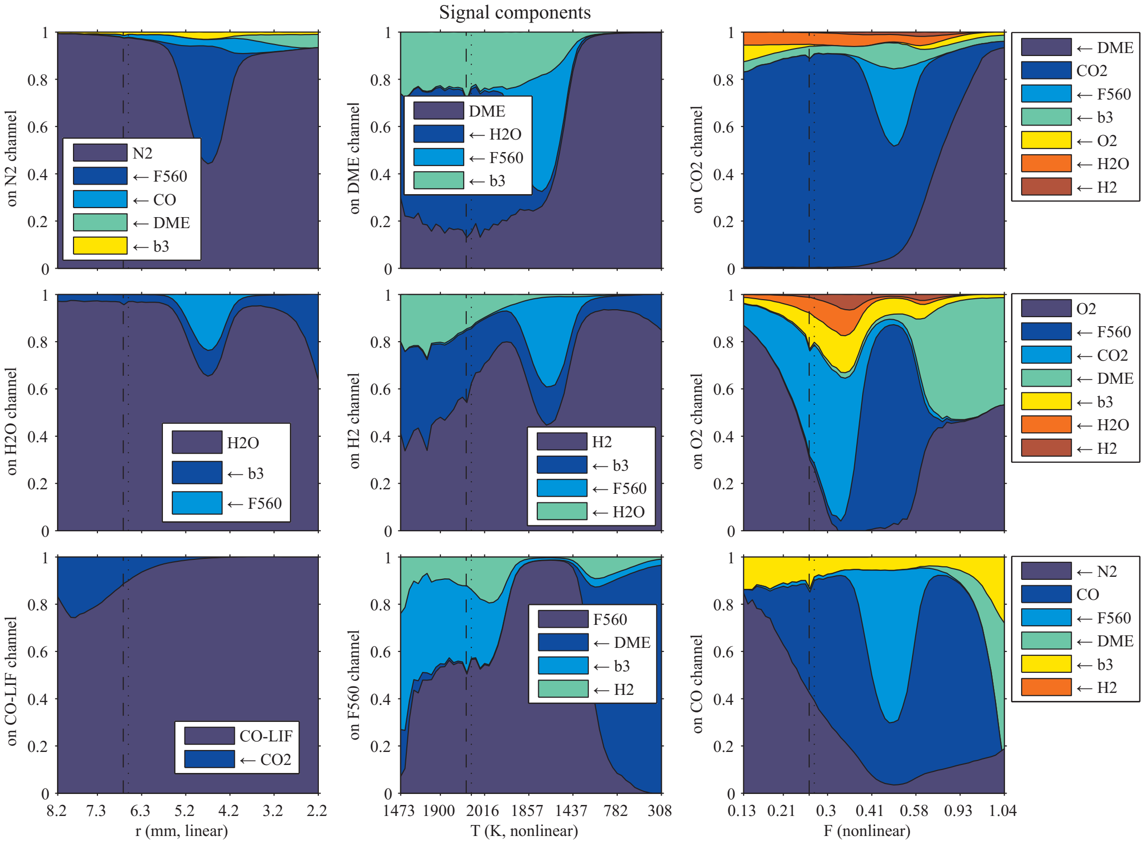

Figure 4.18: Variation of signal components on selected Raman channels illustrated in physical space and with nonlinearly mapped coordinates of temperature and mixture fraction for the L2 mixture composition. Colors and names in legends are chosen in descending order depending on the corresponding amount of signal for each subplot. The three different abscissa labels apply for the corresponding tick marks in all nine subplots. Vertical dotted lines mark the point of maximum temperature (2028 K). Dashed lines mark the stoichiometric mixture fraction ($F_{\mathrm{st}} = 0.26$). Note that crosstalk contributions are provided relative to the respective species response (all contributions normalized to 1; no absolute signal intensities are provided).

4.4.3 Results of laminar and turbulent DME/air flame measurements

The entire procedure discussed so far is now shown in its application by evaluating spatially resolved 1D Raman/Rayleigh data collected from the two laminar (L1, L2) and two turbulent DME/air flames (T1, T2) at mixture compositions given in Tables 4.2 and 4.3. Overall good agreement and remaining deviations between measurements and laminar calculations are discussed below.

Laminar results L2

Figure 4.19 shows results for the case L2 in physical space. The radial profile spans 13.5 mm and is composed of three line-imaged Raman/Rayleigh/CO-LIF measurement positions $r = 0, 4.5, 7.5\,\mathrm{mm}$ resulting in 1.5 and 3 mm spatial overlap between adjacent probe volume locations. Generally, 100 shots were recorded at each position, at the most interesting position $r = 4.5\,\mathrm{mm}$ two sets of 100 shots were taken. For comparison in physical space the laminar calculation at strain rate $a = 50\,\mathrm{s}^{-1}$ (multi-component transport) yields best agreement in the width of the measured temperature profiles.

Overall the agreement between laminar flame calculations and experimental data using the post-processing discussed above is very good. This holds true as well for the hydrocarbons at the DME+4HCs channel. The measured peak temperature is lower than the computed peak by 60 K. About 45 K are caused by negligence of radiation in the simulations, another 10 K by not accounting for 35 % relative humidity (0.007 mole fractions) in the co-flowing air-stream apparent in the experiments, and a mismatch of 10 K at the inflow boundaries (290 K measured but 300 K in the calculation), which is equivalent to ∼5 K in T_{max}. Deviations in gradients at the rich side, particularly in the temperature, O_2, DME+4HCs, or H_2O profiles apparent at $r = 0 - 2\,\mathrm{mm}$ are due to specifics of the calculation in Tsuji geometry, which are not precisely comparable to those present in the jet flame. Deviations at the right lean boundary, i.e. N/O^* profile, are partly attributed to the missing water in the calculation.

Maximum interferences measured on the F560 channel are at $r = 4.75\,\mathrm{mm}$, and interference on the Raman channels is generally well compensated for in the resulting species mole fractions. Slight deviations at the overlapping positions between the data from the three different measurement locations occur. This is attributed to variations in the index of refraction field causing different out-of-focus effects at both ends of the line segment at different positions. This effect was accounted for in the throughput-normalizations of DME, O_2 and N_2 by a linear correction of up to -1.2, +2.1, and +1.7 %, respectively. Mole fractions of CO and CO_2 as well as the C^*/H^* ratio are generally higher in the experiment. A similar trend is observed in the L1 configuration as well (Figures 4.21 and 4.22), which may also be due to the use of 1D opposed flow calculations to approximate the scalar

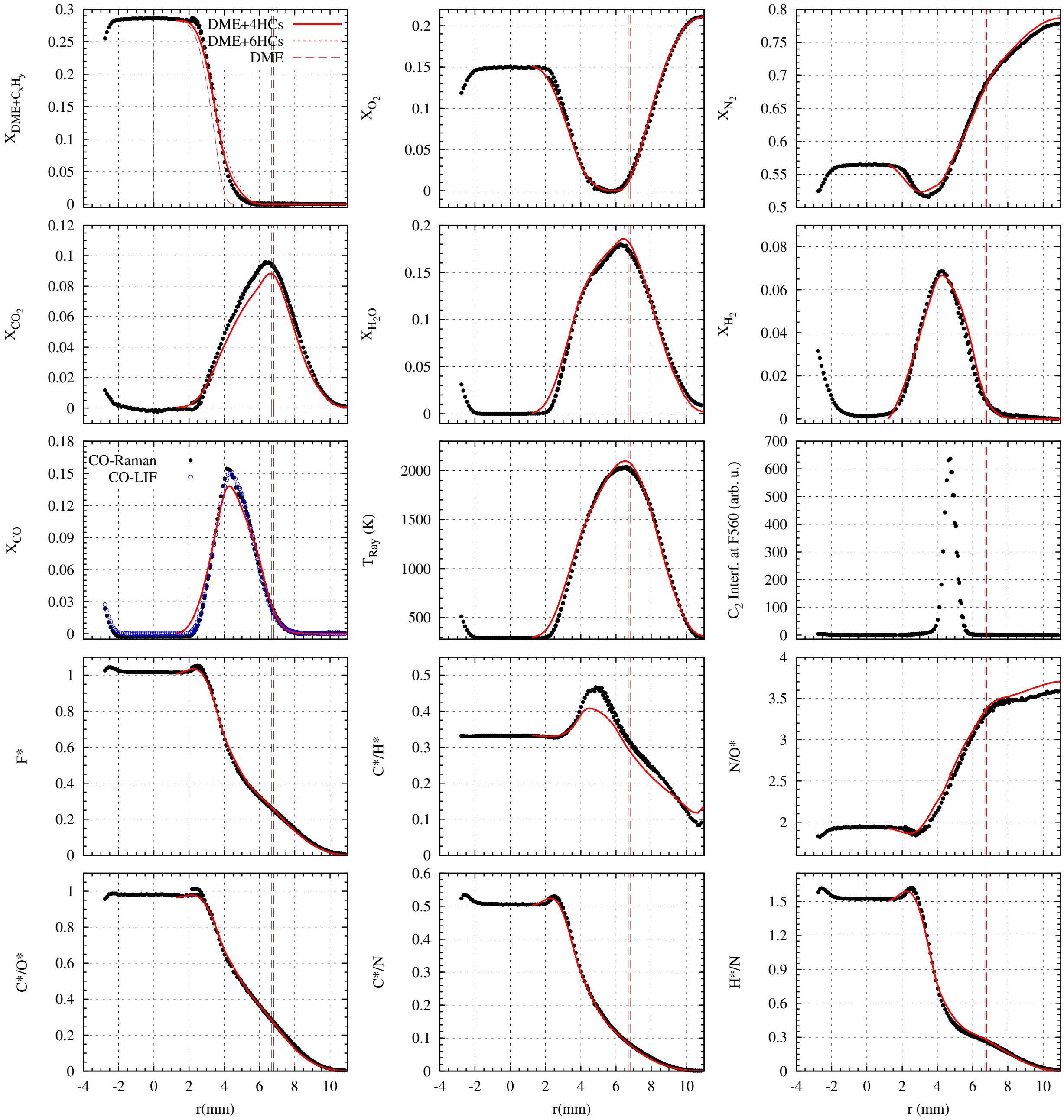

Figure 4.19: Temperature, species mole fractions, LIF interferences, adapted mixture fraction F^*, and atom ratios in physical space for the L2 mixture compositions. Results from simulations are shown by lines, experiments by closed circles and CO-LIF by open circles. The vertical dashed line marks the stoichiometric condition at $F^*_{st} = 0.26$.

structure of a 2D laminar jet flame.

Results from the same L2 measurements are shown in mixture fraction space F^* in Fig. 4.20, with the addition of temperature calculated from total number density and the measured laboratory pressure, the ratio of the two measured temperatures, and the differential diffusion parameter from Barlow et al. [10]. Here z^* adapted to F^*, such that

$$z^* = F^*_{\mathrm{H}} - F^*_{\mathrm{C}} \,, \tag{4.35}$$

where

$$F^*_{\mathrm{H}} = \frac{Y^*_{\mathrm{H}} - Y^*_{\mathrm{H},2}}{Y_{\mathrm{H},1} - Y_{\mathrm{H},2}} \text{ and } F^*_{\mathrm{C}} = \frac{Y^*_{\mathrm{C}} - Y^*_{\mathrm{C},2}}{Y_{\mathrm{C},1} - Y_{\mathrm{C},2}} \tag{4.36}$$

are local elemental mixture fractions based on hydrogen and carbon and subscripts 1 and 2 refer to the inflow conditions of the main jet and co-flowing air stream, respectively. Due to the large amount of molecular hydrogen (twice that in methane/air flames), differential molecular diffusion is prominent in DME/air flames.

Conditional average values are very close to the prediction by the laminar calculation assuming the detection of five hydrocarbon species. This provides additional confidence in the applied Rayleigh cross section model as well as the correctness of the temperature dependence of all Raman response- and crosstalk-curves. Note that conditional averages are omitted for values of F^* greater than unity, which result from strong differential diffusion effects in these laminar DME/air flames. Good agreement in the profile of the molecular diffusion parameter z^* is observed over the entire mixture fraction space, but under predicted significantly between $F^* = 0.4$ and 0.6, which is consistent with the deviation in the $\mathrm{C}^*/\mathrm{H}^*$ ratio.

All plots include simulated profiles for 6+(7) species (blue line), including C_2H_2 and CH_2O and using the corresponding F^* for 6+(7) species following the procedure in Section 4.3.7. However, better matching is obtained with the profiles comprising 6+(5) species. The mismatch of the simulation considering 6+(7) species exemplifies the concentration difference due to the additional contributions from C_2H_2 and CH_2O.

LIF interferences in the L2 flame are most prominent for mixture fractions in the range of $0.4 < F^* < 0.6$. Large scatter is observed in this range, especially for O_2, and is attributed to inherent photon shot-noise of the $O_2 \leftarrow$F560 crosstalk. Obviously, all atom ratios shown in the bottom line are less sensitive to any of the differences described above. Nearly perfect agreement between calculation and experiment is observed. The impact of the corrections of the crosstalk functions $CO_2 \leftarrow$DME+4HCs and $O_2 \leftarrow$DME+4HCs described in Section 4.4.1 was investigated and is discussed in the Appendix B.

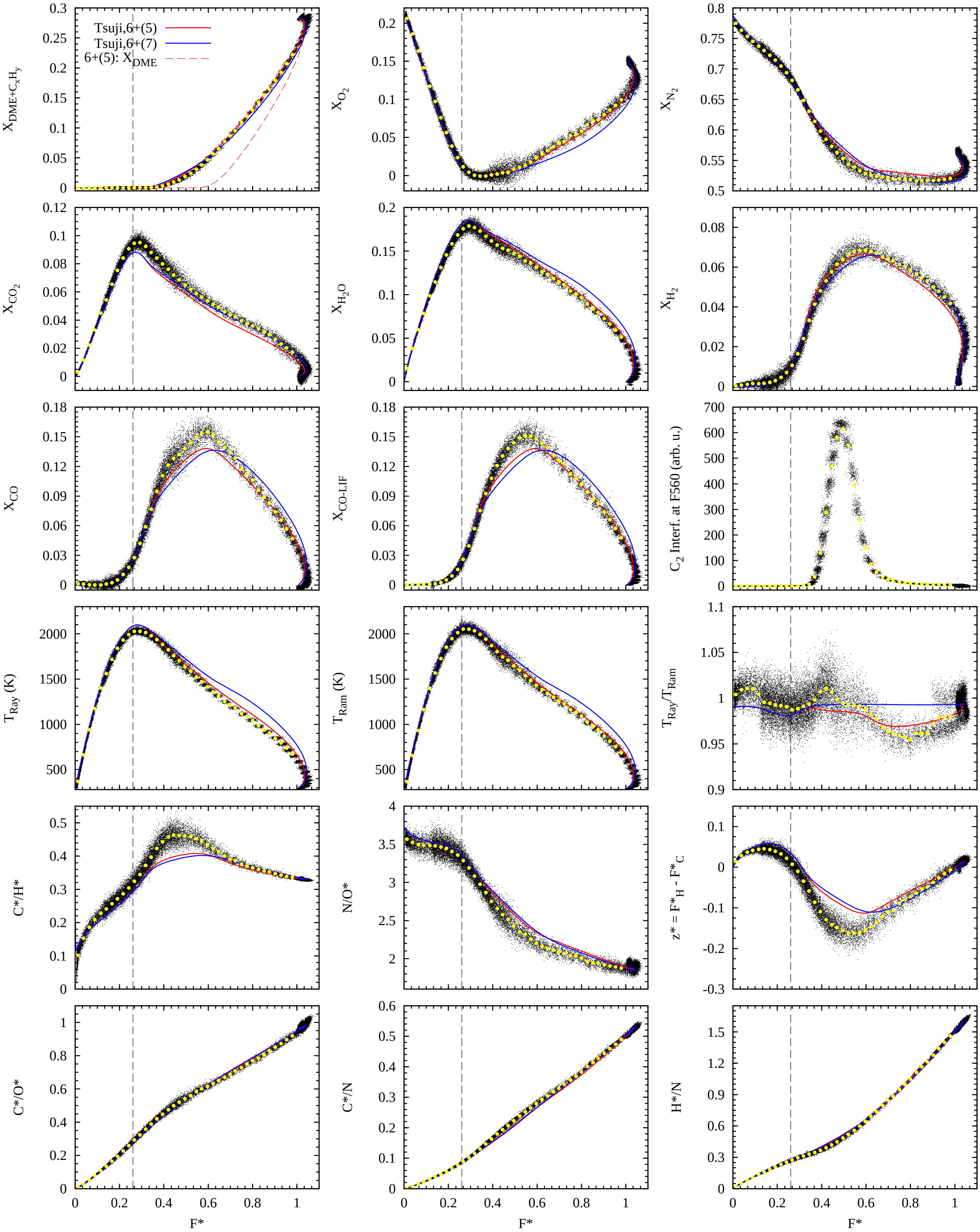

Figure 4.20: Measured and calculated results for the L2 laminar flame, including temperature, species mole fractions, LIF interferences, atom ratios, and differential diffusion parameter z^* plotted versus the

adapted mixture fraction F^* with stoichiometric condition at $F^*_{\mathrm{st}} = 0.26$ (dashed line). Simulated profiles are shown as lines vs. $F^*_{6+(5)}$ (red) and $F^*_{6+(7)}$ (blue). Black dots are results from single-shot measurements. Filled circles are conditional averages.

Laminar results L1

Similarly, the premixed Bunsen configuration L1 is examined. Data were acquired at positions $r = 0, 3, 6\,\mathrm{mm}$ corresponding to 3 mm overlap of the 6-mm probe volumes. The flame structure is dominated by a central premixed cone. Accordingly, gradients in the reaction zone located around $r = 2.5\,\mathrm{mm}$ are much steeper than for the L2 case. This poses high standards for precise Raman measurement at very high spatial resolution. Figures 4.21 and 4.22 show experimental results in comparison to laminar flame calculations in physical space and mixture fraction space F^*, respectively. The laminar flame calculation shown in this comparison is from the opposed jet geometry, with $a = 50\,\mathrm{s}^{-1}$ using Zhao et al. mechanism, and multi-component transport. Perfect agreement between experiments and calculations is not expected, due to differences between jet and opposed-flow geometries and also because of the expected high sensitivity of the premixed reaction zone location to radiation as shown by Barlow et al. [12] for laminar methane/air flames, which is not included in the calculation. Here, the strain rate of the calculation was selected to best match the separation between the premixed reaction zone and the stoichiometric condition, which is the portion of the flame important for evaluation of the hydrocarbon data evaluation scheme.

The maximum temperatures in experiment and simulation match within 30 K ($T_{\mathrm{max,calc.}} = 2136\,\mathrm{K}$). Again, the difference is attributed to radiation, a different inflow temperature in the calculation (290 K measured vs. 298 K in the calculation), and relative humidity. LIF interferences at the F560 channel are condensed to a much smaller region in physical space and are significantly lower (compare Fig. 4.16). As observed in the L2 configuration above CO_2 and CO are both higher in the experiment. For CO_2 the deviation at the peak is +5 %, for CO-LIF +9 %, whereas for H_2O -4 % is observed. Accordingly, the resulting C^*/H^* ratio is too high. In the L2 configuration, better matching was observed in mixture fraction space with the calculation using the $F^*_{6+(5)}$-definition. For the L1 configuration some scalars are in between both definitions $F^*_{6+(5)}$ and $F^*_{6+(7)}$. However, this question is very sensitive especially to the measurement of $X_{\mathrm{DME+CxHy}}$ which depends on the exact knowledge of the intermediate hydrocarbon composition, its corresponding Raman response curve and Rayleigh cross section model and points towards limitations of the current approach.

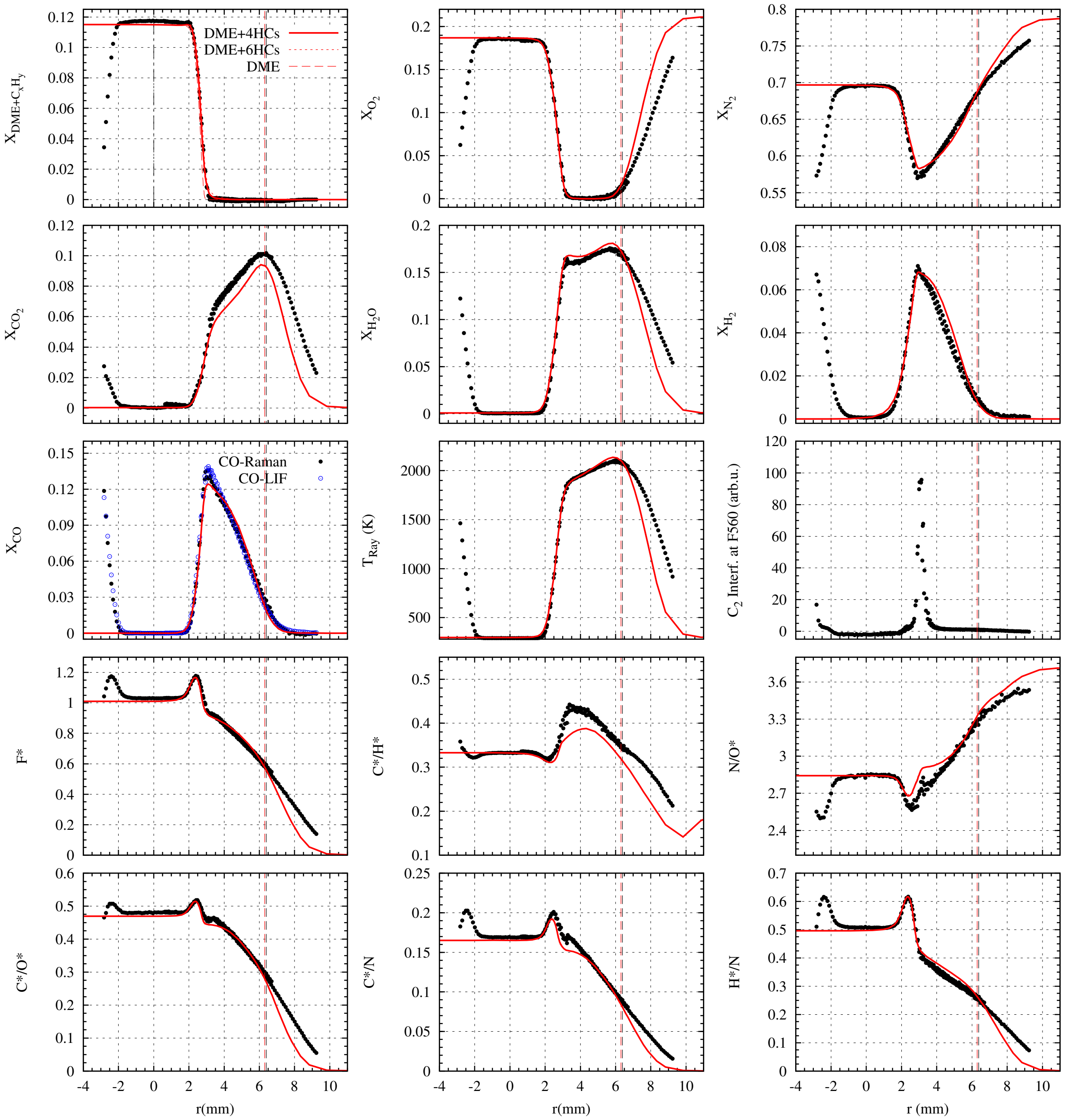

Figure 4.21: Mean temperature, species mole fractions, LIF interferences, adapted mixture fraction F^*, and atom ratios in physical space for the L1 flame. Results from simulations are shown by lines, experiments by circles. The vertical dashed line marks stoichiometric condition at $F^*_{\mathrm{st}} = 0.59$.

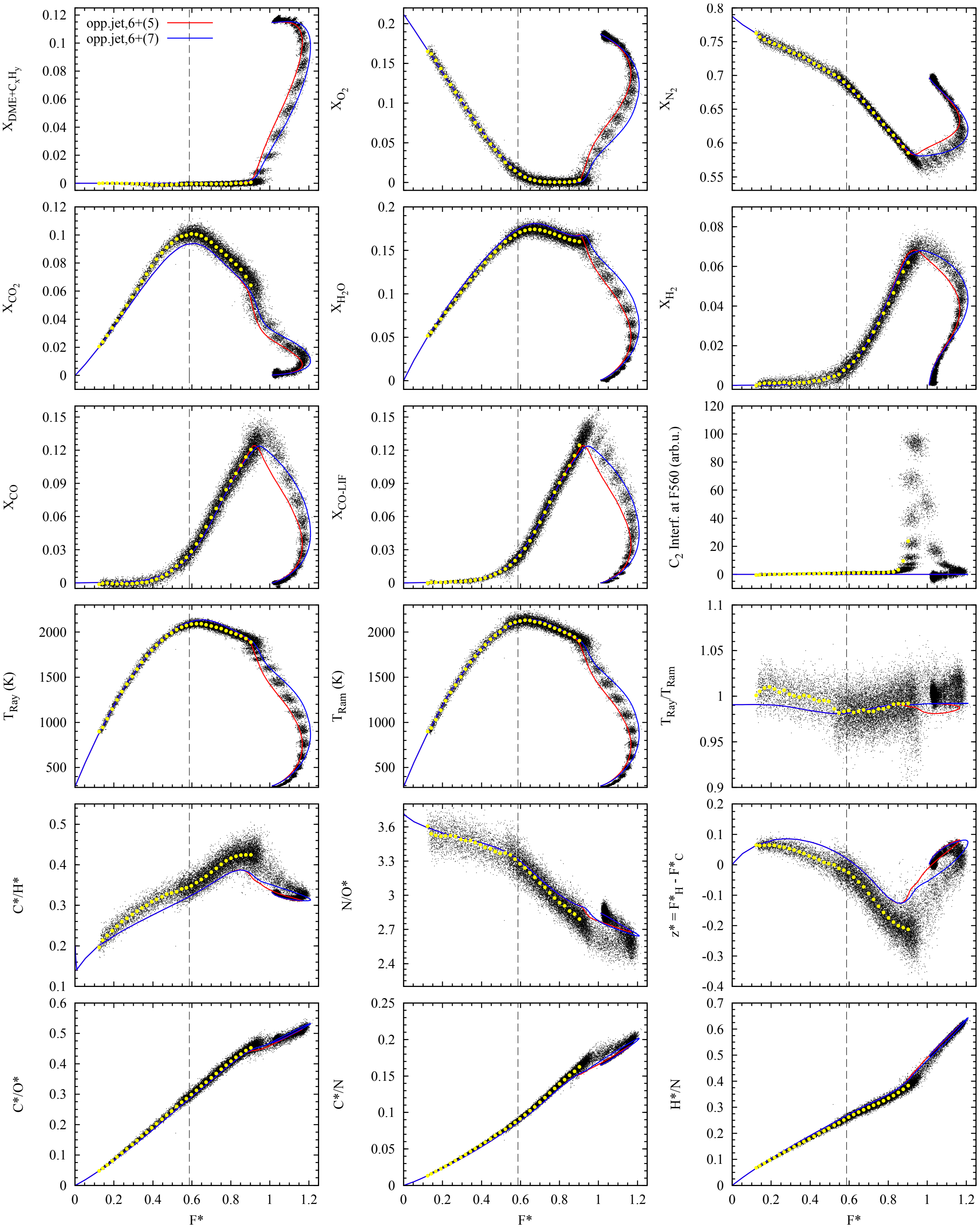

Figure 4.22: Measured and calculated results for the L1 laminar flame, including temperature, species mole fractions, LIF interferences, atom ratios, and differential diffusion parameter z^* in the adapted mixture

fraction space F^* with stoichiometric condition at $F^*_{\mathrm{st}} = 0.59$ (dashed line). Simulated profiles are shown as lines for 6+(5) species (red line) and 6+(7) species (blue line). Black dots are results from single-shot measurements. Filled circles are conditional averages.

Turbulent results

Measurements in the two turbulent piloted DME/air flames were originally intended mainly for evaluation of levels of fluorescence interference and they were limited to 200-shot files at a single downstream location $x/D = 15$ ($D = 7.2\,\mathrm{mm}$). Mixture compositions T2 (19.7 vol% DME in air) and T1 (11.4 vol% DME in air) were investigated at intermediate Reynolds-numbers corresponding roughly to flame D of the piloted CH_4/air flame series [9–11, 13, 55, 84]. The probe volume was centered near the location of maximum fluorescence interference in each flame ($r = 6\,\mathrm{mm}$ in T2 and $r = 4\,\mathrm{mm}$ in T1). Despite higher measurement-noise (see Table 4.1) the data were acquired with full spectral resolution, to allow for spectroscopic analysis, and process by applying software binning before matrix inversion.

Turbulent results T2

The Raman response regarding DME and intermediate hydrocarbon species and for the Rayleigh cross section model, a laminar flame calculation with an intermediate strain rate of $a = 400\,\mathrm{s}^{-1}$ and equal diffusivity transport in the Tsuji-geometry was used.

Figure 4.23 shows scatter plots of all measured scalars, atom ratios, and the molecular diffusion parameter z^* versus the adapted mixture fraction $F^*_{6+(5)}$ for the case T2. Data at the single 1D probe volume location give rise to values for F^* primarily in the range of $0.15 < F^* < 0.9$. Superimposed are profiles from various laminar flame calculations in the Tsuji-geometry, using either multi-component transport or equal diffusivities. For the multi-component transport cases the strain is varied, with $a = 100, 1000, 1750\,\mathrm{s}^{-1}$, and for equal diffusivities $a = 100, 1000, 2500\,\mathrm{s}^{-1}$. The highest strain rates correspond to the respective extinction limits. In addition, four profiles from CHEM1D using opposed jet geometry are shown as dashed lines. Strain rates of these curves with multi-component and equal diffusivities transport are $a = 100, 1500$ and $100, 2300\,\mathrm{s}^{-1}$, respectively. With the exception of large F^*-values and differences in strain rates the flame codes yield similar results for both transport models and the space spanned by both results largely overlaps.

The non-premixed flame structure is evident by the equally distributed scatter and gradual gradients in all scalars. Within a maximum deviation of 1.5 % at $F^* = 0.45$, temperatures determined via Rayleigh and Raman scattering agree very well (see $T_{\mathrm{Ray}}/T_{\mathrm{Ram}}$) supporting consistency in the data processing . Considering temperature and main species profiles, the conditional means are best matched by laminar flame calculations using equal diffusivities at intermediate strain.

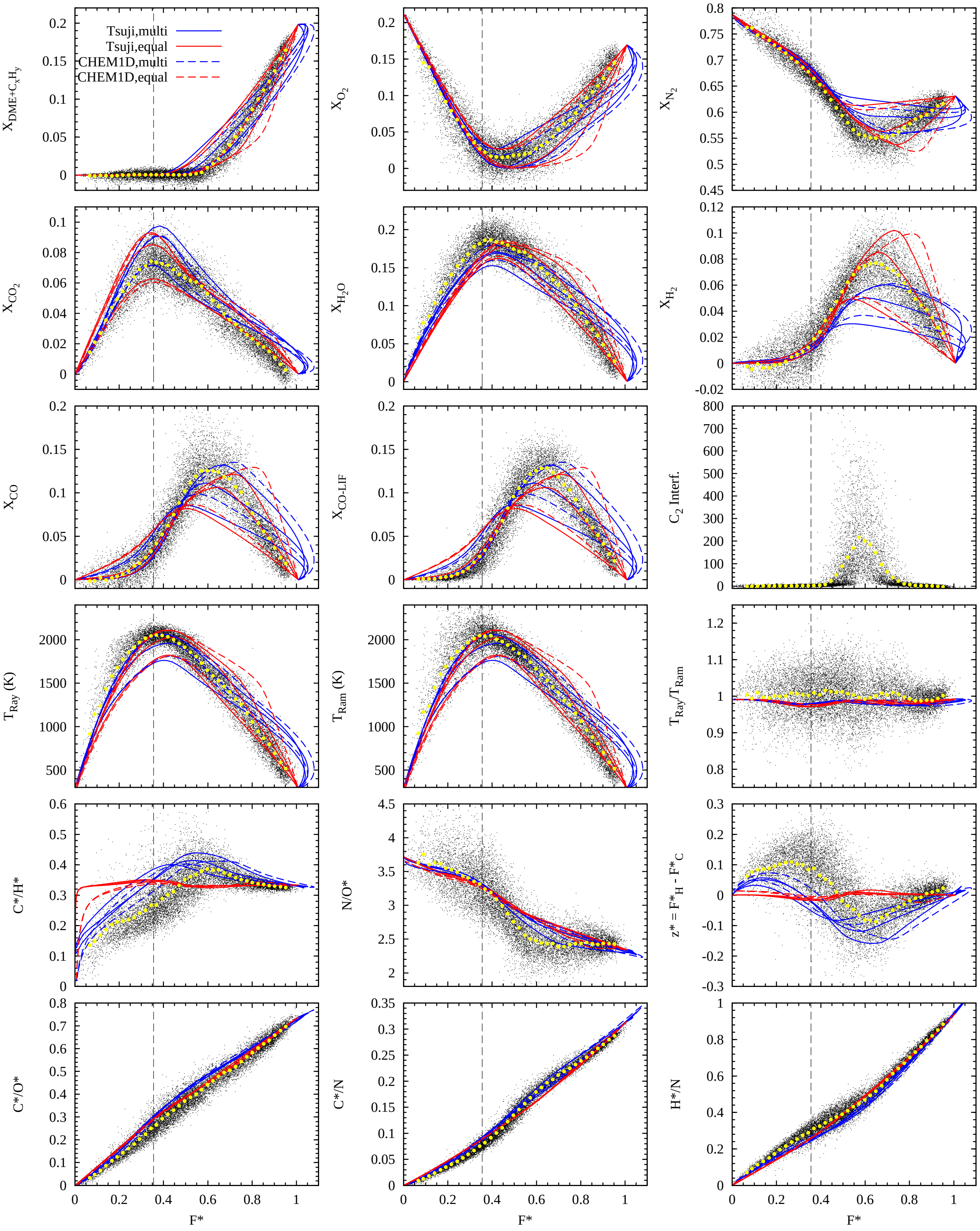

Figure 4.23: Scatter plots for the turbulent partially premixed flame T2 using the adapted mixture fraction coordinate F^* with stoichiometric condition at $F^*_{st} = 0.36$ (dashed line). Filled symbols are conditional

averages. Lines are from laminar flame calculations from OPPFLOW and CHEM1D and strain rates between $a = 100$ to $2500\,\mathrm{s}^{-1}$ as outlined in the text. Data were taken using software-binning. This explains part of the stronger scatter compared to the laminar cases. A quantitative analysis of the effect of turbulence on the fluctuations in mixture fraction space will be just possible in future studies using hardware-binning in the turbulent cases as well.

Different conclusions are drawn from both the C^*/H^*- and z^*-profiles, particularly in the range $0.5 < F^* < 0.8$, where differential diffusion effects are apparent, and the conditional mean profiles of these two quantities are clearly better matched by the multi-component transport model. It is apparent that both molecular diffusion and turbulent transport affect scalar transport in this flame, which is qualitatively consistent with results on transport effects in the CH_4/air piloted flame at similar Reynolds number reported by Barlow et al. [10].

Sensitivity of Rayleigh cross section model

As mentioned in Section 4.3.4, Raman and Rayleigh results are interlinked due to the iterative data evaluation scheme. This was neglected in the Rayleigh cross section study in Section 4.3.5. Here, the sensitivity of results from the T2 flame to the Rayleigh cross section model is examined within the complete data processing scheme. Figure 4.24 compares conditional average temperature results within the range $0.5 < F^* < 1$, based on Rayleigh cross section models derived from different laminar calculations. The calculation giving the overall best match in Fig. 4.23 ($a = 400\,\mathrm{s}^{-1}$, equal diffusivity) is shown as a guide line in Fig. 4.24. First, an unacceptable distortion of the temperature profile is found for data evaluation without applying any Rayleigh cross section model, but using the constant Rayleigh cross section of DME. This would lead to an over estimation of the temperature of up to 20 %. Still up to 10 % difference is found between models composed of the lowest and highest strain rates, where higher strain rates cause higher temperatures. A few percent higher temperatures are found for the models with underlying multi-component transport calculations. Hence, choosing an intermediate strain rate of $a = 400\,\mathrm{s}^{-1}$ for the Rayleigh cross section model seems to be the best compromise for the T2 configuration to minimize the uncertainty on the average values of the Rayleigh temperature measurement. It is of course a significant sensitivity and must be kept in mind as a possible systematic influence parameter when evaluating experimental Raman/Rayleigh data from DME flames, especially close to extinction and when even deriving observations from single-shot measurements.

Additionally, in Fig. 4.24 the impact of the Rayleigh cross section model on the hydrocarbon measurement is shown to be rather small. Interestingly, the amount of hydrocarbons is smaller for higher Rayleigh temperatures measured. From the decrease of the Raman response versus temperature (Fig. 4.6) the opposite would be expected. The explanation of this apparent contradiction is to be sought in the fact that the measured amount of

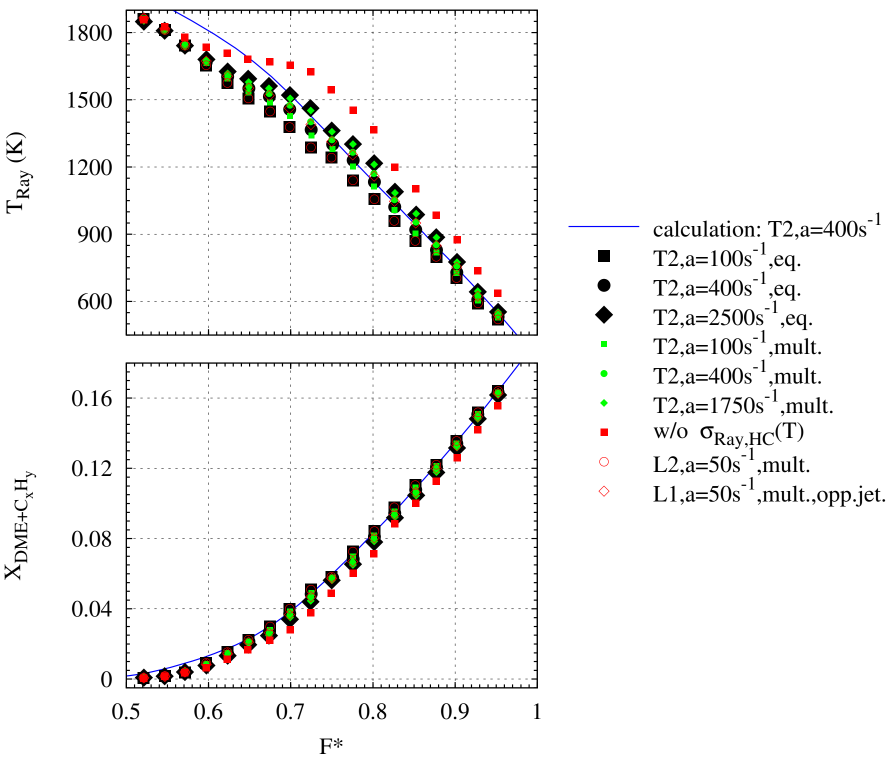

Figure 4.24: Various temperature dependent Rayleigh cross section models applied to the data evaluation in the turbulent T2 measurement. One calculation (solid line) is plotted as a guide line for the experimental data shown as conditional average in F^* space.

hydrocarbons in physical space is actually increasing as expected, but at the same time, its impact on the mixture fraction calculation is dominating and causing a shift of the coordinate to larger values. Finally, it is worth noting that the same comparison in physical space is different. There, deviations in time-averages of temperature are strongly attenuated due to intermittency and are found below 2 % between models of strain rates $a = 100\,\mathrm{s}^{-1}$ and $a = 2500\,\mathrm{s}^{-1}$. However, this of course is not true for evaluation of single-shots and generally, a good agreement with the simplified analysis presented at the end of Section 4.3.5 is found.

Turbulent results T1

Data measured in the T1 configuration are shown in Fig. 4.25. These data were processed using response curves and Rayleigh cross section model from the laminar calculation using the opposed jet geometry, T1 composition, $a = 100\,\mathrm{s}^{-1}$, and multi-component transport. This calculation and those from the Tsuji geometry for both transport models at different strain rates ($a = 100$ to $2250\,\mathrm{s}^{-1}$) are superimposed. The opposed jet geometry clearly better match premixed flames. The probe volume is centered at $r = 4\,\mathrm{mm}$ and comprises mostly mixture fractions $F^* > 0.6$. Profiles from CHEM1D are shown for multi-component transport and $a = 100$ and $1500\,\mathrm{s}^{-1}$ and for equal diffusivities at $a = 100\,\mathrm{s}^{-1}$. The difference in strain rate, already mentioned in Fig. 4.3, shows also up in mixture fraction space. Results from CHEM1D are generally shifted toward higher F^*-values at same strain rates. Interestingly, the calculation at highest strain rate perfectly matches the calculation in Tsuji geometry at lowest strain rate using multi-component transport.

For temperature and main species mole fractions a bimodal distribution appears that is typical for premixed flames: The reaction can occur without further mixing of fuel and oxidizer at almost identical values of mixture fraction. Spatially thin reaction zones reduce the probability measuring temperatures, educts, and products at intermediate states. Broadband and C_2-interferences are reduced significantly compared to the T2 flame (same relative units in Figures 4.23 and 4.25 in the scatter plot showing the level and positions of interferences). Conditional means are plotted only up to $F^* = 0.9$ to avoid the mixed influence from burned and unburned samples. Differential diffusion effects are well observable in all profiles. In addition to the C^*/H^* and z^*-profiles that are well reproduced by the multi-component opposed jet calculations, mixture fractions $F^* > 1$ are regularly measured and laminar-like behavior shows up for all species. A calculation with a higher strain in opposed jet geometry would probably better match the results. In contrast to T2, the agreement with characteristics of differential diffusion is as well observed for the most sensitive H_2-profile. To exclude possible errors in the data processing as a reason for measuring $F^* > 1$, its sensitivity was investigated against different hydrocarbon Raman responses, Rayleigh cross section models, and variations in the interference-corrections. But neither of these was found to influence the results shown in Fig. 4.25 significantly. The influence of differential diffusion, however, should be investigated in more depth in future studies.

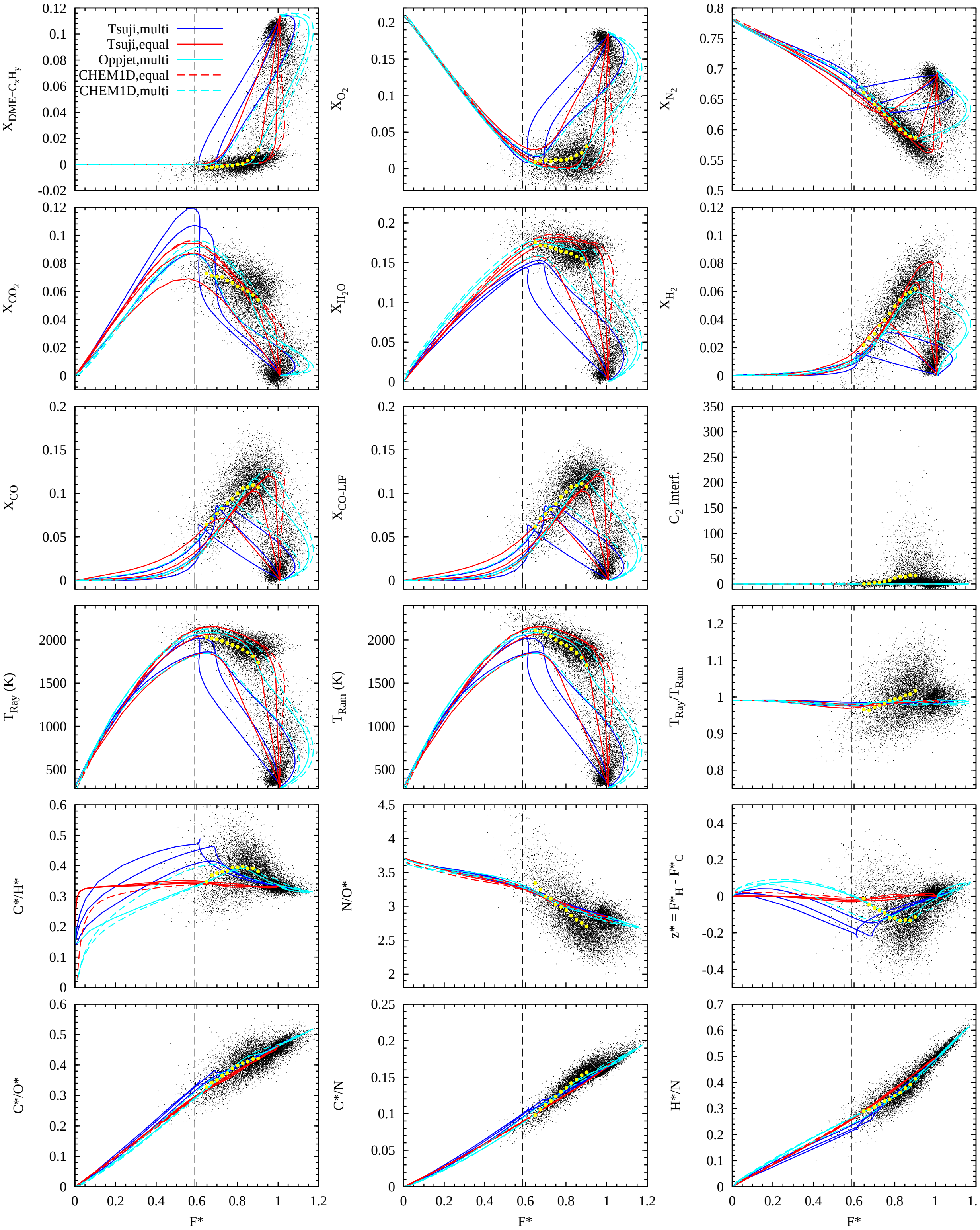

Figure 4.25: Scatter plots for the turbulent partially premixed flame T1 using the adapted mixture fraction coordinate F^* with stoichiometric condition at $F^*_{st} = 0.59$ (dashed line). Lines are from laminar flame

calculations as outlined in the text, filled symbols are conditional averages. Response curves and Rayleigh cross section model are from the opposed jet geometry, L1 composition, $a = 100\,\mathrm{s}^{-1}$. Data were taken using software-binning. This explains part of the stronger scatter compared to the laminar cases.

5 Conclusions

Detailed conclusions regarding the developed of the hybrid data reduction strategy were already given in Section 3.6. The presented hybrid method provided the base to make the data-processing in flames of DME possible.

The feasibility of measurements using line-imaged Raman/Rayleigh scattering and line-imaged CO-LIF in laminar and turbulent DME/air flames was investigated. DME was chosen as the next more complex fuel-candidate beyond methane due to significant lower interference levels than observed in flames of ethylene, ethane, and propane. The objective was to extend well-established methods applied to methane/air flames to allow for quantitative measurements of major species concentrations and temperature in DME/air flames.

In DME/air flames a number of additional complications were quantified by using 1D laminar flame computations. Much higher levels of intermediate hydrocarbons arise in the reaction zone than in similar methane/air flames. In the present measurements important intermediate hydrocarbons, i.e. methane, ethylene, and ethane were not distinguished from DME due to very similar Raman shifts. Formaldehyde and acetylene have different Raman shifts and were not detected at all. This impacted both, the measurement of major species by Raman scattering and the temperature measurement by Rayleigh scattering. In order to account for this fact, distributions of hydrocarbons were taken from 1D laminar flame calculations to provide additional information for the data processing of the measured Raman and Rayleigh signals. For the processing of both signals, temperature dependent models were derived to account for very different scattering properties of DME and intermediate hydrocarbons.

Measurements were obtained in two laminar jet flames of DME/air with stoichiometric values of mixture fraction $F_{\mathrm{st}} = 0.59$ and $F_{\mathrm{st}} = 0.26$. The proposed temperature dependent models were applied to the processing of the Raman and Rayleigh signals. Generally, good agreement of species mole fractions and temperature with 1D laminar flame calculations was observed for both flames in physical space. Locally, major differences are found in values of CO_2, CO, and the C/H atom ratio, which were all underpredicted by the calculation. The highest temperatures were overpredicted due to negligence of radiation in the calculation. Some of the observed differences may be due to 2D-effects apparent in jet flames, which can not be accounted for in 1D opposed-flow calculations. In particular, at the oxidizer side of the premixed Bunsen configuration ($F_{\mathrm{st}} = 0.59$) all scalar gradients are more gradual in the measurement. The approach to select the strain rate in the calculation to best match the separation between the premixed reaction zone and the stoichiometric condition is not able to predict correct gradients at both sides of this flame.

Another complication was identified for the conversion from measured species mole fractions to species mass fractions and corresponding mixture fraction. The difference between the molar mass of DME and the molar masses of intermediate species is large and additional assumptions were introduced to provide consistent comparison between calculations and experiments in an adapted mixture fraction space. Thereafter, good agreement was also found for the two laminar cases in this adapted mixture fraction space.

Towards measurements in turbulent DME/air flames sensitivities of the introduced models for the Raman and Rayleigh data processing were investigated with respect to strain rate and transport model. Significant differences were observed between models based on lowest and highest strain rates, whereas smaller differences were found between multi-component and equal diffusivity transport models.

Data from first measurements obtained in turbulent DME/air jet flames with stoichiometric values of mixture fraction $F_{\mathrm{st}} = 0.59$ and $F_{\mathrm{st}} = 0.36$ and Reynolds numbers of ~25000 were processed with the proposed approach and compared with results from laminar flame calculations in the adapted mixture fraction space. As for previously studied methane/air jet flames at similar conditions, the turbulent DME/air flame results showed some areas of agreement with laminar calculations based on equal diffusivities and some areas of agreement with calculations based on multi-component transport, indicating the importance of both turbulent transport and molecular diffusion. A higher impact of differential diffusion is generally observed in all DME/air flames due to much higher levels of molecular hydrogen.

6 Future Work

The hybrid method first developed for the experimental setup at the Combustion Research Facility in Sandia, Livermore was modified for experimental conditions at TU Darmstadt and already successfully applied on the data evaluation of measurements in stratified flames [85]. First comparison with numerical data could be also achieved and were already presented at the last TNF [95]. To take advantage of the benefit of smaller camera readout noise is still outstanding at TU Darmstadt due to the usage of an improper camera in those measurements. However, first tests with a new camera are promising for future measurements.

The presented results of measurements in flames of DME were already submitted to Combustion and Flame in March 2011 [40]. The data processing procedure is readily developed and can be applied to new measurements in turbulent flames of DME using on-chip binning and scanning larger regions of the flames to provide reasonable validation data sets for numerical calculations. First efforts toward this direction were already presented at the last TNF [95] by Frank et al. [38] with the introduction of a new series of well-defined benchmark flames of DME. First measurements in these flames using OH-LIF diagnostics were shown as well.

The method treating just DME so far is generalized to handle other complex hydrocarbons. This was shown as well at the last TNF and first results regarding Raman/Rayleigh scattering properties were already presented [95] for methanol, ethylene, ethane, and propane.

In this context, the present method based on the detection of seven major species may be extended by new on-chip binning regions with one or two additional channels to allow for the particular detection of acetylene and ethylene which both have promising strong signatures in the Raman spectra. Investigations of the temperature dependence of these signals and comprehensive noise studies with respect to inference levels would be mandatory.

In this work just qualitatively used is the subtraction of Raman spectra with perpendicular polarization directions. The development of such techniques and their application in turbulent flames constitutes another challenging research objective.

A Supplementary crosstalk curves

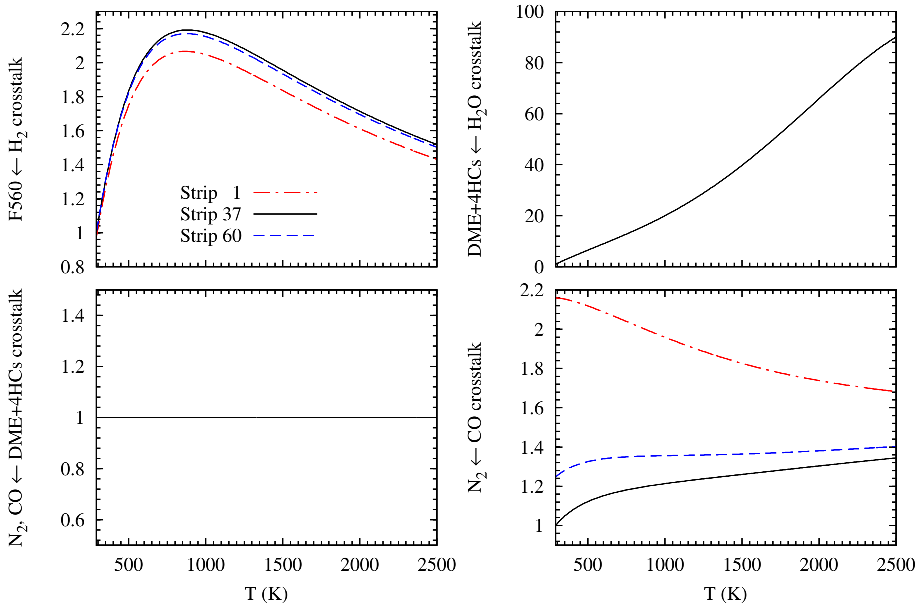

Figure A.1: Crosstalk curves supplementing information provided in Section 4.4.1.

Additional crosstalk curves are presented completing the information provided in Section 4.4.1. The crosstalks F560←H2 and N_2←CO were calculated following the procedure outlined in Chapter 3. The crosstalk curve for DME+4HCs←H_2O was transferred from previous CH_4/air flame measurements. So far, no measurements without N_2 were taken. Hence, the calibration of the crosstalk from DME+4HCs on N_2 relies on a procedure that follows two steps: at first crosstalk upon the O_2 channel was estimated from DME/N_2 flows, then DME/air flows were investigated using the crosstalk-corrected O_2 mole fraction to estimate DME contributions to the N_2 channel. Because the relative O_2/N_2 concentrations in air are known, excessive signal on the N_2 channel was attributed to DME-contributions. A more straightforward strategy would be to measure DME/He jets and will be done in future experiments. Note that the crosstalk contribution N_2←DME+4HCs is assumed to be independent on temperature because of lack of more detailed information.

B Sensitivity of change in the Raman crosstalks

CO_2←DME+4HCs and O_2←DME+4HCs exemplified on the L2 configuration

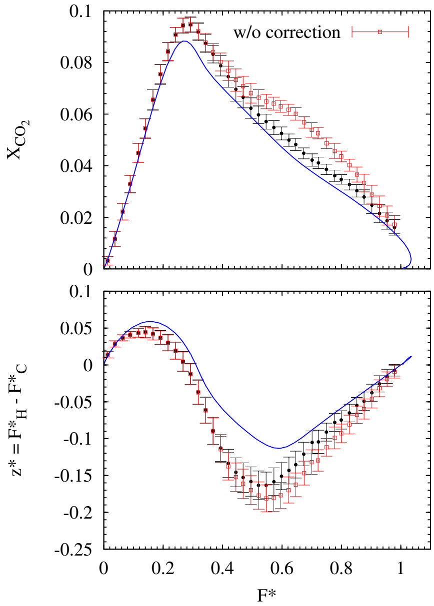

Figure B.1: Sensitivity of the additional correction on CO_2←DME+4HCs crosstalk, which was applied on the crosstalk derived from experimental spectra and species distributions from laminar flame calculations following Eq. (4.3). Errorbars denote the measurement precision as one standard deviation from 100 single laser shots.

Exemplarily, the data evaluation of the L2 configuration was made with and without the additional background correction implied in the CO_2←DME+4HCs crosstalk (compare Fig. 4.14). Figure B.1 shows the impact on the CO_2 mole fractions and z^*-profiles in mixture fraction space. A value of up to 0.012 smaller mole fractions is obtained using the background correction. Independent of this correction all other scalars are very close to the calculation. Therefore, it is assumed that this obvious mismatch in the CO_2-profile must be caused by an uncorrected interference signal on CO_2. The impact on any other of the profiles shown in Fig. B.1 is negligible. This is exemplified on the most sensitive z^*-profile, where still no significant difference is observable. The impact of the additional correction on $O_2 \leftarrow$DME+4HCs (compare Fig. 4.14) was much smaller and is therefore not shown explicitly.

Bibliography

[1] DALTON, a molecular electronic structure program, Release 2.0 (2005). URL `http://www.kjemi.uio.no/software/dalton/dalton.html`.

[2] International Energy Agency (IEA). *Key world energy statistics.* URL `http://iea.org/textbase/nppdf/free/2010/key_stats_2010.pdf`.

[3] Python – uncertainties. URL `http://packages.python.org/uncertainties/`.

[4] CHEM1D 3.0 – A one-dimensional laminar flame code. Eindhoven University of Technology. 2007. URL `http://www.combustion.tue.nl`.

[5] Allan, A., McKean, D. C., Perchard, J. P., and Josien, M. L. Vibrational spectra of crystalline dimethyl ethers. *Spectrochim. Acta, Part A*, 27(8):1409 – 1437, 1971.

[6] Avila, G., Fernandez, J. M., Mate, B., Tejeda, G., and Montero, S. Ro-vibrational Raman Cross-Sections of Water Vapor in the OH Stretching Region. *J. Mol. Spectrosc.*, 196:77 – 92, 1999.

[7] Bacskay, G. B., Saebø, S., and Taylor, P. R. On the calculation of dipole moment and polarizability derivatives by the analytical energy gradient method: Application to the formaldehyde molecule. *Chem. Phys.*, 90(3-4):215 – 224, 1984.

[8] Barlow, R. S., Carter, C. D., and Pitz, R. W. Multi-species diagnostics in turbulent flames. In Kohse-Höinghaus, K. and Jeffries, J. B., editors, *Applied Combustion Diagnostics*, Combustion: An International Series. Taylor & Francis, New York, 2002.

[9] Barlow, R. S. and Frank, J. H. Effects of turbulence on species mass fractions in methane/air jet flames. *Proc. Combust. Inst.*, 27:1087–1095, 1998.

[10] Barlow, R. S., Frank, J. H., Karpetis, A. N., and Chen, J.-Y. Piloted methane/air jet flames: Transport effects and aspects of scalar structure. *Combust. Flame*, 143 (4):433 – 449, 2005.

[11] Barlow, R. S. and Karpetis, A. N. Measurements of scalar variance, scalar dissipation, and length scales in turbulent piloted methane/air jet flames. *Flow Turbul. Combust.*, 72:427–448, 2004.

[12] Barlow, R. S., Karpetis, A. N., Frank, J. H., and Chen, J.-Y. Scalar profiles and NO formation in laminar opposed-flow partially premixed methane/air flames. *Combust. Flame*, 127(3):2102 – 2118, 2001.

[13] Barlow, R. S., Ozarovsky, H. C., Karpetis, A. N., and Lindstedt, R. P. Piloted jet flames of CH_4/H_2/air: Experiments on localized extinction in the near field at high Reynolds numbers. *Combust. Flame*, 156(11):2117 – 2128, 2009.

[14] Barlow, R. S., Wang, G. H., Anselmo-Filho, P., Sweeney, M. S., and Hochgreb, S. Application of Raman/Rayleigh/LIF diagnostics in turbulent stratified flames. *Proc. Combust. Inst.*, 32(1):945 – 953, 2009.

[15] Barlow, R. S. Laser diagnostics and their interplay with computations to understand turbulent combustion. *Proc. Combust. Inst.*, 31(1):49 – 75, 2007.

[16] Belyanin, V. B. History of the discovery of the phenomenon of Raman light scattering. *J. Appl. Spectrosc.*, 30:510–515, 1979.

[17] Bergmann, V., Meier, W., Wolff, D., and Stricker, W. Application of spontaneous Raman and Rayleigh scattering and 2D LIF for the characterization of a turbulent $CH_4/H_2/N_2$ jet diffusion flame. *Appl. Phys. B*, 66:489–502, 1998.

[18] Bilger, R. W., Stårner, S. H., and Kee, R. J. On reduced mechanisms for methane—air combustion in nonpremixed flames. *Combust. Flame*, 80(2):135 – 149, 1990.

[19] Blom, C. E., Altona, C., and Oskam, A. Application of self-consistent-field ab initio calculations to organic molecules VI. Dimethylether : general valence force field scaled on experimental frequencies, infra-red and Raman intensities. *Mol. Phys.*, 34 (2):557–571, 1977.

[20] Bogaard, M. P., Buckingham, A. D., Pierens, R. K., and White, A. H. Rayleigh scattering depolarization ratio and molecular polarizability anisotropy for gases. *J. Chem. Soc., Faraday Trans. 1*, 74:3008–3015, 1978.

[21] Bongers, H. *Analysis of Flamelet-Based Methods to Reduce Chemical Kinetics in Flame Computations*. PhD thesis, Eindhoven University of Technology, 2005. URL `http://www.combustion.tue.nl`.

[22] Boudon, V., Rey, M., and Loëte, M. The vibrational levels of methane obtained from analyses of high-resolution spectra. *J. Quant. Spectrosc. Radiat. Transfer*, 98(3):394 – 404, 2006.

[23] Bridge, N. J. and Buckingham, A. D. The polarization of laser light scattered by gases. *Proc. R. Soc. Lond. A*, 295:334 – 349, 1966.

[24] Brockhinke, A., Hartlieb, A. T., Kohse-Höinghaus, K., and Crosley, D. R. Tunable KrF laser-induced fluorescence of C_2 in a sooting flame. *Appl. Phys. B: Lasers Opt.*, 67:659–665, 1998.

[25] Bruna, P. J., Hachey, M. R. J., and Grein, F. Benchmark ab initio calculations of formaldehyde, H_2CO. *J. Mol. Struct.: THEOCHEM*, 400:177 – 221, 1997.

[26] Buldakov, M. A., Cherepanov, V. N., Korolev, B. V., and Matrosov, I. I. Role of intramolecular interactions in Raman spectra of N_2 and O_2 molecules. *J. Mol. Spectrosc.*, 217(1):1–8, 2003.

[27] Carter, C. D. *Laser-based Rayleigh and Mie scattering methods.* Handbook of Fluid Dynamics and Fluid Machinery, Wiley, New York, 1996.

[28] Champion, J.-P., Loëte, M., and Pierre, G. *Spherical Top Spectra. Spectroscopy of the Earth's Atmosphere and Interstellar Medium.* Academic Press, San Diego, 1992.

[29] Chen, J.-Y. personal communication. *University of California, Berkeley*, 2010.

[30] Chou, C.-P., Chen, J.-Y., Yam, C. G., and Marx, K. D. Numerical Modeling of NO Formation in Laminar Bunsen Flames–A Flamelet Approach. *Combust. Flame*, 114 (3-4):420 – 435, 1998.

[31] Demaison, J., Boggs, E. J., and Csaszar, A. G., editors. *Equilibrium Molecular Structures - From Spectroscopy to Quantum Chemistry.* CRC Press Taylor & Francis Group, 2011.

[32] Demtröder, W. *Molekülphysik.* Oldenburg Verlag München Wien, 2003.

[33] Dibble, R. W., Masri, A. R., and Bilger, R. W. The spontaneous Raman scattering technique applied to nonpremixed flames of methane. *Combust. Flame*, 67(3):189 – 206, 1987.

[34] Dibble, R. W., Stårner, S. H., Masri, A. R., and Barlow, R. S. An Improved Method of data Aquisition and Reduction for Laser Raman-Rayleigh and Fluorescence Scattering from Multispecies. *Applied Physics B*, 51:39–43, 1990.

[35] Dreyer, C., Parker, T., and Linne, M. A. Raman scattering at 532 and 355 nm in atmospheric pressure propane/air flames, with and without liquid fuels. *Appl. Phys. B: Lasers Opt.*, 79:121–130, 2004.

[36] Eckbreth, A. *Laser Diagnostics for Combustion Temperature and Species.* Energy and Engineering Science. Taylor & Francis, 1998.

[37] Egermann, J., Seeger, T., and Leipertz, A. Application of 266-nm and 355-nm Nd:YAG laser radiation for the investigation of fuel-rich sooting hydrocarbon flames by Raman scattering. *Appl. Opt.*, 43(29):5564–5574, Oct 2004.

[38] Frank., J. H., Hsu, A. G., and Kuhl, J. Turbulent Partially Premixed Dimethyl Ether/Air Jet Flames: A New Series of Target Flames for Experiments and Modeling. *Proceedings of TNF 10*, 2010. URL `http://www.sandia.gov/TNF/10thWorkshop/TNF10.html`.

[39] Fuest, F. Raman-Spektren diatomarer Moleküle: Eine Optimierung der Spektren Simulation. Diploma thesis, TU Darmstadt, Energie- und Kraftwerkstechnik, 2006.

[40] Fuest, F., Barlow, R. S., Chen, J.-Y., and Dreizler, A. 1D Raman/Rayleigh-scattering and CO-LIF measurements in laminar and turbulent jet flames of dimethyl ether. *Combust. Flame*, submitted, 2011.

[41] Fuest, F., Barlow, R. S., Geyer, D., Seffrin, F., and Dreizler, A. A hybrid method for data evaluation in 1-D Raman spectroscopy. *Proc. Combust. Inst.*, 33(1):815 – 822, 2011.

[42] Gardiner, W. C., Jr., Hidaka, Y., and Tanzawa, T. Refractivity of combustion gases. *Combust. Flame*, 40:213 – 219, 1981.

[43] Geyer, D. *1D-Raman/Rayleigh experiments in turbulent-opposed jet flows.* PhD thesis, Technische Universität Darmstadt, Germany, ISBN 3-18-353306-5, 2005.

[44] Geyer, D. personal communication. *TU Darmstadt*, 2011.

[45] Geyer, D., Kempf, A., Dreizler, A., and Janicka, J. Turbulent opposed-jet flames: A critical benchmark experiment for combustion LES. *Combust. Flame*, 143(4):524 – 548, 2005.

[46] Gregor, M. A., Seffrin, F., Fuest, F., Geyer, D., and Dreizler, A. Multi-scalar measurements in a premixed swirl burner using 1D Raman/Rayleigh scattering. *Proc. Combust. Inst.*, 32:1739 – 1746, 2009.

[47] Hädrich, S., Hefter, S., Pfelzer, B., Doerk, T., Jauernik, P., and Uhlenbusch, J. Determination of the absolute Raman cross section of methyl. *Chem. Phys. Lett.*, 256(1-2):83 – 86, 1996.

[48] Hameka, H. F. Theoretical prediction of structures and infrared frequencies : Part II. Alcohols and ethers. *J. Mol. Struct.: THEOCHEM*, 226(3-4):241 – 249, 1991.

[49] Hassel, E. P. and Linow, S. Laser diagnostics for studies of turbulent combustion. *Meas. Sci. Technol.*, 11:R37–R57, 2000.

[50] Helgaker, T., Jorgensen, P., and Olsen, J. *Molecular Electronic Structure Theory.* John Wiley & Sons, 2002.

[51] Herzberg, G. *Molecular spectra and molecular structure Vol. II, Infrared and Raman spectra of polyatomic molecules.* Krieger Publishing Company, Malabar, Florida, 1991.

[52] Hohm, U. and Kerl, K. Interferometric measurements of the dipole polarizability a of molecules between 300K and 1100K I.Monochromatic measurements at l = 632.99nm for the noble gases and H_2, N_2, O_2, and CH_4. *Mol. Phys.*, 69(5):803–817, 1990.

[53] Jourdanneau, E., Chaussard, F., Saint-Loup, R., Gabard, T., and Berger, H. The methane Raman spectrum from 1200 to 5500ăcm-1: A first step toward temperature diagnostic using methane as a probe molecule in combustion systems. *J. Mol. Spectrosc.*, 233(2):219 – 230, 2005.

[54] Kaiser, E. W., Wallington, T. J., Hurley, M. D., Platz, J., Curran, J., Pitz, W. J., and Westbrook, C. K. Experimental and modeling study of premixed atmospheric-pressure Dimethyl Ether-Air flames. *J. Phys. Chem. A*, 104(35):8194–8206, 2000.

[55] Karpetis, A. N. and Barlow, R. S. Measurements of scalar dissipation in a turbulent piloted methane/air jet flame. *Proc. Combust. Inst.*, 29:1929–1936, 2002.

[56] Karpetis, A. N. and Barlow, R. S. Measurements of flame orientation and scalar dissipation in turbulent partially premixed methane flames. *Proc. Combust. Inst.*, 30:665 – 672, 2005.

[57] Kattawar, G. W., Young, A. T., and Humphreys, T. J. Inelastic scattering in planetary atmospheres. I. The ring effect, without aerosols. *Astrophys. J.*, pages 243 – 1049, 1981.

[58] Kee, R. J., Grcar, J. F., Smooke, M. D., and Miller, J. A. A Fortran program for modeling steady laminar one-dimensional premixed flames. Technical report, Sandia National Laboratories Report SAND85-8240, 1992.

[59] Kelly, P. B. and Westre, S. G. Resonance Raman spectroscopy of the methyl radical. *Chem. Phys. Lett.*, 151(3):253 – 257, 1988.

[60] Kojima, J. and Nguyen, Q.-V. Quantitative analysis of spectral interference of spontaneous Raman scattering in high-pressure fuel-rich H2-air combustion. *Journal of Quantitative Spectroscopy and Radiative Transfer*, 94(3-4):439 – 466, 2005.

[61] Lammers, F. A. and de Goey, L. P. H. The influence of gas radiation on the temperature decrease above a burner with a flat porous inert surface. *Combust. Flame.*, 136:533–47, 2004.

[62] Le Roy, R. J. LEVEL 7.7: A Computer Program for Solving the Radial Schrödinger Equation for Bound and Quasibound Levels,. *University of Waterloo Chem. Phys. Research Report CP-661(2005);see the Computer Programs link at*, http://leroy.uwaterloo.ca, 2005.

[63] Linow, S., Dreizler, A., Janicka, J., and Hassel, E. P. Measurement of temperature and concentration in oxy-fuel flames by Raman/Rayleigh spectroscopy. *Meas. Sci. Technol.*, 13:1952–1961, 2002.

[64] Long, D. A. *The Raman Effect: A Unified Treatment of the Theory of Raman Scattering by Molecules.* Wiley, 2002.

[65] Lutz, A. E., Kee, R. J., Grcar, J. F., and Rupley, F. M. OPPDIF: A Fortran program for computing opposed-flow diffusion flames. Technical report, Sandia National Laboratories Report SAND96-8243, 1997.

[66] Lutz, A. E., Kee, R. J., and Miller, J. A. SENKIN: A Fortran Program for Predicting Homogeneous Gas Phase Chemical Kinetics with Sensitivity Analysis. *Sandia National Laboratories Tech. Rep. SAND87-8248*, 1988.

[67] Masri, A. R., Dibble, R. W., and Barlow, R. S. The structure of turbulent nonpremixed flames of methanol over a range of mixing rates. *Combust. Flame*, 89(2): 167 – 185, 1992.

[68] Masri, A. R., Kalt, P. A. M., and Barlow, R. S. The compositional structure of swirl-stabilised turbulent nonpremixed flames. *Combust. Flame*, 137(1-2):1 – 37, 2004. ISSN 0010-2180.

[69] Meier, W. and Keck, O. Laser Raman scattering in fuel-rich flames: background levels at different excitation wavelengths. *Meas. Sci. Technol.*, 13:741–749, 2002.

[70] Miles, P. C. Raman line imaging for spatially and temporally resolved mole fraction measurements in internal combustion engines. *Appl. Opt.*, 38(9):1714–1732, 1999.

[71] Miles, R. B., Lempert, W. R., and Forkey, J. N. Laser Rayleigh Scattering. *Meas. Sci. Technol.*, 12:R33–R51, 2001.

[72] Miller, J. A., Kee, R. J., Smooke, M. D., and Grcar, J. F. The computation of the structure and extinction limit of a methane-air stagnation point diffusion flame. *Spring Meeting of the Western State Section of the Combustion Institute*, WSS/CI84-10, 1984.

[73] Mokhov, A. V., Gersen, S., and Levinsky, H. B. Spontaneous Raman measurements of acetylene in atmospheric-pressure methane/air flames. *Chem. Phys. Lett.*, 403 (4-6):233 – 237, 2005.

[74] Murphy, W. F. The ro-vibrational Raman spectrum of water vapour ν_1 and $2\nu_2$. *Mol. Phys.*, 33(6):1701 – 1714, 1977.

[75] Murphy, W. F. The rovibrational Raman spectrum of water vapour ν_1 and ν_3. *Mol. Phys.*, 36(3):727 – 732, 1978.

[76] Murphy, W. F. The Rayleigh depolarization ratio and rotational Raman spectrum of water vapor and the polarizability components for the water molecule. *J. Chem. Phys.*, 67(12):5877–5882, 1977.

[77] Nooren, P. A., Versluis, M., van der Meer, T. H., Barlow, R. S., and Frank, J. H. Raman-Rayleigh-LIF measurements of temperature and species concentrations in the Delft piloted turbulent jet diffusion flame. *Appl. Phys. B: Lasers Opt.*, 71:95–111, 2000.

[78] Pecul, M. and Rizzo, A. Linear response coupled cluster calculation of Raman scattering cross sections. *J. Chem. Phys.*, 116(4):1259–1268, 2002.

[79] Pfuderer, D. G., Neuber, A. A., Früchtel, G., Hassel, E. P., and Janicka, J. Turbulence modulation in jet diffusion flames: Modeling and experiments. *Combust. Flame*, 106(3):301 – 317, 1996.

[80] Rabenstein, F. and Leipertz, A. One-Dimensional, time-Resolved Raman measurements in a sooting flame made with 355-nm excitation. *Appl. Opt.*, 37(21):4937–4943, Jul 1998.

[81] Raizer, Y. P. *Gas Discharge Physics.* Springer, Berlin, 1997.

[82] Rowell, R. L., Aval, G. M., and Barrett, J. J. Rayleigh–Raman Depolarization of Laser Light Scattered by Gases. *J. Chem. Phys.*, 54(5):1960–1964, 1971.

[83] Savitzky, A. and Golay, M. J. E. Smoothing and Differentiation of Data by Simplified Least Squares Procedures. *Analytical Chemistry*, 36(8):1627–1639, 1964.

[84] Schneider, C., Dreizler, A., Janicka, J., and Hassel, E. P. Flow field measurements of stable and locally extinguishing hydrocarbon-fuelled jet flames. *Combust. Flame*, 135(1-2):185–190, 2003.

[85] Seffrin, F. *Geschwindigkeits- und Skalarfeld-Charakterisierung turbulenter stratifizierter Vormischflammen.* PhD thesis, Technische Universität Darmstadt, Germany, ISBN 978-3-86955-649-9, 2010.

[86] Seffrin, F., Fuest, F., Geyer, D., and Dreizler, A. Flow field studies of a new series of turbulent premixed stratified flames. *Combust. Flame*, 157(2):384 – 396, 2010.

[87] Seshadri, K. and Williams, F. A. Laminar flow between two plates with injection of a reactant at high Reynolds number. *Int. J. Heat Mass Transfer*, 21:251–253, 1978.

[88] Sneep, M. and Ubachs, W. Direct measurement of the Rayleigh scattering cross section in various gases. *J. Quant. Spectrosc. Radiat. Transfer*, 92(3):293 – 310, 2005.

[89] Stårner, S. H., Bilger, R. W., Dibble, R. W., and Barlow, R. S. Some Raman/Rayleigh/LIF measurements in turbulent propane flames. *Symp. Int. Combust. Proc.*, 23:645 – 651, 1991.

[90] Stephenson, D. A. Raman cross sections of selected hydrocarbons and freons. *J. Quant. Spectrosc. Radiat. Transfer*, 14(12):1291 – 1301, 1974.

[91] Struve, W. S. *Fundamentals of Molecular Spectroscopy.* John Wiley & Sons, 1989.

[92] Sutton, G., Levick, A., Edwards, G., and Greenhalgh, D. A combustion temperature and species standard for the calibration of laser diagnostic techniques. *Combust. Flame*, 147(1-2):39 – 48, 2006.

[93] Tacke, M. M., Linow, S., Geiss, S., Hassel, E. P., and Janicka, J. Experimental and numerical study of a highly diluted turbulent diffusion flame close to blowout. *Proc. Combust. Inst.*, 27:1139–1148, 1998.

[94] TNF. International Workshop on Measurement and Computation of Turbulent Nonpremixed Flames (TNF). URL `http://www.ca.sandia.gov/TNF`.

[95] TNF. Proceedings of TNF 10. 2010. URL `http://www.sandia.gov/TNF/10thWorkshop/TNF10.html`.

[96] van Oijen, J. A. *Flamelet-Generated Manifolds: Development and Application to Premixed Laminar Flames.* PhD thesis, Eindhoven University of Technology, 2002. URL `http://www.combustion.tue.nl`.

[97] van Oijen, J. A. and de Goey, L. P. H. Modelling of Premixed Laminar Flames using Flamelet-Generated Manifolds. *Combust. Sci. and Techn.*, 161:113 – 137, 2000.

[98] Vidler, M. and Tennyson, J. Accurate partition function and thermodynamic data for water. *J. Chem. Phys.*, 113:9766 – 9771, 2000.

[99] Wang, G. and Barlow, R. S. Spatial resolution effects on the measurement of scalar variance and scalar gradient in turbulent nonpremixed jet flames. *Exp. Fluids*, 44: 633–645, 2008.

[100] Wang, G., Karpetis, A. N., and Barlow, R. S. Dissipation length scales in turbulent nonpremixed jet flames. *Combustion and Flame*, 148(1-2):62 – 75, 2007.

[101] Wenger, C. and Champion, J. P. Spherical Top Data System (STDS) software for the simulation of spherical top spectra. *J. Quant. Spectrosc. Radiat. Transfer*, 59(3 - 5):471 – 480, 1998.

[102] Wiegeler, W. and Bleckmann, P. Calculation of relative Raman intensities: II. Calculations using an extended Hückel valence basis set. *J. Mol. Struct.*, 66:273 – 280, 1980.

[103] Zhao, J. Image Curvature Correction and Cosmic Removal for High-Throughput Dispersive Raman Spectroscopy. *Appl. Spectrosc.*, 57, 11:1368–1375, 2003.

[104] Zhao, Z., Chaos, M., Kazakov, A., and Dryer, F. L. Thermal Decomposition Reaction and a Comprehensive Kinetic Model of Dimethyl Ether. *Int. J. Chem. Kinet.*, 40: 1–18, 2008.

Lebenslauf

Name	Frederik Fuest
Geburtsdatum	25.07.1976
Geburtsort	Bielefeld

08.1987 - 06.1996	Tilemannschule Limburg Abitur
07.1996 - 08.1997	Caritas Limburg, Zivildienst MSHD Altenpflege und -betreuung, Behindertenbetreuung Astrid-Lindgren Schule
10.1997 - 01.2006	Technische Universität Darmstadt Studium des Allgemeinen Maschinenbaus Abschluss: Diplom Ingenieur
02.2006 - 2011	Technische Universität Darmstadt Wissenschaftlicher Mitarbeiter am Fachgebiet für Energie- und Kraftwerkstechnik